DESIGN & FABRICATION OF AN AIRBORNE REMOTE SENSING SYSTEM FOR GAS PIPE-LINE LEAK DETECTION

DSS File No. 15SQ.23440-0-9103

PHASE I - CONCEPTUAL DESIGN REPORT

REQ. NO. 0-9103

Monitoring Environmental Quality
Monteq Ltd., 630 Rivermede Road, Concord, Ontario, Canada L4K 1B6 (416) 669-5334 Cable: Monteq Toronto

CONTRACT REPORT NO. 1SQ81-00003

DESIGN & FABRICATION OF AN AIRBORNE REMOTE SENSING SYSTEM FOR GAS PIPE-LINE LEAK DETECTION

DSS File No. 15SQ.23440-0-9103

PHASE I - CONCEPTUAL DESIGN REPORT

MTR #81-27
August, 1981

84 pp

MICROMEDIA

JUL 29 1983

TABLE OF CONTENTS

1. GAS FILTER CORRELATION TECHNIQUE..... 1

1.1 Introduction..... 1

1.2 Difference Signal in the Absence of the Solar Radiation..... 2

1.3 Effect of Terrain Variation & Fluctuating Air Temperature..... 4

1.4 Effect of the Sensor Altitude..... 10

1.5 Effect of Emission from the Correlation Cell..... 10

1.6 Residual Interfering Gases..... 12

1.7 Difference Signal in the Presence of the Solar Radiation..... 12

1.8 Difference Signal of CH_4 Gas at 3.4 μm..... 15

1.9 Footprint Size..... 15

2. MODEL CALCULATION..... 17

2.1 Introduction..... 17

2.2 LOWTRAN Study..... 17

2.3 High Resolution Modelling..... 19

2.3.1 Results of The Model Calculation at 3.4 μm..... 24
2.3.2 Results of The Model Calculation at 7.8 μm..... 30
2.3.3 Ethane Spectrum..... 34

2.4 Gas Dispersion Model..... 34

3. SIGNAL TO NOISE CALCULATION..... 38

3.1 Electric Noise..... 38

3.2 Estimation of the Detection Limit..... 42

4. OPTICS..... 46

4.1 Introduction..... 46

4.2 Optical Components & Critical Areas..... 46

4.2.1 Lenses..... 46
4.2.2 Systematic Correlation of the Terrain Structure with Optical Components..... 47
4.2.3 Interference Filter..... 48
4.2.4 Thermal Radiation Noise..... 51
4.2.5 The Chopper Wheel..... 55
4.2.6 Detector..... 57

4.2 Optical Configuration..... 59

5. SIGNAL PROCESSING..... 61
5.1 Introduction..... 61
5.2 Selection of the Spectral Bands..... 61
5.3 Signal Processing Concept..... 62

6. ANALOG SIGNAL PROCESSING..... 64
6.1 General Discussion..... 64
6.2 Phase Sensitive Detection..... 64
6.3 Analog to Digital..... 67

7. INSTRUMENT CALIBRATION AND TEST..... 70
7.1 Confirmation of the Optimum Cell Parameters..... 70
7.2 The Difference Signal Balancing..... 70
7.3 Instrument Sensitivity Calibration..... 72
7.4 Instrument Stability..... 73

8. MECHANICAL DESIGN..... 75

9. PLAN FOR THE FIELD TEST..... 76

10. WORK STATEMENT..... 77

REFERENCES

1. GAS FILTER CORRELATION TECHNIQUE

1.1 Introduction

Several instrumental techniques have been used to make passive remote measurements of trace gases in the atmosphere. These include conventional spectrometers and interferometers, as well as the generally more sensitive and specific sensors using correlation techniques. Correlation sensors include dispersive[1,2], interferometric[3,4] and non-dispersive gas filter correlation devices[5,6]. The gas filter correlation technique (GFC) has some strong advantages; the sensor complexity is low, sensitivity and accuracy are high, and interference by other gases is minimized.

The GFC techniques are based on the concept that a sample of gas can provide an efficient and selective filter for measuring radiation absorbed or emitted from a specific target gas. The GFC technique has high sensitivity because of its large light gathering capability (large etendue) since all wavelengths are sampled simultaneously. In the GFC technique the gas cell forms a matched filter so that the radiation due to a specific gas is monitored, and the radiation due to the presence of other gases is rejected; thus, a high degree of specificity is obtained.

In the proposed system thermal radiation from the ground is the background source against which the pipeline leak gas, between the surface and the downward looking sensor, is to be detected. Several difficulties are inherent in this type of measurement, and care must be taken to detect this gas. These difficulties are due to such factors as the competing thermal absorption and emission from the leak gas, the normal background gas present in the atmosphere (especially methane), and solar reflected radiation competing with thermal emission. An evaluation of these problem areas is included in this report.

However, it does appear to be possible to overcome these difficulties and to develop a sensor capable of successful detection of pipeline leaks.

The basis of operation of the GFC sensor is the differential transmission, through separate reference and measurement gas cells, of radiation entering the sensor.

$$\text{output} = \int \text{incoming radiation} \quad (\text{cell}_1 - x.\text{cell}_2)\, d\lambda$$

where x is chosen to make the sensor cell responses equal when the incoming radiation contains no radiation specific to the gas to be detected.

1.2 Difference Signal in the Absence of the Solar Radiation

The signal corresponding to the total amount of trace gas in a column subtended by the instrument field of view is represented as a difference in energy transmitted between the correlation gas cell and the reference cell. Using the earth blackbody radiation as the radiation source, one can write the difference signal at the detector as

$$\Delta S = A\Omega \int_{\Delta\nu} \left\{ \eta_c I_o(\nu) e^{-\tau_c(\nu)} - \eta_r I_o(\nu) e^{-\tau_r(\nu)} \right\} d\nu + J_c \qquad (1\text{-}1)$$

where η_c and η_r are the transmission coefficients of the optical components for the correlation channel and reference channel, respectively. $A\Omega$ is the instrument etendue, and $\tau_c(\nu)$ and $\tau_r(\nu)$ are the optical depths of the channels. J_c is the emission term from the correlation gas. At wavelengths appreciably longer than 3.5 μ, the solar spectrum has no significant importance to the total radiation flux if the reflection coefficient of the earth surface is less than 0.2. Thus, $I_o(\nu)$ can be approximated as follows:

$$I_o(\nu) = \left\{ \varepsilon B_e(\nu, \theta_e) e^{-\tau_a(\nu)} + B_a(\nu, \theta_a)\left(1 - e^{-\tau_a(\nu)}\right) \right\} \qquad (1\text{-}2)$$

where $B(\nu,\theta)$ - the blackbody radiance at frequency ν, temperature θ

ε - emissivity of the earth's surface

$\tau_a(\nu)$ - optical thickness of target gas

and subscripts e and a designate the earth and atmosphere, respectively.

Substituting equation (1-2) into equation (1-1) one obtains.

$$\Delta S = \eta_c A\Omega \left\{ \varepsilon \bar{B}_e \int_{\Delta\nu} e^{-\tau_a(\nu)} \left(e^{-\tau_c(\nu)} - \frac{\eta_r}{\eta_c} e^{-\tau_r(\nu)} \right) d\nu \right.$$
$$\left. + \bar{B}_a \int_{\Delta\nu} \left(1 - e^{-\tau_a(\nu)}\right) \left(e^{-\tau_c(\nu)} - \frac{\eta_r}{\eta_c} e^{-\tau_r(\nu)} \right) d\nu \right\} \quad (1\text{-}3)$$

where the bar stands for the average.

Normally the reference channel transmittance is adjusted to get $\Delta S = J_c$ when there is no trace gas in the atmosphere. Thus,

$$\int_{\Delta\nu} e^{-\tau_c(\nu)} d\nu = \frac{\eta_r}{\eta_c} \int_{\Delta\nu} e^{-\tau_r(\nu)} d\nu \quad (1\text{-}4)$$

If we write,

$$T(\nu) = e^{-\tau(\nu)} \quad (1\text{-}5)$$

we get,

$$\frac{\eta_r}{\eta_c} = \frac{\bar{T}_c}{\bar{T}_r} \quad (1\text{-}6)$$

and

$$\Delta S = \eta_c A\Omega \left(\varepsilon \bar{B}_e - \bar{B}_a\right) \int_{\Delta\nu} \left(T_a T_c - \frac{\bar{T}_c}{\bar{T}_r} T_a T_r\right) d\nu + J_c \quad (1\text{-}7)$$

Since T_a and T_r are not correlated, further simplification leads to

$$\Delta S = \eta_c A\Omega \left(\varepsilon \bar{B}_e - \bar{B}_a\right) \left(\overline{T_a T_c} - \bar{T}_a \bar{T}_c\right) \Delta\nu + J_c \quad (1\text{-}8)$$

we shall refer to $(\overline{T_a T_c} - \bar{T}_a \cdot \bar{T}_c)$ as the 'correlation coefficient'.

1.3 Effect of Terrain Variation & Fluctuating Air Temperature

As shown in equation (1-8), the difference signal is proportional to the product of the difference of the Planck functions for the earth and atmosphere ($\varepsilon = 1$) and the correlation coefficient. Even with a constant amount of residual gas in the atmosphere, i.e. T_a not varying, the variation in $(\varepsilon\bar{B}_e - \bar{B}_a)$ will cause a variation in the output signal. Since the difference signal corresponding to 10 ppm-M, CH_4 amounts only to 3% of total ΔS due to the atmospheric residual CH_4 gas[8], and $(\varepsilon\bar{B}_e - \bar{B}_a)$ can vary as much as a few hundred percent, we need to measure $(\varepsilon\bar{B}_e - \bar{B}_a)$ precisely and incorporate it in the signal processing routine.

It is well known that, except for relatively short periods before dawn, there are convective air plumes, eddy flows, and gravitational waves in a normal standard atmosphere. The typical heights of convective plumes range from several meters up to about 300 m with an average value of about 100 m, and extend horizontally from a few tens of meters to about 200 m. The gravitational wave may have a wavelength of 1.5 Km with amplitude of 100 m. Therefore the temperature at low altitude (<100 m) may show fluctuations with an amplitude as high as 1.5° K[8]. This temperature fluctuation has a tendency to decrease with height. Since the instrument will normally be flown above this convective flow and the sensor footprint is large, one can expect to have an average air temperature which will show less fluctuation. At the instant the sensor field of view crosses the boundary of the eddies one may see a larger temperature change. However, the average temperature (vertically averaged) will not fluctuate to the same extent[9]. Furthermore, with the speed of the aircraft of $\sim$ 120 knots and the field of view of the instrument of $\sim$ 40 m, $\sim$ 100 m on the ground, will be covered in one second averaging out any small scale horizontal temperature fluctuation. Thus, considering that we are averaging the temperature vertically $\sim$ 350 m and horizontally $\sim$ 100 m for each measurement, the average air temperature fluctuation is estimated to be less than 0.5° K.

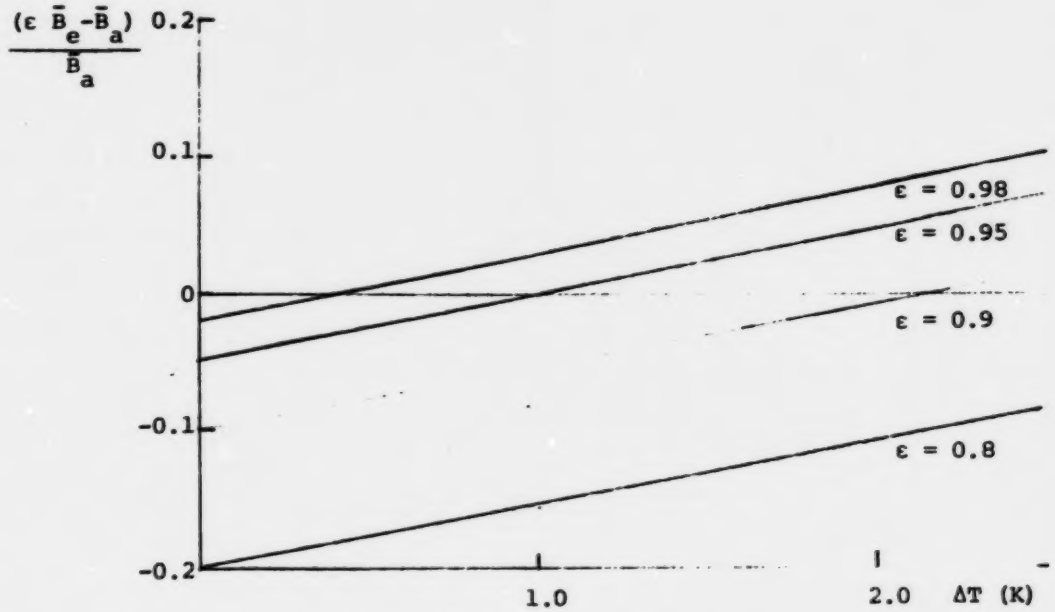

FIGURE 1: $(\varepsilon \bar{B}_e - \bar{B}_a)/\bar{B}_a$ as a function of ΔT $(=T_e - T_a)$ for various ground emissivities at λ = 3.4 μ

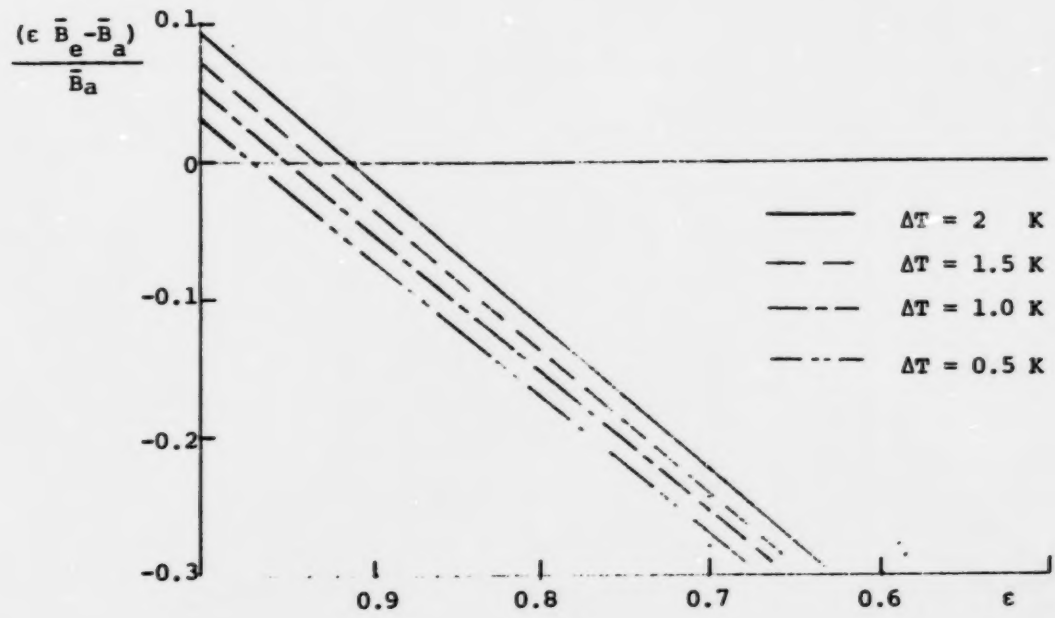

FIGURE 2: $(\varepsilon \bar{B} - \bar{B}_a)/\bar{B}_a$ as a function of the ground emissivity for various ΔT at λ = 3.4 μ

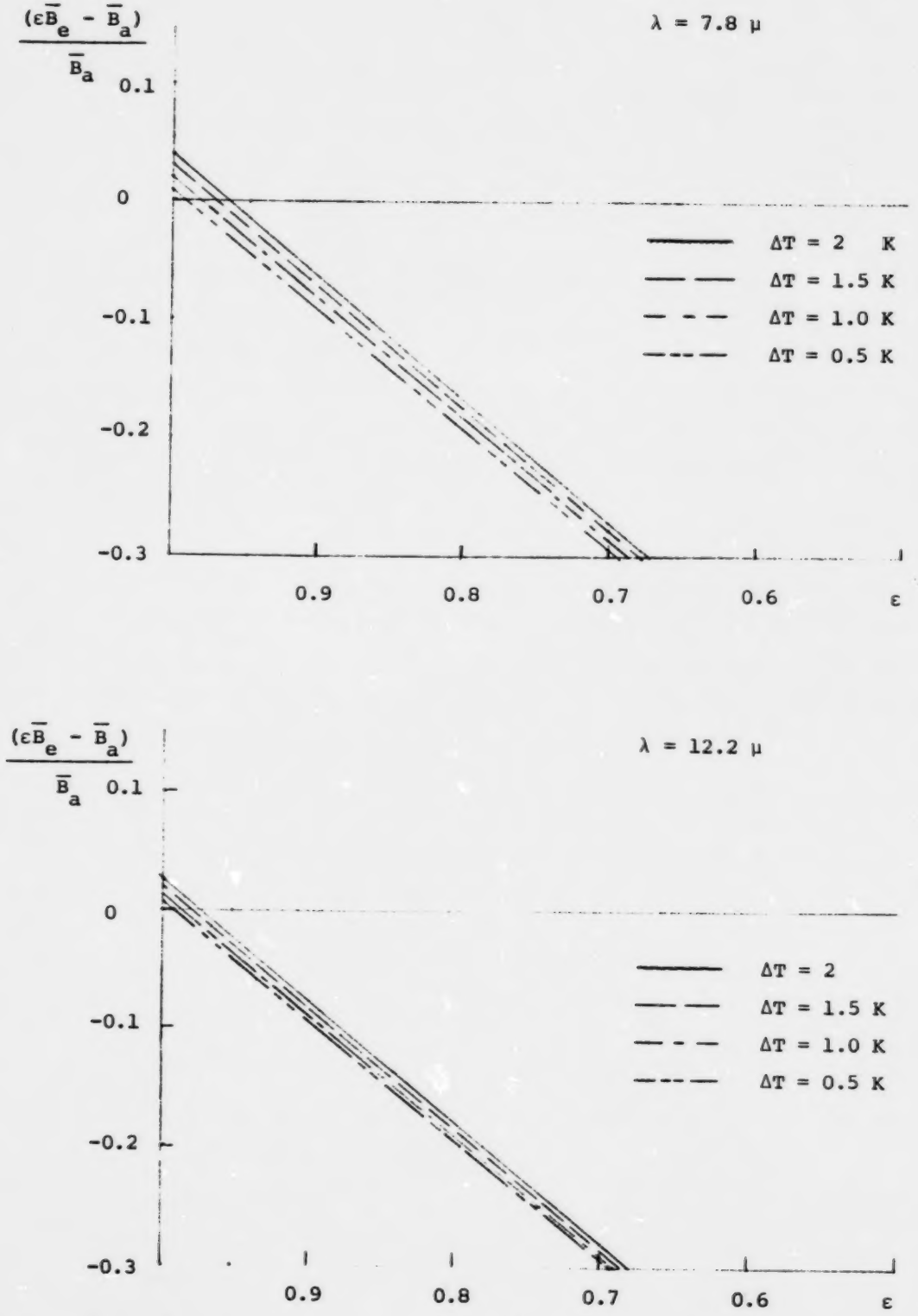

FIGURE 3: $(\varepsilon\bar{B}_e - \bar{B}_a)/\bar{B}_a$ as a function of the ground emissivity for various ΔT's at λ = 7.8 μ (upper) and λ = 12.2 μ (lower)

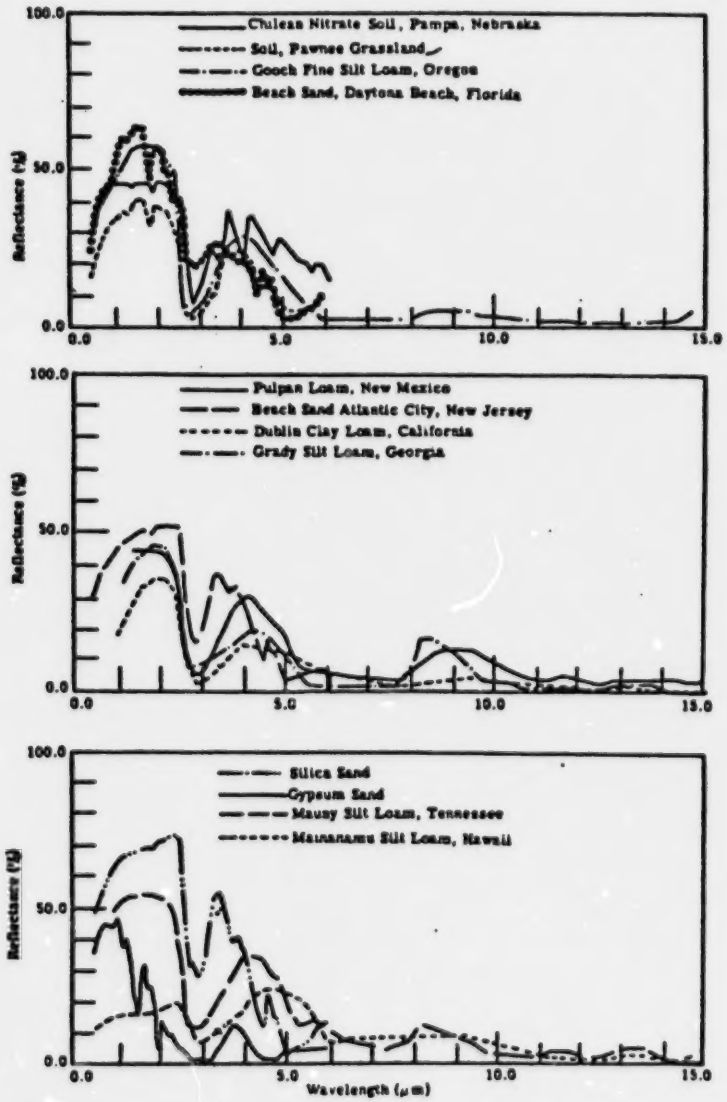

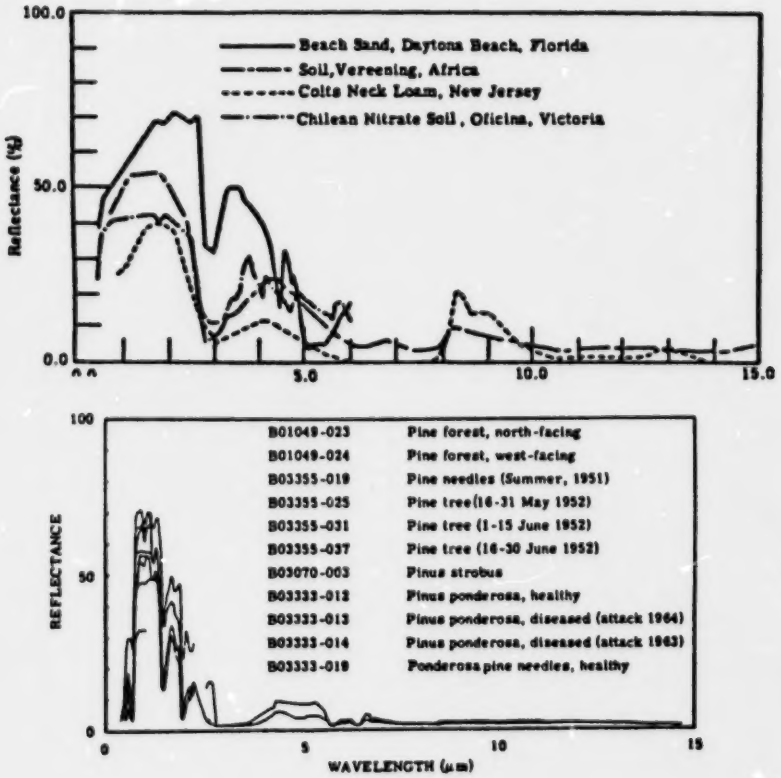
Beach Sand, Daytona Beach, Florida
Soil, Vereening, Africa
Colts Neck Loam, New Jersey
Chilean Nitrate Soil, Oficina, Victoria
Reflectance (%)
B01049-023 Pine forest, north-facing
B01049-024 Pine forest, west-facing
B03355-019 Pine needles (Summer, 1951)
B03355-025 Pine tree (16-31 May 1952)
B03355-031 Pine tree (1-15 June 1952)
B03355-037 Pine tree (16-30 June 1952)
B03070-003 Pinus strobus
B03333-012 Pinus ponderosa, healthy
B03333-013 Pinus ponderosa, diseased (attack 1964)
B03333-014 Pinus ponderosa, diseased (attack 1963)
B03333-019 Ponderosa pine needles, healthy
REFLECTANCE
WAVELENGTH (μm)

FIGURE 4: Ground reflection coefficient as a function of wavelength for various ground conditions[10,11]

For a 0.5° K temperature fluctuation, the change in the average radiance, $\bar{B}_a$, is estimated as follows:

$$\Delta \bar{B}_a = \bar{B}_a \frac{h\nu}{kT} \frac{\Delta T}{T} \simeq 0.025\, \bar{B}_a \qquad (1\text{-}9)$$

On the other hand, the variation in terrain emissivity may give fluctuations in $\varepsilon\bar{B}_e$ as high as 20%[10]. Although the fluctuation in $\bar{B}_a$ is not as large as the variation of $\varepsilon\bar{B}_e$ it cannot be ignored since $1/(\varepsilon\bar{B}_e - \bar{B}_a)$ goes through the pole for a small difference between the earth temperature and air temperature as shown in Figure 1. This stringent constraint is more serious for high emissivity values (ε>0.9) and somewhat relaxed for low emissivity values as shown in Figure 2 at λ = 3.4 μ.

The behaviour of the $(\varepsilon\bar{B}_e - \bar{B}_a)/\bar{B}_a$ is very much the same at λ = 7.8 μ and 11.8 μ, although the pole is moved to higher ε values for the given ΔT.

It is important to note that the average values of ε at different wavelengths are not the same, as shown in Table 1 and Figure 4.

$\lambda(\mu)$	$\bar{\varepsilon}$	$\Delta\bar{\varepsilon}$	$\Delta(\varepsilon\bar{B}_e-\bar{B}_a)/(\varepsilon\bar{B}_e-\bar{B}_a)$
3.4	0.85	±0.1	77%
7.8	0.95	±0.04	60%
11.8	0.95	±0.02	59%

TABLE 1: Expected emissivity variations[10]

It is concluded that the relative fluctuation in $(\varepsilon\bar{B}_e - \bar{B}_a)$ shows the highest value at λ = 3.4 and the lowest value at λ = 12.8 μ. The fluctuation due to air temperature variation is also included in the above estimation of $\Delta(\varepsilon\bar{B}_e - \bar{B}_a)/(\varepsilon\bar{B}_e - \bar{B}_a)$.

Improving the precision of $(\varepsilon\bar{B}_e - \bar{B}_a)$ may be accomplished as follows:

a) Incorporating a Separate Radiometric Measurement

$\bar{B}_a$ can be radiometrically measured by using a carefully selected spectral window. In order to do this a band of uniformly mixed atmospheric gas is required which provides an optical depth of greater than 1 at the sensor flight altitude. The CO_2 band at $\lambda = 4.3\ \mu$ has an optical depth of approximately 5 in a standard atmosphere at 300 m altitude. A measurement made at this wavelength will provide an estimate of $\bar{B}_a$, which when combined with $\varepsilon\bar{B}_e$ measured through the reference channel can yield $\varepsilon\bar{B}_e - \bar{B}_a$.

b) Incorporating a Second Correlation Cell

If the difference signal is measured as ΔS of a uniformly mixed atmospheric interference gas, it will have the $(\varepsilon\bar{B}_e - \bar{B}_a)$ term in exactly the same way as the target gas signal provided emissivity is the same for the interferent and target gas wavelengths. By ratioing $\Delta S/\Delta SI$ signals one can isolate the correlation terms. If the interference gas mixing ratio is uniform and constant, the remaining variation is due to the correlation term of the target gas only. This method has the further advantage that, in the ratioing process, any instrument altitude effect for uniformly mixed target gas will be cancelled out. A CO_2 band at $\lambda = 4.3\ \mu$ and an N_2O band at $\lambda = 7.8$[10] and the CH_4 band at 7.8 μ appears to be proper for this concept.

c) Determination of Representative $\bar{B}_a$

The average air temperature may be measured and $\bar{B}_a$ for the temperature may be calculated. This method requires a precise calibration and accurate measurement. The average air temperature should be measured often in order to have the allowable precision. There are also practical difficulties in measuring the average temperature to better than 0.5 K accuracy[12].

The effect of the air temperature fluctuation will be less serious for C_2H_6 measurement, due to there being less residual C_2H_6 gas in the atmosphere.

1.4 Effect of the Sensor Altitude

Since there is approximately 1.4 ppm of residual CH_4 in the atmosphere up to 22 Km altitude, the variation of the height of the airborne instrument will appear as a signal variation. A pulse radar altimeter system, commercially available, could be used to continuously monitor the height of the instrument with an accuracy of 1 m. However, because of the detection limits (10 to 60 ppm M) it appears adequate to read out the altitude from existing aircraft systems and only include a dedicated radar altimeter into GASPILS after proving the need.

1.5 Effect of Emission from the Correlation Cell

The emission from the correlation gas will appear as a noise signal fluctuating according to the gas temperature variation. There are many experimental ways to remove this term in the signal processing. The method proposed here is to use a scaled down blackbody radiation of the chopper wheel assuming thermal equilibrium between the gas and the chopper wheel.

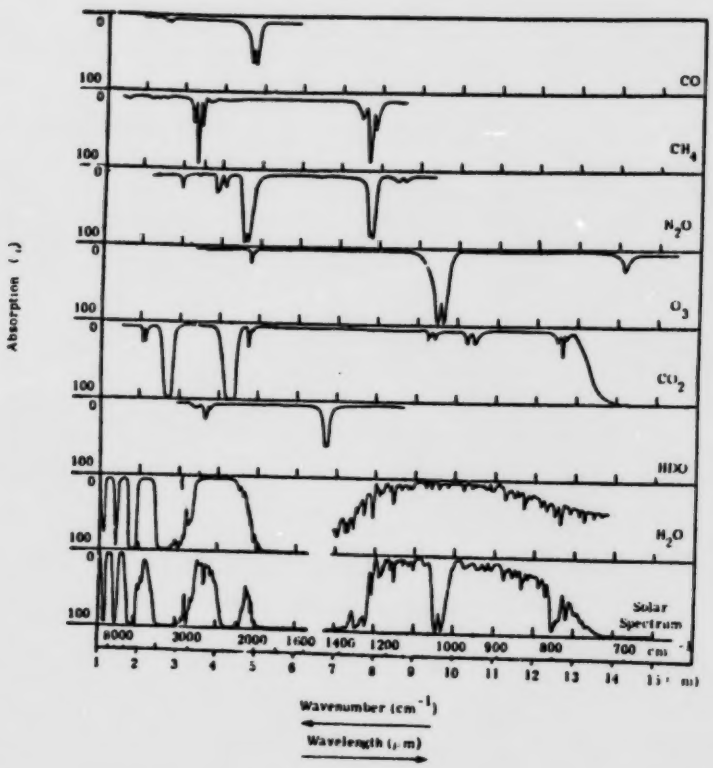

FIGURE 5: Low resolution solar spectrum from 1.0 to 15.0 μm

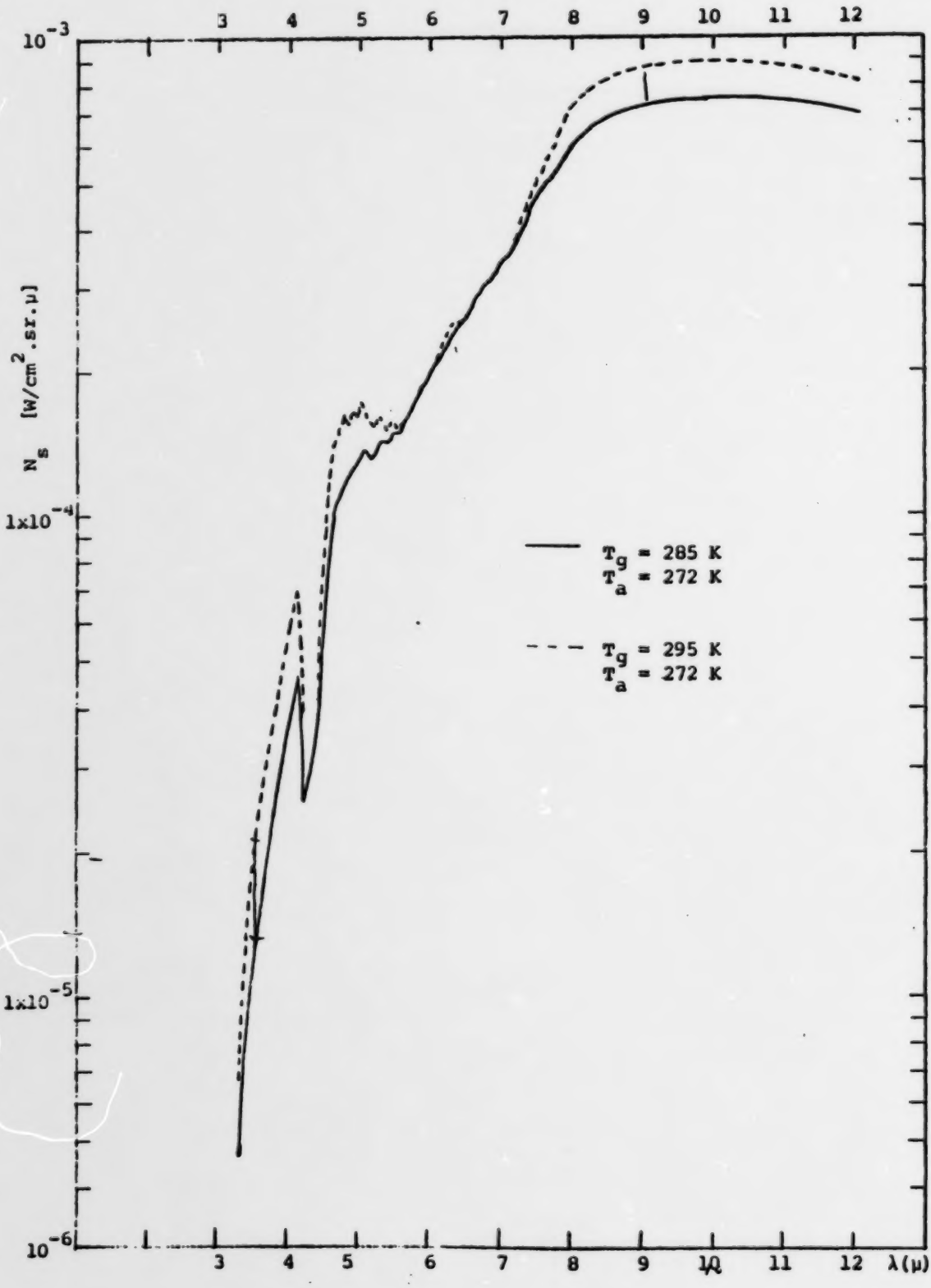

FIGURE 6: Upwelling Radiance at 1.1 km Altitude vs. Wavelength for Two Different Ground Temperatures

1.6 Residual Interfering Gases

The optimum sensitivity and the specificity are expected in the absence of any interfering gases. Any interfering gases will give a false correlation signal (either negative or positive). Furthermore, if the interference gas burden is high, then the optical depth becomes large and the information about the target gas will be reduced and eventually lost completely. Therefore, it is important to choose a spectral band for the target gas where no interfering gases overlap spectrally.

A set of spectra of the important pollutant constituents in the atmosphere is shown in Figure 5. Quantitative estimation of the interference gas effect on the blackbody radiation from the ground was obtained from the LOWTRAN program (Chapter 2) and is plotted in Figure 6. The figure shows no significant absorption by interference gases in the bands of interest at 3.4 μ, 7.8 μ and 11.8 μ.

1.7 Difference Signal in the Presence of the Solar Radiation

Due to the large burden of the atmospheric residual CH_4 and the non-negligible solar radiation flux, we need to consider the effect of the solar radiation on the difference signal at $\lambda = 3.4\ \mu$ (Figure 7).

The total irradiance, N_t, at the objective lens of the instrument can be written as

$$N_t = N_x R T_s T_a + B_s R (1-T_s) T_a + \varepsilon B_e T_a + B_a (1-T_a) \qquad (1\text{-}10)$$

where N_x, B_s, B_e, B_a are solar irradiance on the upper atmosphere, and the blackbody radiances for average sky temperature (between 0 - 20 Km), earth temperature, and air temperature (between 0 - 360 m) respectively, R is the reflection coefficient of the ground. A simplified infinite planar mono-layer of the medium is assumed in this formulation.

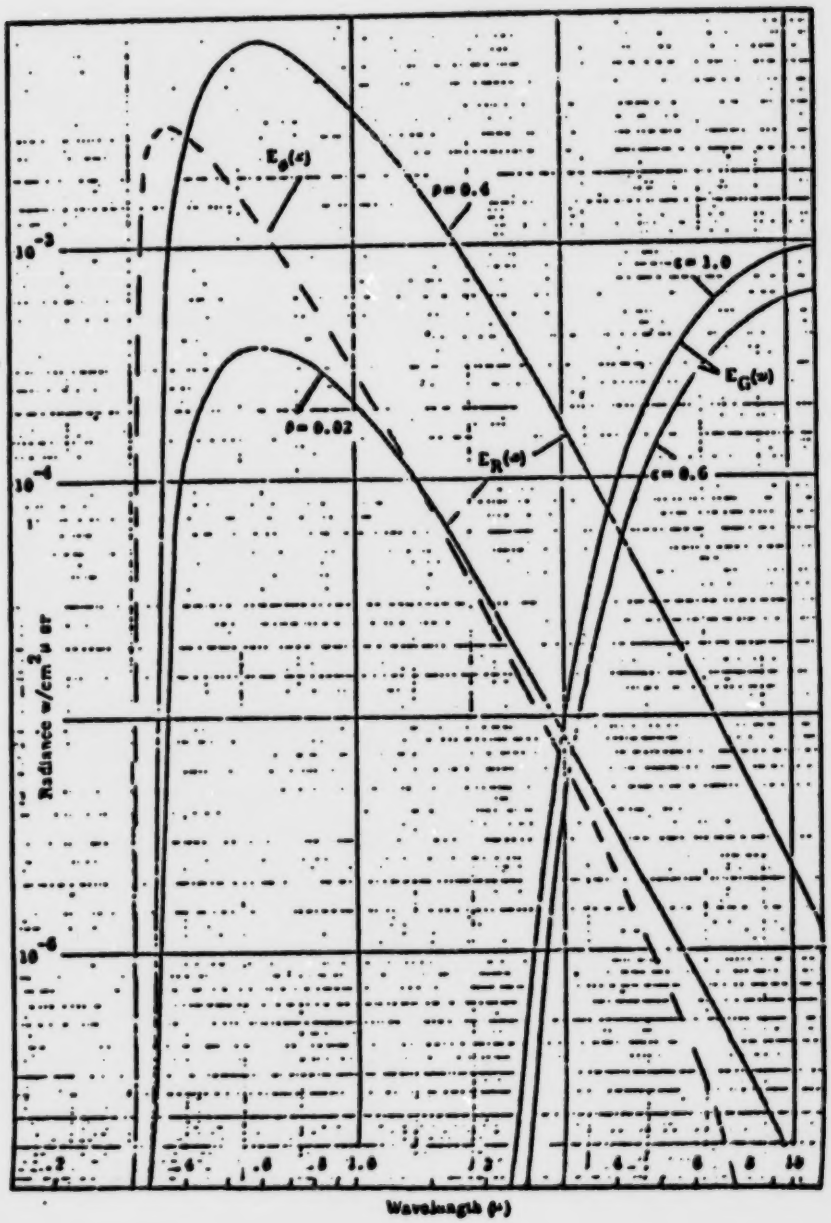

FIGURE 7: Upwelling radiation at the top of atmosphere. Contributions from reflected sun radiation $E_R(\omega)$, atmospheric scattering $E_s(\omega)$, and thermal radiation $E_G(\omega)$. Ground temperature = 300° K, sun zenith angle = 45°, particulate matter according to Elterman 1968.

The difference signal ΔS can be formulated using N_t and following the procedure previously described

$$\Delta S = A\Omega\eta_c \int_{\Delta\nu} \left(N_t T_c - \frac{\eta_r}{\eta_c} N_t T_r \right) d\nu \qquad (1\text{-}11)$$

Substituting equation (1-10) into equation (1-11) and imposing the zero gas balance condition

$$\frac{\eta_c}{\eta_r} = \frac{\bar{T}_r}{\bar{T}_c} \qquad (1\text{-}12)$$

we get

$$\begin{aligned}\Delta S = A\Omega\eta_c \Big[& \bar{N}_x R \left(\overline{T_s T_a T_c} - \overline{T_s T_a}\,\bar{T}_c \right) + \bar{B}_s R \left\{ \overline{(1-T_s) T_a T_c} \right. \\ & \left. - \overline{(1-T_s) T_a}\,\bar{T}_c \right\} + \varepsilon \bar{B}_e \left(\overline{T_a T_c} - \bar{T}_a \bar{T}_c \right) \\ & + \bar{B}_a \left\{ \overline{(1-T_a) T_c} - \overline{(1-T_a)}\,\bar{T}_c \right\} \Big] \Delta\nu \end{aligned} \qquad (1\text{-}13)$$

where $\overline{}$ stands for the average over Δν.

With a simple modification, equation (1-13) can be written as

$$\begin{aligned}\Delta S = A\Omega\eta_c \Delta\nu \Big[& \left(\bar{N}_x - \bar{B}_s \right) R \left(\overline{T_s T_a T_c} - \overline{T_s T_a}\,\bar{T}_c \right) \\ & + \left(\bar{B}_s R + \varepsilon \bar{B}_e - \bar{B}_a \right) \left(\overline{T_a T_c} - \bar{T}_a \bar{T}_c \right) \Big] \end{aligned} \qquad (1\text{-}14)$$

As expected, the difference signal is composed of two parts; one for the correlation of the residual gas (between ground and 20 Km) with the instrument cell gas, and the other the correlation of the residual plus leak gas (between ground and sensor altitude) with the instrument cell gas. Thus the fluctuation of R values, even though the other parameters in the first term remain almost constant, will appear as a fluctuation in the signal, and may generate a false signal.

1.8 Difference Signal of CH_4 at 3.4 μm

The mixing ratio of CH_4 in the air is almost a constant value of 1.4 ppm up to 22 Km. Therefore, the total residual CH_4 gas viewed by the sun (average 60° solar zenith angle) corresponds to about 34.5 torr.M. The average temperature of the air for the scale height is about 260 K. The model calculation shows a very high correlation coefficient of the residual gas for any correlation gas cell conditions.

An estimation shows that the first term in equation (1-14) is approximately 1,000 times higher than the gas leak signal (refer to Chapter 2). Thus, as the ground albedo varies the difference signal will fluctuate with a very large amplitude which is ∿ 1,000 times larger than the leak gas signal. At this wavelength it does not appear to be feasible to measure the ground albedo with 0.1% accuracy, which is required in order to be able to incorporate any signal processing compensation routine.

We conclude that the detection of methane leaks by the use of the 3.4 μ band will be extremely difficult and should not be attempted. This is further supported by the fact that the sensor sensitivity at 3.4 μ decreases very fast as a function of the ground temperature, while the sensitivities at 7.8 μ and 12.2 μ are not as strong a function of the ground temperature (Chapter 4). This results in decreased sensor performance during winter months in the Canadian climate at the 3.4 μ region.

1.9 Footprint Size

The instrument field of view is conceived to be 140 milliradians which will produce ∿ 50 m diameter circular footprint on the ground when operated at an altitude of 350 m. For 120 miles/H (53 m/sec), the footprint spans 26 m in half a second which is the duration of analog data averaging (Chapter 6). For this aircraft speed the spatial resolution deteriorates only by ∿ 20% compared with the instantaneous measurement, while the noise figure improves ∿ 10 times.

Since the chopper wheel revolution can be as fast as 100 Hz and two pairs of gas and reference cells can be accommodated on the chopper, the average span on the ground for one modulation period will be 27 cm. Thus the relative change in footprint during one modulation will be 5.3×10^{-3}.

A linear 30% change in ground emissivity during 0.5 sec will then generate a false signal which is as high as 1.6×10^{-3} of the ground radiance signal. A specific chopper sector configuration (Chapter 4) in a specific data processing routine is applicable to overcome this problem.

2. MODEL CALCULATION

2.1 Introduction

The gas filter correlation technique differs from conventional spectroscopic techniques in the method for obtaining high sensitivity. To maximize the sensitivity of the GFC instrument one has only to select the optimum pressure and length of the correlation cell. The temperature of the cell has a minor influence on the sensitivity of the GFC instrument.

The correlation coefficient also strongly depends on the characteristics of the spectrum of the gas used, such as the ratio of the line width to the line separation and the way the lines are grouped. In order to obtain the quantitative understanding of the behaviour of the correlation coefficient we have developed a simple model calculation.

The code is written in one dimension, for a simple unilayer model atmosphere. Radiation from the source (the ground) is transferred through the atmosphere which contains the target gas and passes through the correlation cell. The parameters for the correlation cell, atmosphere, and the ground are variable in the model. The model uses the available CH_4 gas data for both bands. No interference gases are incorporated in this model.

2.2 LOWTRAN Study

Initially, the LOWTRAN code was evaluated to develop a model for the instrument performance. The LOWTRAN program includes all the interference gases in the atmosphere including aerosols. In spite of the versatility of the program, LOWTRAN has a relatively coarse spectral resolution, which is not sufficient for the specific correlation calculation of interest. Furthermore, the program has a minimum resolution in altitude of 1 Km. Thus we have developed an independent computer code which can be used for evaluation of the correlation coefficient.

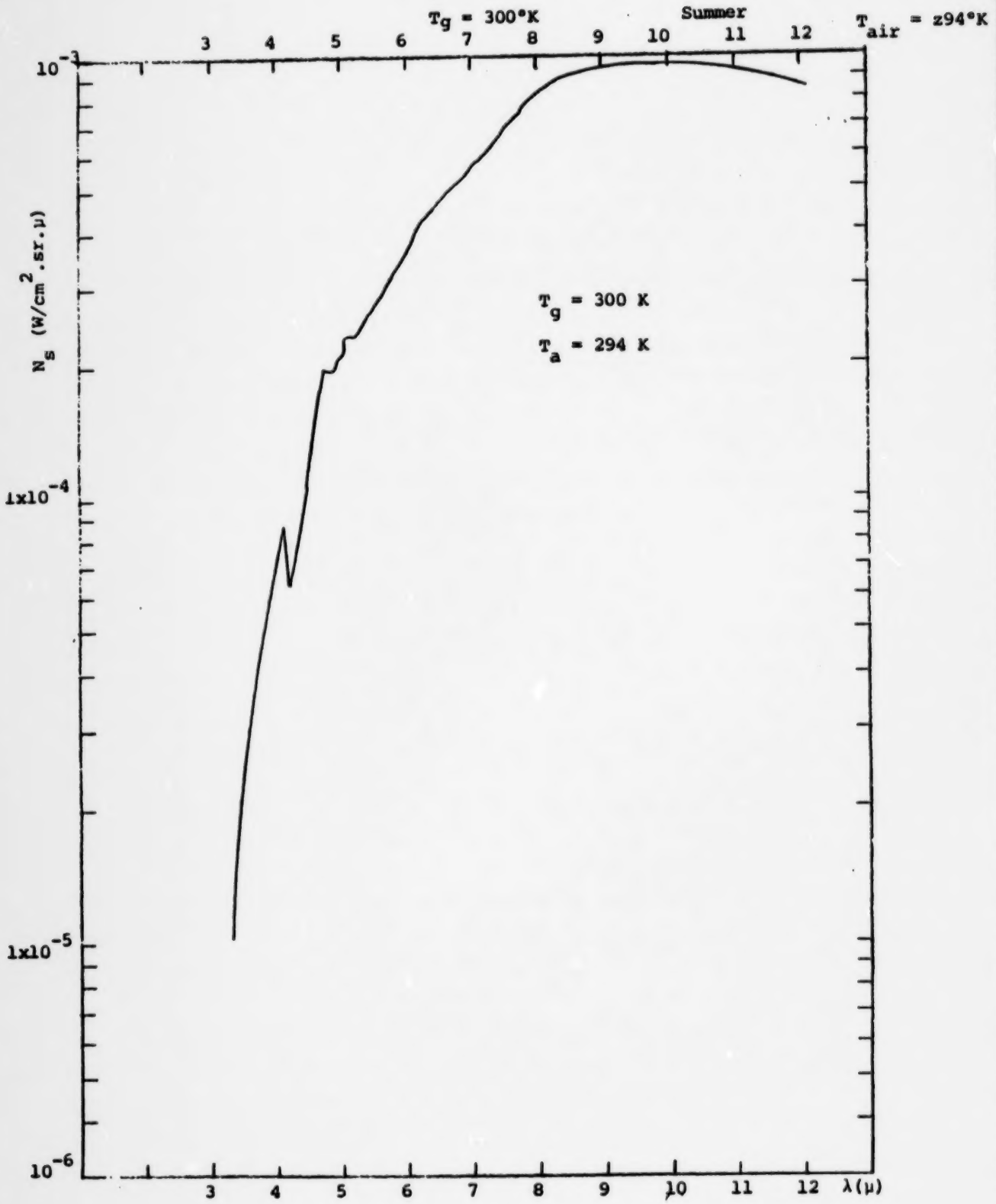

FIGURE 8: LOWTRAN results of a summertime upwelling radiance at 1.1 Km altitude vs wavelength

The LOWTRAN calculation gave the coarse resolution atmospheric transmission and emission characteristics between 3 μ and 12 μ. As shown in Figures 6 and 8, strong CO_2 absorption at around 4.3 μ and H_2O absorption between 4.8 μ and 7.5 μ indicates that the optical depth exceeds 1 for both bands. The absorption by other interfering gases is not noticeable in the spectral range of interest. The influence of the target gas on the transmission coefficient is considered to be minimal (< 1%), thus the radiance spectrum obtained by LOWTRAN can be used for the current study without significant discrepancy.

2.3 High Resolution Modelling

Due to the requirement of high spectral resolution (better than 1×10^{-2} cm^{-1}) we have developed a computer code to calculate the correlation coefficient and difference signal, for a simple unilayer model atmosphere. The ground temperature and albedo, atmospheric layer temperature, the correlation gas cell temperature and pressure may be varied independently in the model. The correlation gas pressure and the cell length are optimized by this modelling, and the results used in the sensor design.

Initially, the ν_3 band of CH_4 at $\lambda = 3.4$ μ was considered in the model without any interferent gases. After implementation of the first model it was extended to the ν_4 band of CH_4 at 7.8 μ. The possibility of incorporating a complete spectrum of the interfering gases at these bands was independently studied by using an AFCRL tape[13], however, the time required to transfer the I/O commands to the PDP-10 proved to be too long to accomplish this task.under the framework of the present contract.

The current model is essentially based on the experimental data of the CH_4 ν_3 and ν_4 band spectra[7]. The data by A.S. Pine[14] lists the spectrum of the ν_3 band of CH_4 including the line position, tetrahedral fine structure patterns, absolute absorption strengths and the atmospheric-pressure broadening and shifts. Data by A. Chedin, et al[15] is used for the ν_4 band.

The correlation integration in equation (1-8) may be written explicitly as

$$(\overline{T_a T_c} - \bar{T}_a \bar{T}_c) = \frac{1}{\Delta\nu}\int_{\Delta\nu} \exp\left\{-(K_a(\nu)\cdot L_a \cdot P_a + K_c(\nu)\cdot L_c \cdot P_c)\right\} d\nu$$

$$- \frac{1}{(\Delta\nu)^2}\int_{\Delta\nu}\exp(-K_a(\nu)\cdot L_a \cdot P_a)\, d\nu \cdot \int_{\Delta\nu}\exp(-K_c(\nu)\cdot L_c \cdot P_c)\, d\nu \qquad (2\text{-}1)$$

The model calculates the correlation coefficient by numerically integrating equation (2-1). In this calculation the correlation cell length L_c, and pressure P_c are parameterized. The absorption coefficient $K(\nu)$ is calculated based on the experimental value of $K_o(\nu_o)$ and including the corrections for the pressure and temperature changes.

The temperature dependence of the line strength $S(T)$, is considered via the partition function and lower state population as

$$S(T) = S_o \left(T/T_o\right)^{1.5} \exp\left\{\frac{1.439 \cdot E''\cdot (T-T_o)}{T_o T}\right\} \qquad (2\text{-}2)$$

where S_o is the line strength at temperature T_o = 296 K. The lower state energy E'' is calculated as[16]

$$E'' = B_o j(j+1) - D_o [j(j+1)]^2$$

and $$B_o = 5.2412 \text{ cm}^{-1} \qquad (2\text{-}3)$$

$$D_o = 1.14 \times 10^{-4} \text{ cm}^{-1}$$

The absorption coefficient $K(\nu)$ is calculated by assuming a Lorenzian line shape[14] as

$$K(\nu) = \frac{S\alpha}{\pi\left[(\nu-\nu_o)^2 + \alpha^2\right]} \qquad (2\text{-}4)$$

In this equation S is calculated according to equation (2-2) and S_o is obtained from the experimental $K_o(\nu_o)$ value at T_o = 296 K by

$$S_o = \pi \alpha_o S K_o(\nu_o) \qquad (2\text{-}5)$$

The half width is corrected for the temperature and pressure variation neglecting Doppler broadening as

$$\alpha = \alpha_o \frac{P}{P_o} \sqrt{T_o/T} \qquad (2\text{-}6)$$

where $\alpha_o = 0.059\ cm^{-1}$ [8] at $P_o = 1$ atm and $T_o = 296$ K.

In evaluating $K(\nu)$ at a fixed ν, all the lines within $\pm 12\ cm^{-1}$ windows are considered and the contribution from each line is summed up to give the total $K(\nu)$ value. The $K(\nu)$'s are calculated separately for the CH_4 in the atmosphere and the CH_4 in the correlation cell.

The integration is carried out numerically for a given set of P_c, T_c and L_c. Having done this, the entendue $A\Omega$, the transmission coefficient of the window materially η_r and the radiation term $(\varepsilon \bar{B}_e - \bar{B}_a)$ is multiplied to the integration and the difference signal ΔS is calculated. A schematic flow chart is shown in Figure 9.

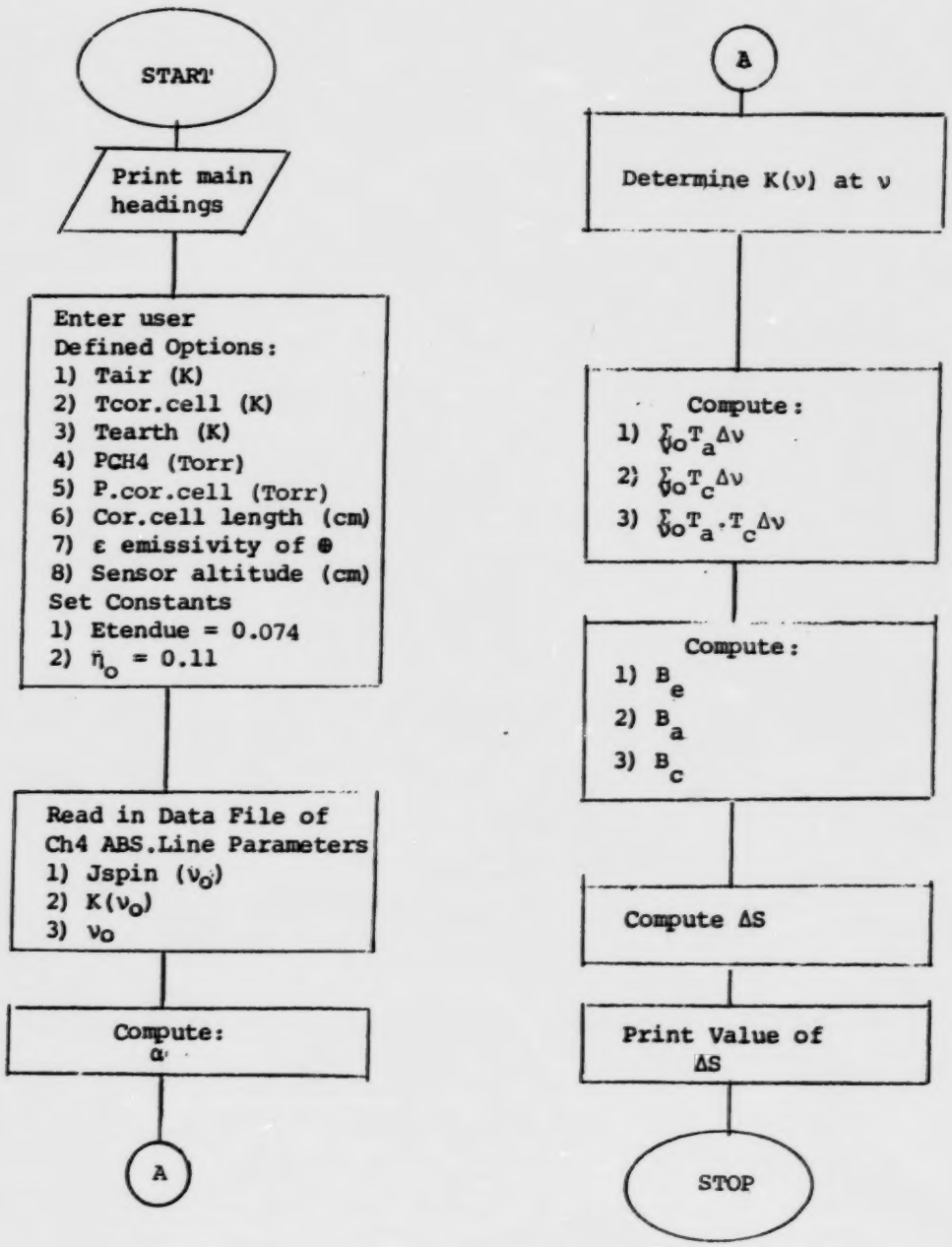

FIGURE 9: Flowchart of the code calculation

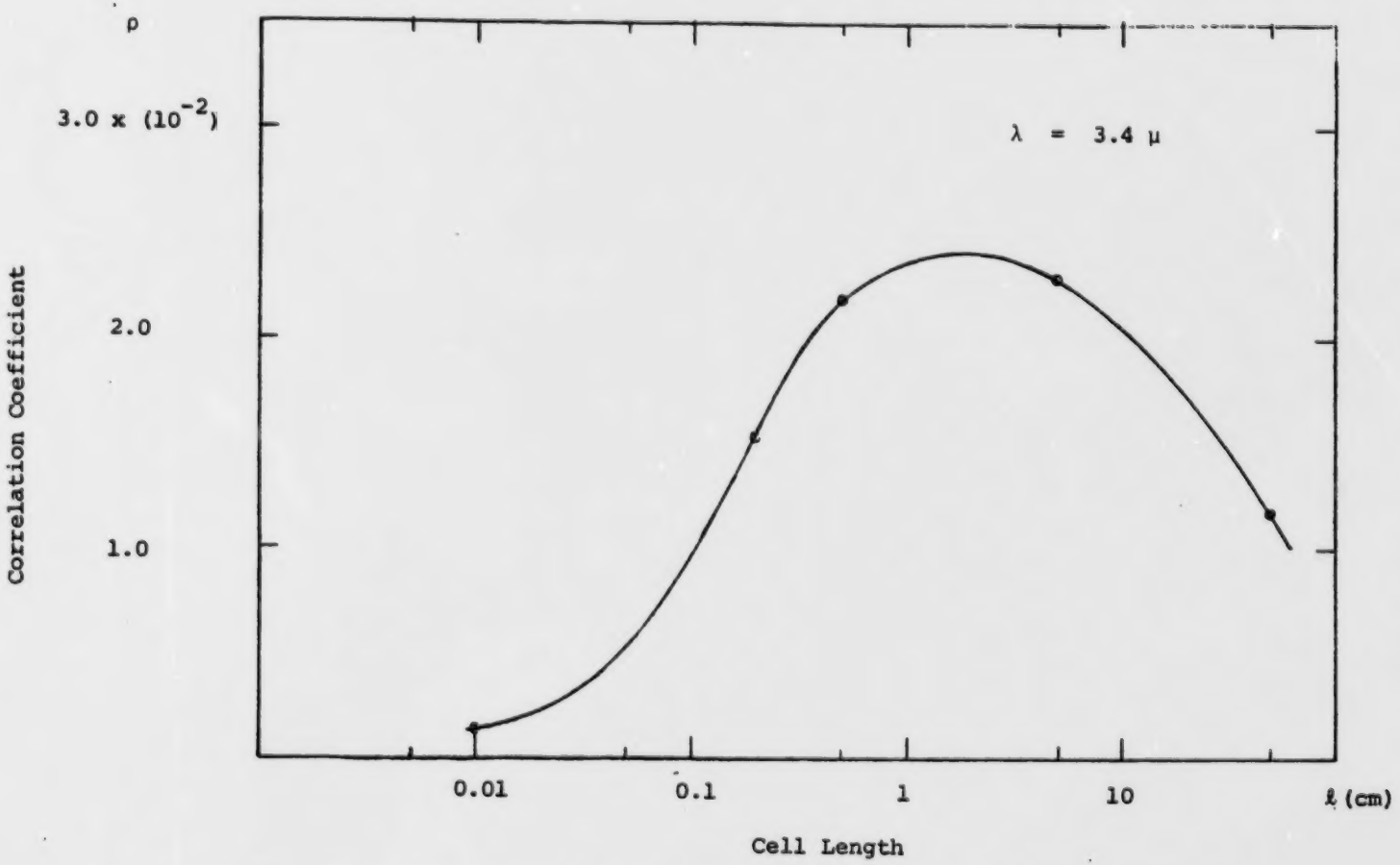

FIGURE 10: The correlation coefficient for 1.4×10^{-3} torr x 350 m residual CH_4 gas (the background amount) as a function of the cell length

2.3.1 Results of The Model Calculation at 3.4 μm

The model calculation has been carried out for the set of spectroscopic data[14]. The validity of the model has been confirmed by testing the general feature of the correlation coefficient, $\rho \equiv (\overline{T_a T_c} - \overline{T}_a \overline{T}_c)$. As shown in Figure 10, for a given atmospheric CH_4 burden, ρ increases as a function of correlation gas cell length, ℓ, until a certain point, and decreases for very large ℓ values. This means that for very large ℓ values the CH_4 spectrum becomes extremely broad so that very little correlation with the sharply defined target gas spectrum is obtained.

The correlation coefficient, ρ_ℓ, for 10 ppm.M leak gas is calculated by taking the equivalent increase of ρ at the nominal residual CH_4 gas burden. Figure 11 shows ρ_ℓ as a function of the cell length, ℓ. ρ_ℓ increases as a function of ℓ and starts to turn around at ℓ = 1 cm.

The correlation coefficient for the total residual CH_4 gas of twice the atmospheric height (a 60° solar zenith sun approximation to equivalent path) is also computed and plotted in Figure 12 as a function of ℓ. Comparing Figures 11 and 12, one may conclude that it is impossible to reduce the $(\overline{T_a T_s T_c} - \overline{T_a T_s} \overline{T}_c)$ term in equation (7) below the value of $(\overline{T_a T_c} - \overline{T}_a \overline{T}_c)$ by varying the cell length.

The correct average absorption coefficient $\bar{\alpha}$ = 0.61 / atm.cm has also been obtained by computation.

Throughout the computation we have used 1 atm CH_4 in the correlation cell, T_{earth} = 300 K, T_{air} = 298 K, T_{cell} = 296 K, and 350 m sensor altitude unless specified otherwise.

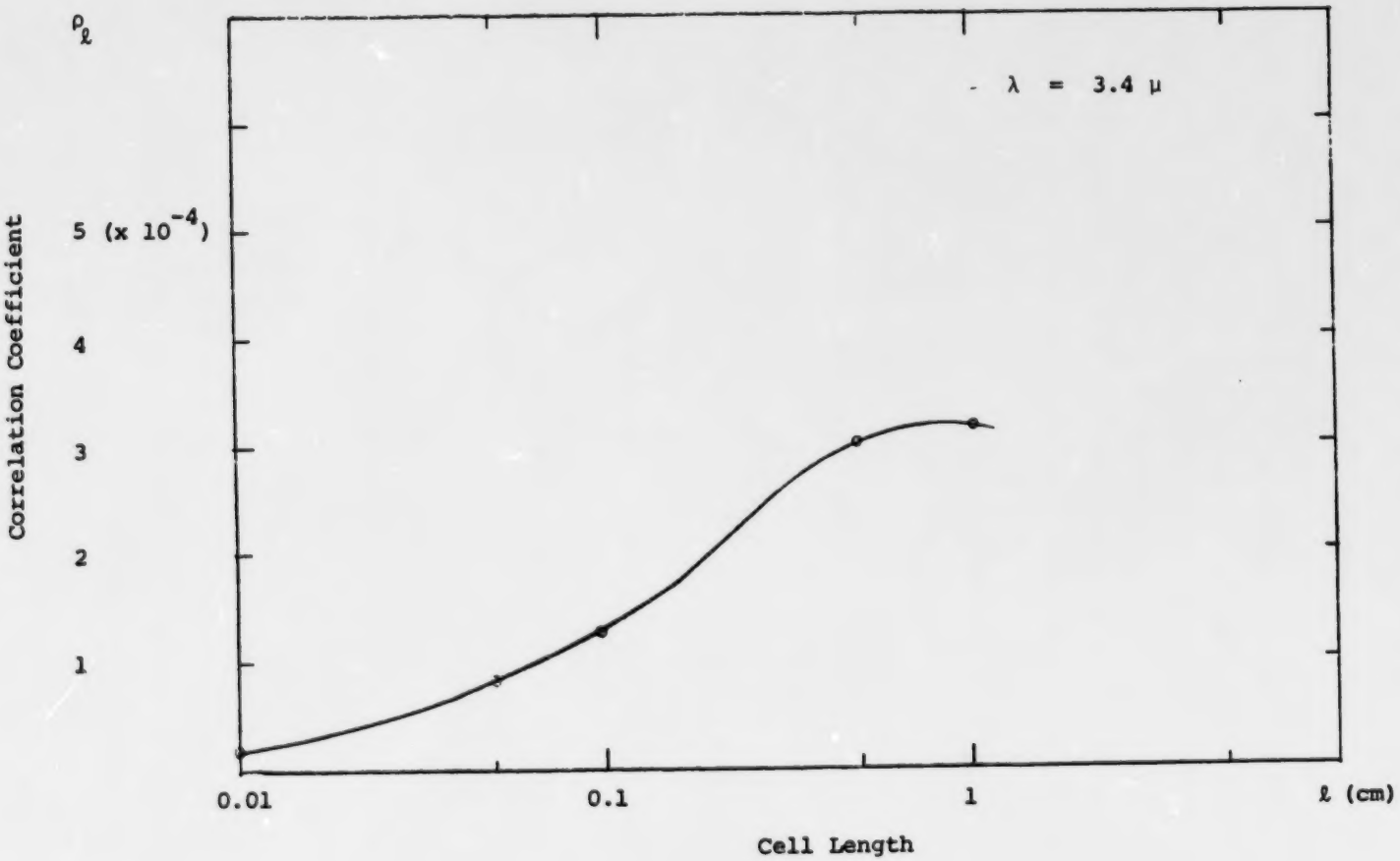

FIGURE 11: The correlation coefficient for 10 ppm.M CH_4 leak gas as a function of the cell length.

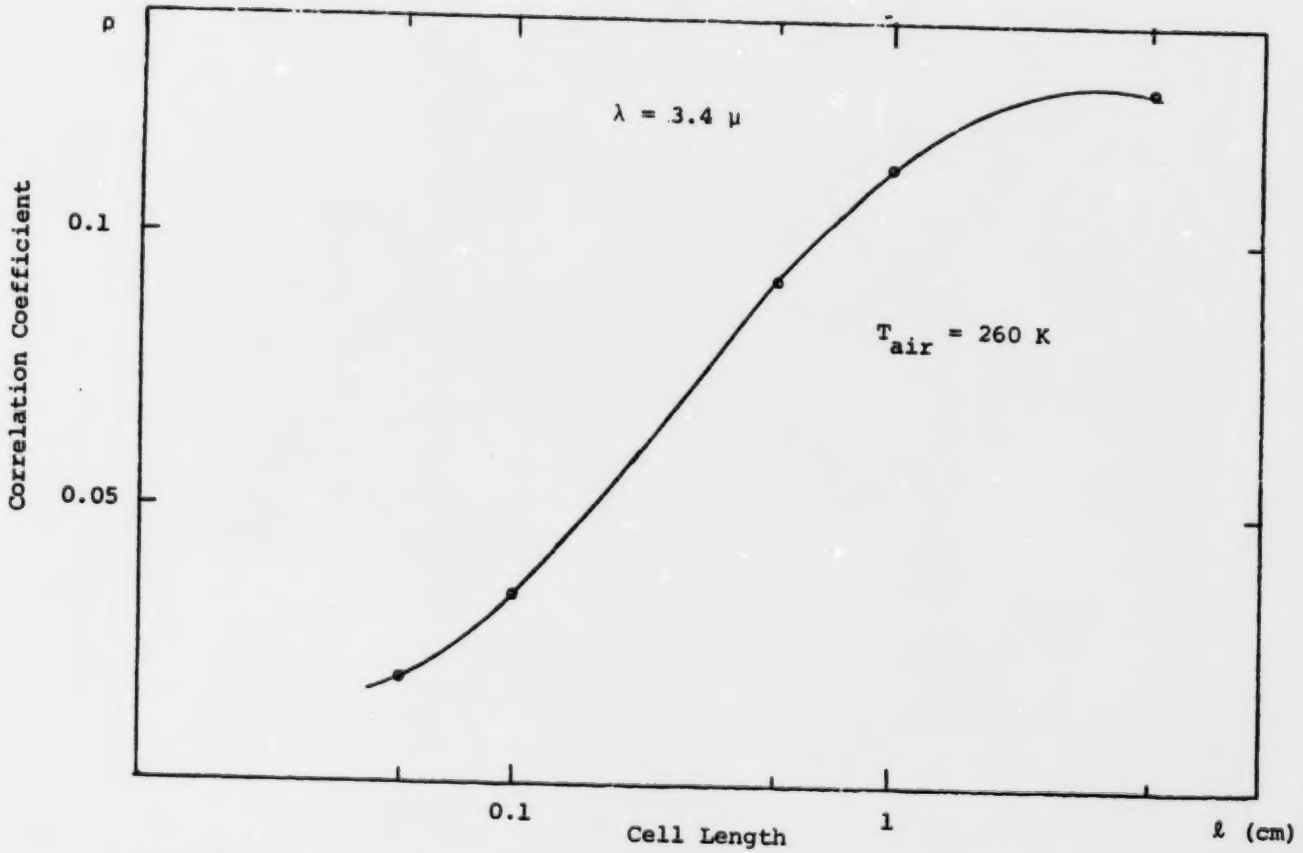

FIGURE 12: The correlation coefficient of the total residual CH_4 for 2X scale height (24.5 torr.M)

Temperature effects on the correlation coefficient have also been studied by changing the cell temperature to 290 K while maintaining all other parameters at the same temperatures. As shown in Figure 13, the general features of the correlation coefficient are not affected by the temperature change, although the absolute value of the correlation coefficient shows a noticeable change. Knowing that the slope of the correlation coefficient is directly proportional to the instrument sensitivity, the optimum correlation gas (cℓ) value remains the same for the temperature change. It is interesting to note that the correlation coefficient is noticeably decreased by lowering the temperature of the correlation gas, showing that the two spectra go out of match as the difference between the target gas and correlation gas temperatures increases. It suggests that the average transmittance of the gas changes significantly. The temperature gradient of transmittance at 296 K shows $\frac{dT}{d\theta} = 9.5 \times 10^{-4}/K$ at 3.4 μ. $\frac{dT}{d\theta} = 3.3 \times 10^{-4}/K$ at 7.8 μ. This also suggests that the temperature of the correlation gas should be maintained as close as possible to the target temperature, in order to optimize the instrument sensitivity. The influence of the temperature variation on the correlation coefficient has also been studied by taking the gradient of ρ at operating temperature. The result shows that $\frac{d\rho}{d\theta} = 9 \times 10^{-5}/K$ at 3.4 μ and $\frac{d\rho}{d\theta} = 9.3 \times 10^{-6}/K$ at 7.8 μ. This indicates that the variation in the correlation coefficient due to a few degree temperature change will be insignificant compared with the detector NEP.

The band width of the spectrum has also been varied in the calculation. As shown in Figure 14 the increase of the band width increases the absolute magnitude of the correlation coefficient without deteriorating the slope (sensitivity). This suggests that the sensitivity of the instrument is maximized by utilizing as much of the absorption band as possible. The sensitivity of the instrument is shown to be linearly proportional to the spectral window as shown in equation (1-8).

However, as the spectral filter window is broadened the potential for interference gas spectra may increase. Examination of the interferent spectra in Figure 5 leads to the recommended spectral filter location of 7.8 μ centre wavelength and 0.4 μ band width.

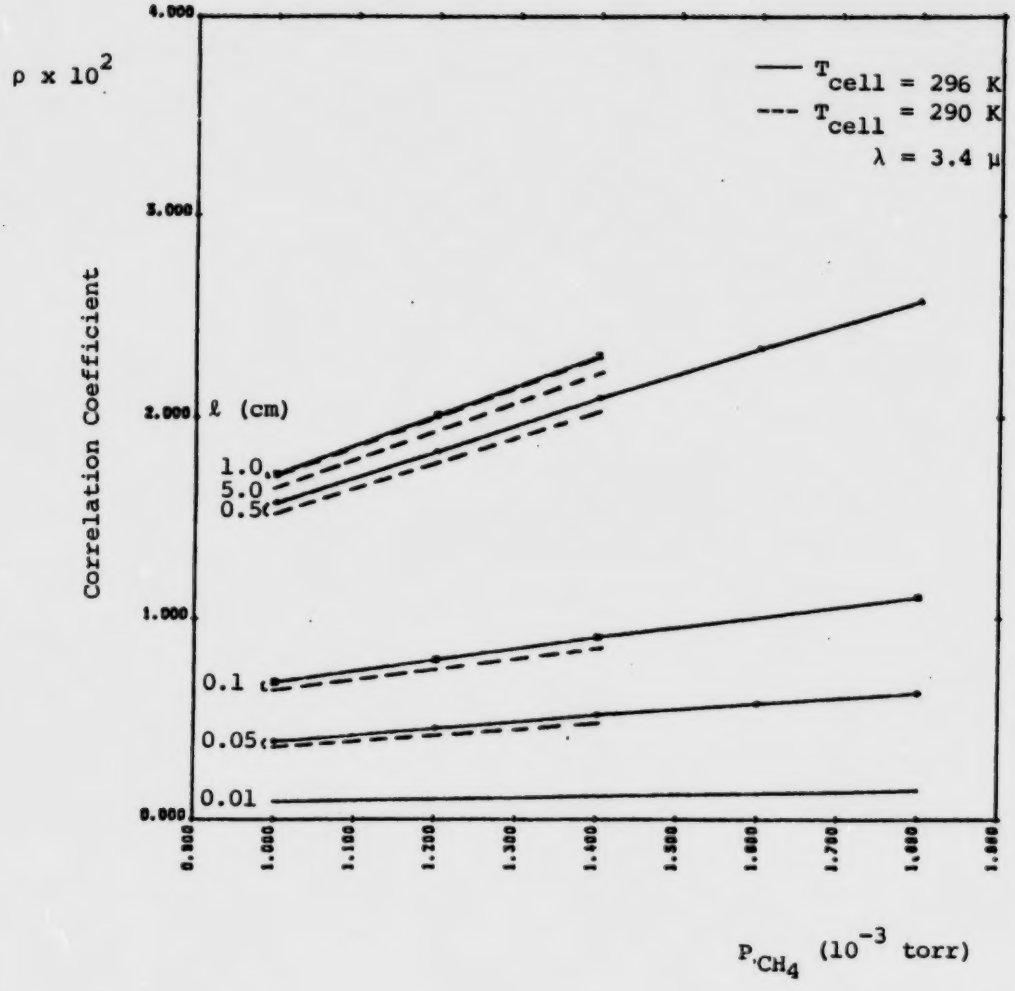

FIGURE 13: Correlation coefficients as a function of the partial pressure of CH_4 in the air

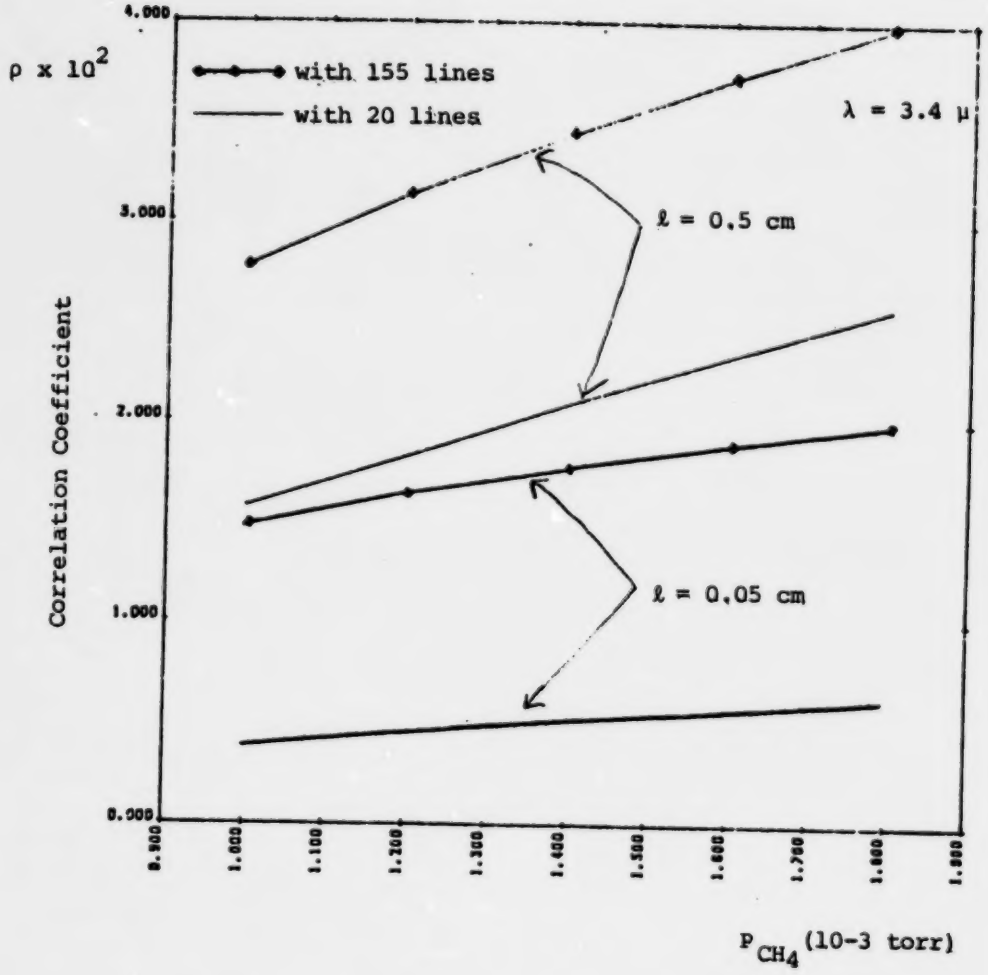

FIGURE 14: Correlation coefficients as a function of the partial pressure of CH_4 in the air

2.3.2 Results of the Model Calculation at 7.8 μm

The same code as used in the 3.4 μ band calculation, has been used at the 7.8 μ calculation with a slight modification in data input format. A set of data for line position, line strength, lower state energy, and the line width, has been obtained from the results of A. Chedin, et al[15] and read into the code. This data has also been cross-checked with other data[17,18]. Again, the calculation is based on T_{earth} = 300 K, T_{air} = 298 K, T_{cell} = 296 K, 1 atm CH_4 in the cell and 350 m sensor altitude unless specified otherwise.

The correlation coefficient for the residual CH_4 gas burden (1.4 ppm.350 m) has been calculated for various cell lengths and plotted in Figure 15. As expected the correlation increases with the cell length to the maximum value (3.5×10^{-3}) and decreases for further increase of the cell length. It is interesting to note that the rate of increase in this band is very much smaller than that of the 3.4 μ band.

The correlation coefficient for 10 ppm.M of CH_4, ρ_ℓ has also been calculated and shown in Figure 16. The ρ_ℓ value increases with the cell length up to $\ell \sim 5$, which means the optimum cell length for 7.8 μ band is larger than 1 cm. The value of ρ_ℓ at 7.8 μ is smaller than that at 3.4 μ by a factor 5 and originates from the low absorption coefficient of the ν_4 band at 7.8 μ.

The correlation coefficient, ρ_ℓ for T_{air} = 251 K and T_{cell} = 296 K has also been calculated and plotted in Figure 16 in order to simulate a measurement under typical winter conditions. Comparing the two results, one can conlude that the large temperature difference, in winter, deteriorates the correlation coefficient. With a 1 cm cell length, the correlation coefficient for T_{air} = 251 K is estimated to be 0.6 times of that for T_{air} = 298 K. The instrument sensitivity will thus be decreased by a factor of 0.6 in winter compared with summer conditions due to the decrease in the correlation coefficient, if a constant cell temperature, 296 K, is maintained.

The correlation coefficient obtained here has been used to evaluate the detection limit of the instrument and is listed in Table 2 of the next chapter.

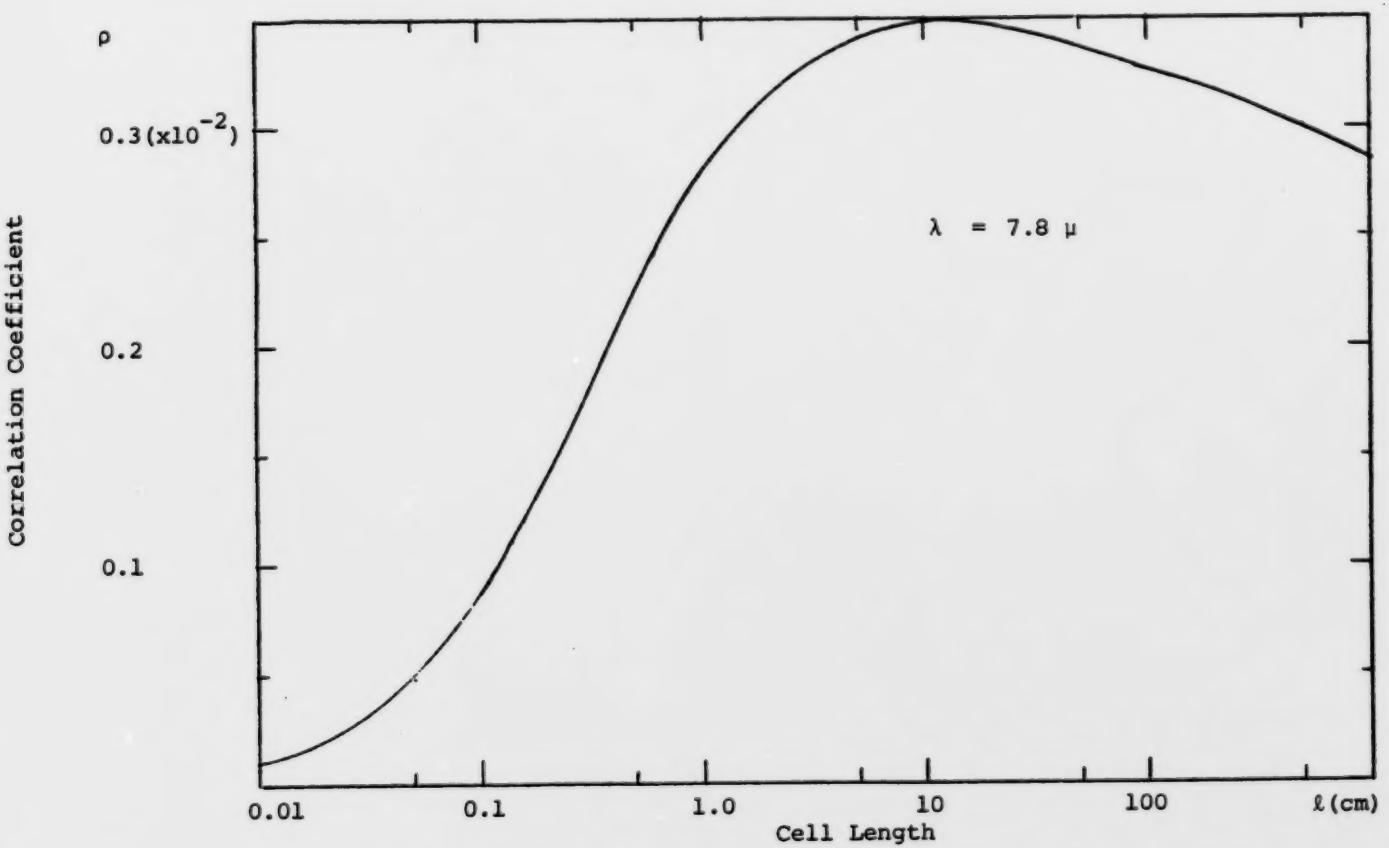

FIGURE 15: The correlation coefficient for 1.4 x 10^{-3} torr x 350 m residual CH_4 gas as a function of the cell length

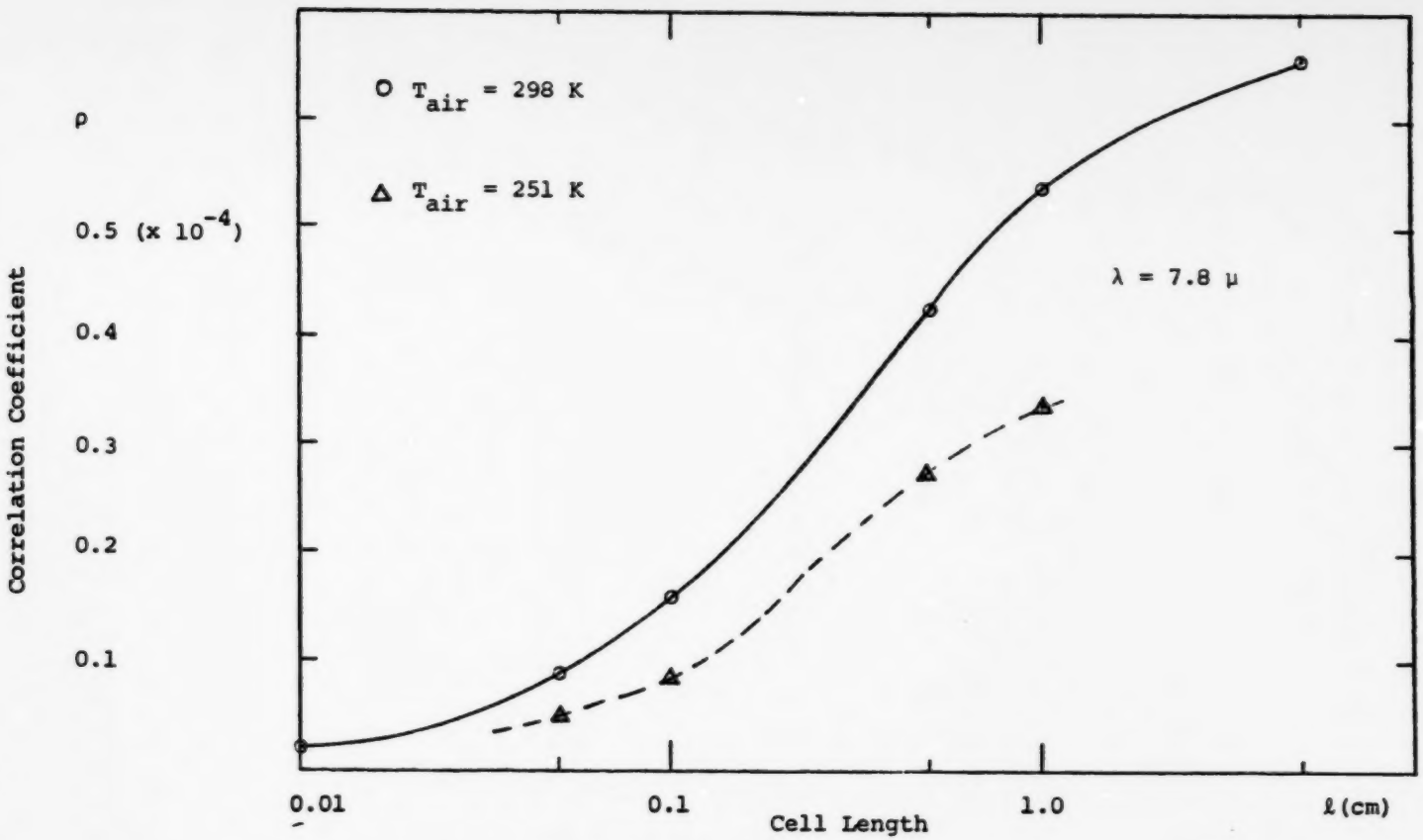

FIGURE 16: The correlation coefficients for 10 ppm.M CH_4 leak gas as a function of the cell length

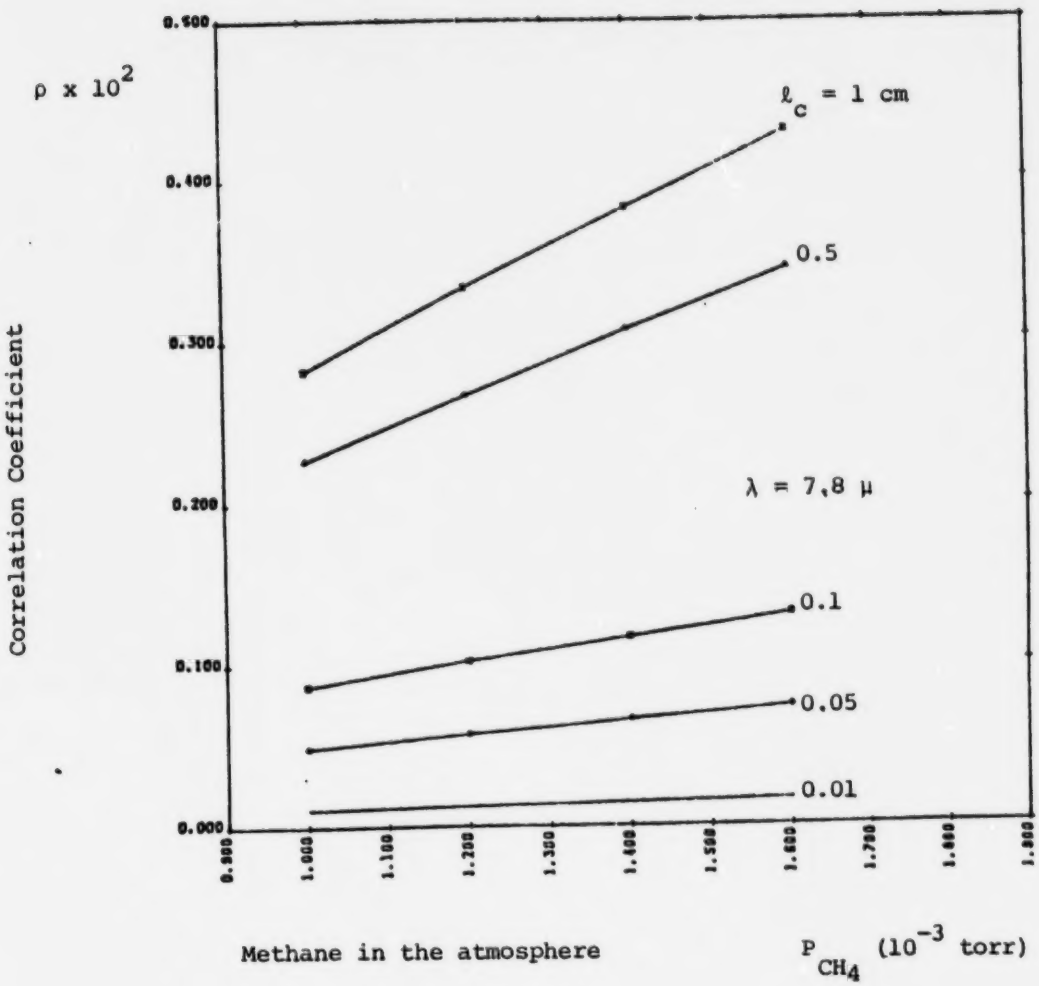

FIGURE 17: Correlation coefficients as a function of the partial pressure of CH_4 in the air

2.3.3 Ethane Spectrum

The features of the ethane spectra are generally more complicated than those of methane. In the ethane spectra the lines are located very close together. The widths (FWHM) of the ethane lines in the ν_7 band at atmospheric pressure are about 0.1 cm^{-1} with an average separation of about 0.2 cm^{-1}, as shown in the following figure thus the lines do not overlap each other seriously, However, as the optical depth of the correlation cell is increased, the line structure will diffuse very rapidly. Therefore, it is important not to overpressurize the gas cell in order to optimize the correlation coefficient.

In the GFC technique, the correlation coefficient is generally optimized for a few percent absorption coefficient of the correlation gas. Considering the high line density in the ethane spectrum, a few percent absorption coefficient can easily be obtained without serious saturation at the line peaks. Therefore, we expect to achieve a high correlation efficiency for ethane for a relatively low pressure compared with the methane case.

Interference between ethane and methane has been considered as a drawback in the 3.4 μ band measurement.

In order to show the interference the methane spectrum (dotted lines) have been laid on top of the ethane spectrum. There is a distinctive difference between the two spectra; the methane lines are separated by 8 cm^{-1} typically and ethane lines by 0.2 cm^{-1}. In terms of the cross-correlation between the two spectra, the ethane spectrum resembles a flat band compared with the methane spectrum. Consequently, the cross-correlation will be minimal and the interference will be negligible.

2.4 Gas Dispersion Model

The relationship between the gas leak rate and the atmospheric mixing ratio is of interest. An existing gas dispersion model has been used here with minor modification. The model calculates vertically integrated leak gas

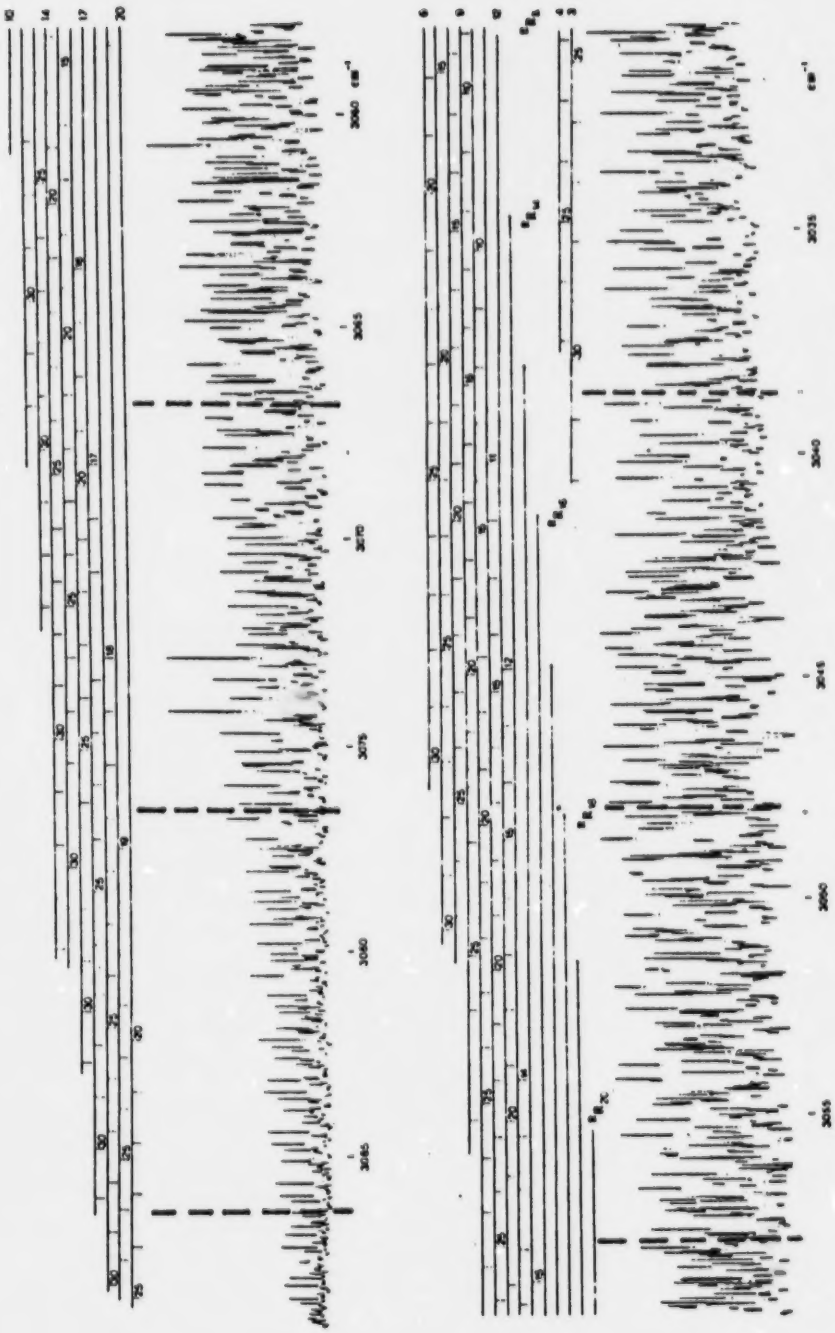

Survey spectrum of the upper region of ν_7 of C_2H_4, with assignments. Below 3042 cm^{-1}, the pressure was halved.

concentration and averages for the footprint size. The code is one dimensional. Various classes of PASQUILL-GIFFORD stability are applied in the model.

A typical result of the model calculation for the methane leak is given in the following table.

The preliminary results demonstrate that under the modelled conditions we expect to see about 100 ppm.M leak gas concentration within 40 m downwind distance. The gas concentration decreases at further downwind distances. The stability class has a minor effect on the gas dispersion.

RUN FORT
INPUT WIND SPEED(M/S): 2.
INPUT LEAK RATE(M**3/S): 0.01
INPUT SENSOR FOOTPRINT(M): 10.

VERTICALLY INTEGRATED CONCENTRATION FOR VARIOUS DOWNWIND DISTANCE

FOR PASQUILL STABILITY CLASS, A, THE VERTICAL CONCENTRATIONS ARE EXPRESSED IN PPM-M FOR DISTANCES OF 10-1000 METRES FROM THE SOURCE

	10	20	30	40	50	60	70	80	90	100
0	100.0000	99.9995	99.7593	97.7230	93.1654	87.1411	80.7507	74.6098	68.9721	63.9086
100	59.4015	55.4004	51.8462	48.6811	45.8528	43.3158	41.0310	38.9651	37.0899	35.3813
200	33.8195	32.3366	31.0679	29.9507	28.9241	27.9786	26.7059	25.7997	24.9509	24.1559
300	23.4119	22.7113	22.0515	21.4291	20.8410	20.2845	19.7571	19.2566	18.7810	18.3286
400	17.8977	17.4868	17.0945	16.7197	16.3612	16.0179	15.6890	15.3735	15.0706	14.7797
500	14.5000	14.2308	13.9717	13.7220	13.4812	13.2489	13.0247	12.8081	12.5987	12.3963
600	12.2003	12.0107	11.8270	11.6489	11.4763	11.3089	11.1464	10.9886	10.8354	10.6865
700	10.5418	10.4010	10.2641	10.1308	10.0011	9.8748	9.7517	9.6317	9.5148	9.4007
800	9.2895	9.1809	9.0749	8.9715	8.8705	8.7717	8.6753	8.5810	8.4889	8.3987
900	8.3106	8.2243	8.1399	8.0573	7.9764	7.8972	7.8196	7.7435	7.6690	7.5960

FOR PASQUILL STABILITY CLASS, B, THE VERTICAL CONCENTRATIONS ARE EXPRESSED IN PPM-M FOR DISTANCES OF 10-1000 METRES FROM THE SOURCE

	10	20	30	40	50	60	70	80	90	100
0	100.0000	100.0000	99.9970	99.8259	98.7798	96.3344	92.6860	88.3291	83.7022	79.0969
100	74.6794	70.5314	66.6840	63.1393	59.8945	56.8996	54.1620	51.6489	49.3384	47.2103
200	45.2463	43.4301	41.7470	40.1839	38.7292	37.3727	36.1053	34.9189	33.8063	32.7610
300	31.7774	30.9504	29.9753	29.1480	28.3648	27.6224	26.9177	26.2480	25.6108	25.0037
400	24.4249	23.8723	23.3443	22.8393	22.3558	21.8925	21.4482	21.0218	20.6121	20.2183
500	19.8395	19.4748	19.1234	18.7847	18.4580	18.1426	17.8380	17.5436	17.2590	16.9837
600	16.7172	16.4591	16.2090	15.9665	15.7314	15.5033	15.2818	15.0668	14.8579	14.6548
700	14.4574	14.2653	14.0784	13.8965	13.7194	13.5469	13.3788	13.2149	13.0552	12.8993
800	12.7473	12.5989	12.4541	12.3126	12.1745	12.0395	11.9076	11.7786	11.6526	11.5293
900	11.4086	11.2906	11.1751	11.0620	10.9512	10.8428	10.7365	10.6325	10.5305	10.4305

FOR PASQUILL STABILITY CLASS, C, THE VERTICAL CONCENTRATIONS ARE EXPRESSED IN PPM-M FOR DISTANCES OF 10-1000 METRES FROM THE SOURCE

	10	20	30	40	50	60	70	80	90	100
0	100.0000	100.0000	100.0000	99.9995	99.9733	99.7629	99.0852	97.7499	95.7570	93.2338
100	90.3479	87.2545	84.0769	80.9045	77.7981	74.7964	71.9221	69.1869	66.5949	64.1453
200	61.8342	59.6557	57.6030	55.6688	53.8456	52.1262	50.5034	48.9705	47.5214	46.1501
300	44.8512	43.6196	42.4508	41.3403	40.2843	39.2791	38.3213	37.4078	36.5359	35.7028
400	34.9061	34.1437	33.4134	32.7133	32.0416	31.3968	30.7772	30.1815	29.6084	29.0566
500	28.5250	28.0125	27.5192	27.0411	26.5803	26.1351	25.7046	25.2882	24.8853	24.4951
600	24.1171	23.7508	23.3955	23.0509	22.7165	22.3917	22.0763	21.7699	21.4719	21.1822
700	20.9004	20.6261	20.3591	20.0990	19.8457	19.5989	19.3582	19.1236	18.8947	18.6714
800	18.4534	18.2407	18.0329	17.8299	17.6316	17.4378	17.2483	17.0631	16.8819	16.7047
900	16.5312	16.3615	16.1953	16.0326	15.8732	15.7171	15.5642	15.4143	15.2674	15.1233

3. SIGNAL TO NOISE CALCULATION

3.1 Electronic Noise

The signal channel is conceived to operate as

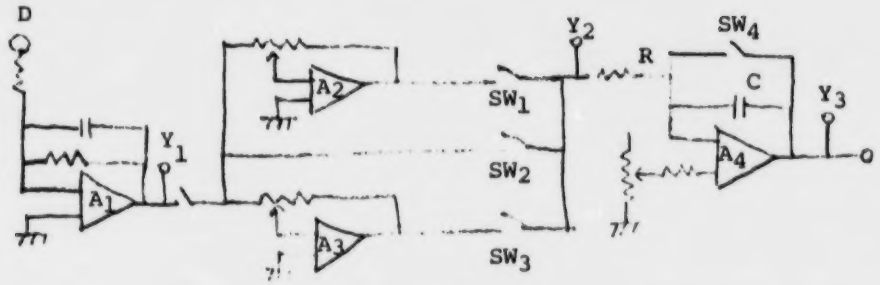

We shall write the offset and gain of each amplifier as

$$Y_i = G_i (S + B_i) \tag{3-1}$$

where G_i and B_i are the gain and offset of amplifier A_i referred to the input, S, and Y_i is the output. The offset B is assumed to contain all noise terms and drift terms. Three signals appear from the detector; S_g for the correlation gas cell, S_r for the reference cell, and S_b for the blank sector.

The signal Y_3 is given by

$$Y_3 = \frac{T_1}{RC} \left[G_1 (S_g + B_1) - G_2 \{ G_1 (S_r + B_1) + B_2 \} - G_3 \{ G_1 (S_b + B_1) + B_3 \} + \frac{T}{T_1} B_4 \right] \tag{3-2}$$

where T_1 is the time during which switches SW_1, SW_2 and SW_3 are closed and T is the time during which switch SW_4 is closed.

The effect of the temperature fluctuation on the signal Y_3 may be estimated by taking temperature gradient $\frac{dY_3}{d\theta}$, where θ is the temperature.

With simple algebra one can write

$$\left|\frac{dY_3}{d\theta}\right| = \left|\frac{T_1}{RC}\left[\frac{dG_1}{d\theta}(S_g - G_2S_r - G_3S_b) - G_1\left(\frac{dG_2}{d\theta}S_r + \frac{dG_3}{d\theta}S_b\right) + \left(\frac{dG_1}{d\theta}B_1 + G_1\frac{dB_1}{d\theta}\right)(1 - G_2 - G_3) - G_1B_1\left(\frac{dG_2}{d\theta} + \frac{dG_3}{d\theta}\right) - \frac{dG_2}{d\theta}B_2 - G_2\frac{dB_2}{d\theta} - \frac{dG_3}{d\theta}B_3 - G_3\frac{dB_3}{d\theta} + \frac{T}{T_1}\frac{dB_4}{d\theta}\right]\right| \quad (3\text{-}3)$$

The first and third terms are zero in the absence of the gas leak (Chapter 7). Typical values for B_iS, G_iS and their temperature gradient are estimated as follows

$$B_i \simeq 10^{-5}\,V,\ \frac{1}{G_i}\frac{dG_i}{d\theta} \simeq 2\times10^{-5}/K,\ \frac{dB_i}{d\theta} \simeq 10^{-5}/K,\ \frac{T_1}{RC} \simeq 1$$

$$G_2 \simeq 1,\ G_3 \simeq 10^{-2},\ G_1 \leq 2\times10^{4}.$$

For this value the last six terms in equation (3-3) are estimated to be negligible thus $\frac{dY_3}{d\theta}$ becomes

$$\left|\frac{dY_3}{d\theta}\right| \simeq \frac{T_1}{RC}G_1S_r\left|\frac{dG_2}{d\theta}\right| \quad (3\text{-}4)$$

From equation (3-4) one can derive

$$\frac{1}{G_1S_r}\left|\frac{dY_3}{d\theta}\right| \simeq \frac{T_1}{RC}\left|\frac{dG_2}{d\theta}\right| \simeq 2\times10^{-5} \quad (3\text{-}5)$$

In conclusion the fractional thermal drift for 1°K change is estimated to be 2×10^{-5}.

The effect of noise in amplifiers A_1, A_2 and A_3 has also been considered. Amplifier A_3 has a noise bandwidth which is determined by the interval T ∿ 1 sec for which SW3 is open, i.e., at a frequency of ∿ 1 Hz. The noise generated in amplifier A_2 is not synchronously rectified; since the gas filter wheel rotates through a half revolution to create the difference signal, the amplifier A_2 generates noise at a frequency $\frac{f_o}{2}$ where f_o is the chopping frequency (∿ 100 Hz). Finally amplifier A_1 has a noise component at the chopping frequency.

All amplifiers are assumed to be LF351's. The noise voltage generator is assumed to have a $^1/f$ characteristic below 10 Hz. The noise contributions are:

f(Hz)	e_n (nv/√Hz)
1	300
10	30
50	20
100	15

The gain of amplifier A_1 must also be estimated. This term is dependent on the desired signal level presented to the synchronous detector (assumed to be 10 V) and on the estimated signal level. The noise contributions are indicated in the following table. The fractional noise contribution is the noise-to-signal ratio. Use of a photovoltaic HgCdTe detector implies that G_1 have values similar to the PbS case, however, the D* for such a detector is smaller than for the photoconductive PbS.

The detector noise levels and responsivities for Δf = 1.7 Hz have been estimated below:

λ	3.4 μm	7.8 μm	11.5 μm	
Detector Type	PbS Photoconductive	HgCdTe Photoconductive	HgCdTe Photoconductive	
Area	.01	.01	.01	cm^2
D*(minimum)	1.5×10^{11}	5×10^{9}	8×10^{9}	$\frac{cmHz^{\frac{1}{2}}}{w}$
NEP/$(\Delta f)^{\frac{1}{2}}$	6.7×10^{-13}	2×10^{-11}	1.25×10^{-11}	$\frac{w}{\sqrt{Hz}}$
Responsivity	5×10^{5}	1.3×10^{3}	6×10^{2}	v/w
Electronic Noise	4.4×10^{-7}	3.4×10^{-8}	7.5×10^{-9}	$v/\sqrt{Hz}$

NOISE CONTRIBUTIONS AT INPUT

Optical Power W	Detector Output V	Amplifier Gain G_1	Pbs Detector (3.4μm) ($v/\sqrt{Hz}$)	Amplifier A_1 $v/\sqrt{Hz}$	Amplifier A_2 $v/\sqrt{Hz}$	Amplifier A_3 $v/\sqrt{Hz}$	e_{total} $v/\sqrt{Hz}$	Noise Voltage v	Fractional Noise Components	Fractional Thermal Drift G_1S = 10V (1°C change)
10^{-7}	5×10^{-2}	200	3.3×10^{-7}	1.5×10^{-8}	10^{-10}	1.5×10^{-9}	3.3×10^{-7}	4.3×10^{-7}	8.6×10^{-6}	2.5×10^{-5}
10^{-8}	5×10^{-3}	2000	3.3×10^{-7}	1.5×10^{-6}	----	----	3.3×10^{-7}	4.3×10^{-7}	8.6×10^{-5}	2.5×10^{-5}

Optical Power W	Detector Output V	Amplifier Gain G_1	(Worst Case) HgCdTe $v/\sqrt{Hz}$	Amplifier A_1 $v/\sqrt{Hz}$	Amplifier A_2 $v/\sqrt{Hz}$	Amplifier A_3 $v/\sqrt{Hz}$	e_{total} $v/\sqrt{Hz}$	Noise Voltage v	Fractional Noise Components	Fractional Thermal Drift G_1S = 10V (1°C change)
10^{-6}	10^{-3}	10^{4}	3.25×10^{-8}	1.5×10^{-8}	----	----	1.25×10^{-8}	2.6×10^{-9}	2.6×10^{-6}	2.5×10^{-5}
10^{-7}	10^{-4}	10^{5}	1.25×10^{-8}	1.5×10^{-8}	----	----	1.25×10^{-8}	2.6×10^{-9}	2.6×10^{-5}	2.5×10^{-5}

3.2 Estimation of the Detection Limit

The signal to noise calculation has been carried out based on the difference signal given as

$$\Delta S = \eta_c A \Omega \left(\varepsilon \bar{B}_e - \bar{B}_a \right) \left(\overline{T_a T_c} - \bar{T}_a \bar{T}_c \right) \Delta \nu \qquad (3\text{-}4)$$

The radiance term is estimated by use of the blackbody radiance for a Lambertian surface as[2]

$$B = \frac{2hc^2}{\lambda^5} \left(e^{h\nu/kT} - 1 \right)^{-1} \qquad (3\text{-}5)$$

The temperatures of the ground and the air are taken as 300°K and 299°K respectively and the average emissivity over various terrain conditions is obtained from the literature[3]. The detectivity quotations for PbS (3.4 μ) and HgCdTe (7.8 - 11.8 μ) are referred to SBRC data.

The correlation coefficient is assumed to be linear in cl, which is justified by the results of the model calculation, thus the difference signal is written as

$$\Delta S = \eta_c A \Omega \left(\varepsilon \bar{B}_e - \bar{B}_a \right) \Delta \nu \cdot \rho (= \bar{\alpha} c \ell k) \qquad (3\text{-}6)$$

where ρ is the correlation coefficient for the gas leak.

The parameter k is then determined by setting the correlation coefficient obtained from the model calculation, to be equal to $\bar{\alpha}$ cl.k. Optimum cell parameters are used here.

Since the detector noise is the limiting noise of the system, the minimum (cl) value is obtained by setting the difference signal in equation (3-6) to be equal to the detector noise equivalent power,

$$NEP = \eta_c A \Omega \left(\varepsilon \bar{B}_e - \bar{B}_a \right) \Delta \nu \cdot k \bar{\alpha} \left(c \cdot \ell \right)_{min} \qquad (3\text{-}7)$$

Table 2 includes the parameters used in these calculations and summarizes the results.

PARAMETERS \ BAND	No. 1	No. 2	No. 3	UNIT
Gas	CH_4 C_2H_6	CH_4	C_2H_6	
λ	3.4	7.8	12.2	μm
$\Delta\lambda$	.25	.40	.40	μm
α (Absorption Coefficient)	.60 for CH_4 .73 for C_2H_6	.10	.80	$cm^{-1}\ atm^{-1}$
B_a	0.2	8.9	9.1	$10^{-4} w/(cm^2 \cdot \mu m \cdot Sr)$
$\bar{\epsilon}$	0.85	0.95	0.95	-
$\frac{\bar{B}_e - \bar{B}_a}{B_a}$ $(=N_s/\bar{B}_a)$	0.15	0.04	0.03	-
Etendu †	7.4	7.4	7.4	$10^{-2} cm^2 Sr$
T_w (Lens Transmission)	.98	.98	.98	-
T_f (Filter Transmission)	0.30	0.30	0.30	-
T_t $(=T_e^3 T_f)$	0.27	0.27	0.27	-
P $(=N_s A\Omega T_t \Delta\lambda)$	0.15	2.8	1.5	$10^{-7} w$
Detector	PbS	HgCdTe	HgCdTe	-
D* (low / high)	150 200	6.5 30	8.5 30	$10^9 cm\sqrt{Hz}/w$
Δf	1.7	1.7	1.7	Hz
Duty Factor	0.70	.70	.70	-
NEP†† (low / high)	0.32 0.25	7.7 1.7	6.0 1.7	$10^{-11} w$
NEP/P (low / high)	2.1 1.7	2.8 0.6	4.0 1.1	10^{-4} 10^{-4}
ρ†††/(10 ppm.M CH_4)	3.3	0.55	-	10^{-4}
k* ρ/(10 ppm.M C_2H_6)	0.55 4.0	0.55	4.4	10^{-4}
Detection Limit for CH_4 (low / high)	6.5 5.2	50 11	- -	ppm.M
Detection Limit for C_2H_6 (low / high) ††††	5.3 4.3	-	9.1 2.5	- -
Δ S/S for Detection Limit	4.3	1.1	1.3	10^{-5}
$\Delta\theta$** (Temperature Stability Limit)	.23	.83		K

TABLE 2

† Estimation is based on 110° detector field of view angle and $\pi \times 0.01\ cm^2$ detector area. Data confirmed with SBRC.

†† The band width was assumed to be 1.7 Hz, and the change in D* due to the increase in the field of view angle considered as D* (110°) = 0.67 x D* (60°). 70% duty factor is also assumed.

††† ρ is obtained from the results of the model calculation.

†††† The correlation coefficients for C_2H_6 are scaled by the ratio of the average absorption coefficient, assuming that the correlation efficiency of ethane is the same as that of methane.

* In view of the fact that the cell length used in the 7.8 μ estimation is not the optimum value and yet the same correlation efficiency is obtained as the 3.4 μ case, which has an optimum cell length, one can conclude that the spectral feature at 7.8 μ is more efficient for use in the GFC technique. The distinctive feature of the spectrum at the 7.8 μ band is that the band is composed of almost regularly spaced lines, while the 3.4 μ band consists of a series of subbands each of which contains several lines.

□ Without knowing the specific details of the ethane spectrum we assume that the correlation efficiency for the ethane spectra at both bands is as good as that for the methane spectrum at 3.4 μ. We have then estimated the correlation coefficient of ethane using a 1 cm x 760 torr gas cell.

** The temperature stability limit is obtained by using the temperature gradient of gas cell transmittance given in Chapter 2 and setting the relative change in the transmittance equivalent to the detection limit.

In principle, the sensor can achieve the detection limit listed on Table 2. However, the estimated thermal drift noise is approximately 2 larger than the $\Delta S/S$ ratio thus in practice the thermal drift noise will be the limiting factor. Efforts will be made to improve the thermal drift noise in order to improve the sensor sensitivity.

The sensitivity of the sensor in the winter months will be decreased due to the decrease in the correlation coefficient (Chapter 2) and the radiation power. The ratio of the source (ground) radiation power for 300 K and 253 K is estimated for each spectral band and listed in the following table.

$\lambda(\mu)$	3.4	7.8	12.2
$\frac{P\ (253\ K)}{P\ (300\ K)}$	7.6×10^{-2}	0.32	0.49
Scaling Factor	4.6×10^{-2}	0.19	0.29

The detection limit listed in Table 2 should be scaled down by a scaling factor which is determined by the product of a factor for the radiation power and the factor 0.6 for the correlation coefficient. The scaling factors for each band are also given in the above table. One may notice a significant change in the instrument sensitivity for the temperature change. The sensitivity at 3.4 μ is most seriously deteriorated by the temperature decrease and this phenomenon is well reflected in the signal processing concept (Chapter 5).

4. OPTICS

4.1 Introduction

The instrument uses the thermal radiation of the ground as an infrared radiance source. Due to the nature of the blackbody radiation, the source spectrum is broad and sensitive to the variation of the surface condition (emissivity) and the surface temperature. Furthermore, the small temperature difference between the ground and the atmosphere introduces additional difficulties associated with the thermal noise radiation from the atmosphere itself and the optical components of the sensor. In designing the optics, the following objectives have been defined:

i) Good rejection of the spectrum of the blackbody radiation outside the spectral band of the target gas.
ii) Minimize the modulated thermal radiation noise.
iii) Maximize the signal power.
iv) Minimize any systematic correlations between the ground structure and optical components.

4.2 Optical Components & Critical Areas

The optics are composed of a set of lenses, an interference filter, gas cells mounted on a chopper wheel, a detector and a shroud which covers the optics.

4.2.1 Lenses

The lens material will be highly transparent throughout the near and mid-infrared region (3 - 12 μ). A low absorption coefficient material is essential. Either Germanium lenses or Irtran lenses may be used, both materials show a very low absorption coefficient for temperatures below room temperature. The high reflection coefficient due to the high index of refraction can be easily minimized using anti-reflection coatings. Better than 98% transmission with the anti-reflection coating is quoted by

manufacturers for Ge lenses. Germanium lenses are chosen for two reasons. Firstly, since the index of refraction varies less than 1% over the spectral range of interest, the optical design for one band can be used for other bands without modification. Secondly, the high index of refraction of Ge with a proper choice of meniscus lenses minimizes the blur spot size caused by spherical aberration. This simplifies the design of the field stop significantly.

The lens diameter and thickness is minimized to reduce size and cost.

4.2.2 Systematic Correlation of the Terrain Structure with Optical Components

Since the terrain structure is changing in time, any systematic correlation of it with an optical component could appear as a difference signal. This correlation can be avoided by having the image of the ground removed from any optical components. However, since the pure spatial information is actually transformed to angular information at places other than the image plane, one can never be totally free of problems unless considerable design care is taken.

As an example, we have estimated the worse case of the correlation between the ground structure and the correlation gas cell which is set at the pseudo collimating region. Let us assume the rays from the two extreme positions of the footprint make 0.34 rad (20°), and the cell transmission coefficient is given as $T(\theta) = T_o \cos\theta$. The signal corresponding to the correlation of the radiance of the ground N_g and the gas cell is given as

$$\rho_s = T_o \left[\int_{\Delta\theta} N_g(\theta) \cos\theta \, d\theta - \frac{1}{\Delta\theta} \int_{\Delta\theta} N_g(\theta) d\theta \int_{\Delta\theta} \cos\theta \, d\theta \right] \qquad (4\text{-}1)$$

For a radiance function $N_g(\theta) = N_o \cos\theta$ which is the worse case,

$$\rho_s = T_o N_o \left[\int_{-0.17}^{0.17} \cos^2\theta \, d\theta - \frac{1}{0.34} \left(\int_{-0.17}^{0.17} \cos\theta \, d\theta \right)^2 \right] \qquad (4\text{-}2)$$

$$= T_o N_o \times 6.2 \times 10^{-4}$$

On the other hand, for constant source radiance $N_g(\theta) = N_o$,

$$\rho_s = T_o N_o \left[\int_{\Delta\theta} \cos\theta \, d\theta - \frac{1}{\Delta\theta} \int_{\Delta\theta} \cos\theta \, d\theta \int_{\Delta\theta} d\theta \right] \equiv 0 \qquad (4\text{-}3)$$

Considering that the correlation coefficient of the estimated gas leak is the order of 5×10^{-4} and the relevant radiation term for the gas signal is about 10% of N_o, the gas leak signal is well above the possible noise signal due to the correlation between the terrain structure and the gas cell.

4.2.3 Interference Filter

The function of the interference filter is to reject the broad source spectrum outside the target gas bandpass. Using an interference filter with high rejection rate and a transmission well matched to the gas passband maximizes the sensitivity and specificity of the instrument. A suitable multi-layer interference filter is commercially available. The rejection rate to the longer wavelength normally does not extend beyond 15 μ from the transmission band, however the sharp drop in the detector spectral responsivity blinds out the long wavelength side of the blackbody spectrum. Thus the interference filter rejection rate extends, effectively, to the far infrared.

Since the radiation source is not a point source, wherever the interference filter is located it will intercept rays of various incident angles. The peak transmission wavelength of the filter shifts towards the shorter wavelength as the angle of incidence increases. An estimated shift, $\Delta\lambda$, for an interference filter, with peak transmission at $\lambda = 12.2$ μ, for the normal incident ray, is plotted in Figure 18 as a function of the angle of incidence. The effective index of refraction, $n_e = 2.23$, is quoted from a manufacturer's (Valtec) specification. The shift, effectively, broadens the transmission bandwidth of the interference filter for an extended source, and thus should be minimized, in order to maximize the correlation signal. The bandwidth of the interference filter will be selected considering this shift.

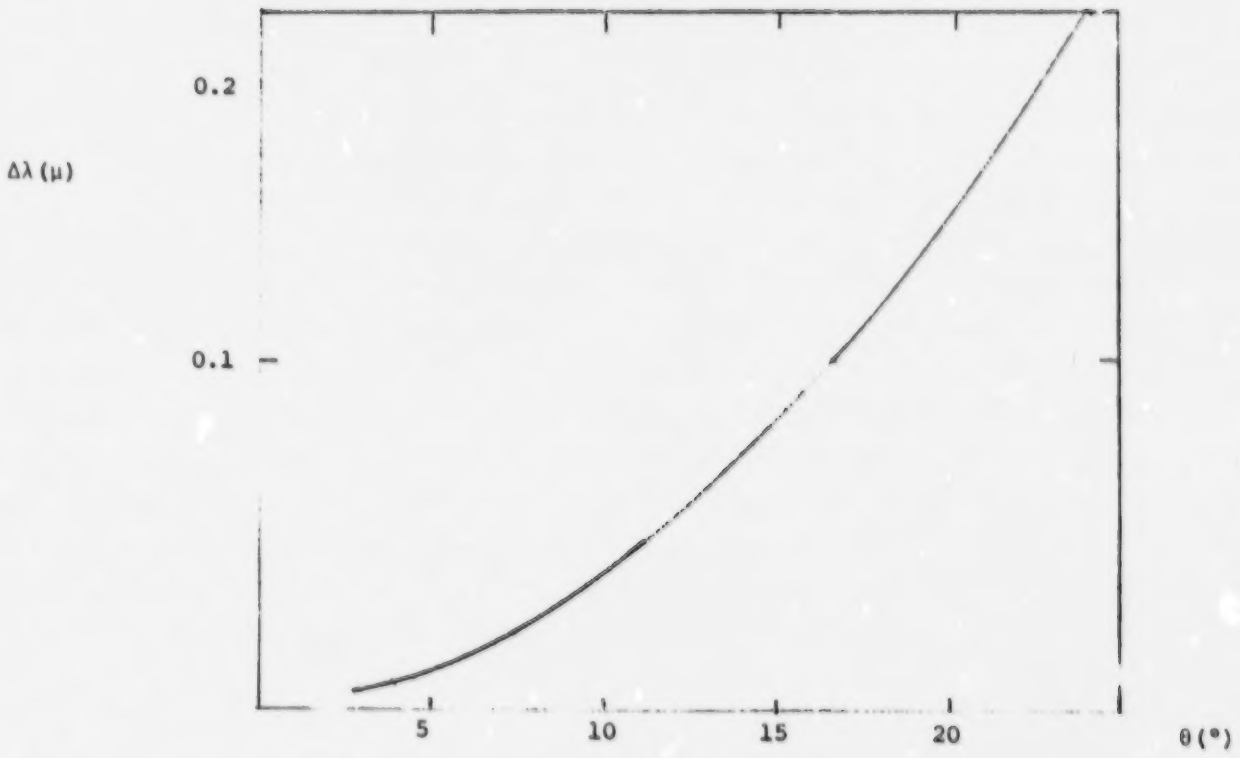

FIGURE 18: Peak transmission shift due to the incidence angle at $\lambda = 12.2\mu$ for $n_e = 2.23$

For the specific requirement of taking two gas signals at two different bands, a possibility of attaching the interference filter sets at the rear side of the chopper wheel has been investigated and the detailed estimation of the signal fluctuation due to the non-uniformity of the filter has been carried out as follows:

i) Fluctuation of the Source Radiance Signal

The manufacturer's specification on the spatial filter transmission non-uniformity is 1%. Thus for the 2×10^{-4} parts of the time jitter of the chopper speed, the signal fluctuation is estimated to be $\delta S = 0.01 \times 2 \times 10^{-4} \times N_o = 2 \times 10^{-6} N_o$. On the other hand, the minimum leak gas signal is estimated to be $\Delta S = (\varepsilon \bar{B}_e - \bar{B}_a) A T_o \rho \approx 3 \times 10^{-5} N_o$. Thus the effect of the non-uniformity of the filter transmission on the signal is not significant.

ii) Fluctuation of the Thermal Radiation Noise

A modulated component of the thermal radiation noise can originate due to the non-uniformity of the filter transmission. Assuming 0.01 emissivity and 100 cm^2 of emitting area of the blackbody radiation, the total thermal noise power is estimated according to the Stefan-Boltzmann formula as

$$P_n = \frac{\varepsilon \sigma T^4 A}{2} = 1.6 \times 10^{-2} \text{ Watt} \qquad (4\text{-}4)$$

Considering a factor 10^{-1} decrease of the noise power due to the detector responsivity, since the detector is responding to only a small portion of the total energy, a factor 10^{-2} decrease by using the interference filter and a factor 10^{-3} decrease for the collection efficiency onto the detector, the radiation power decreases to $P_n' = 10^{-5} \times 1.6 \times 10^{-3} = 1.6 \times 10^{-8}$ watt.

For 1% variation of transmission and 10^{-4} parts jitter in the chopper position the modulated thermal radiation noise which pases through the filter is estimated to be $\delta P_n' = 10^{-6} \times 1.6 \times 10^{-8} = 1.6 \times 10^{-14}$ watt. On the other hand the modulated thermal radiation noise

originating from the reflection off the interference filter is estimated to be $\delta P_n' = 1.6 \times 10^{-12}$ watt by simply removing the filter transmission term of 10^{-2} from $\delta P_n'$. Comparing these numbers with the detector NEP $\simeq 10^{-11}$ watt, one concludes that the thermal noise radiation is not the limiting noise factor. The assumed value of $\varepsilon = 0.01$ in the estimation of $\delta P_n'$ is a conservative value even if there is a black shroud between the chopper and the detectors, as the rays reflected off the filter will be absorbed by the black surface of the shroud.

iii) Variation in the Spectral Transmission Curve

Since interference filters for the gas cell and the reference cell cannot be made exactly the same, the spectral transmission curves between any pair of filters cannot be identical. The peak transmission wavelength can also shift. If we have no spectral structure in the source spectrum, i.e., $N(\lambda) = N_o$, the variation of the spectral transmission curve would not affect the difference signal at all. However, we do expect a fair amount of spectral structure in the received (through the atmosphere) radiation. A correct estimation of this effect due to the mis-match of a pair of interference filter transmission curves on the ΔS signal is subject to the given pair of transmission curves and the given source spectrum.

4.2.4 Thermal Radiation Noise

The optical components (lenses, interference filters, gas cells) must have a very low absorption coefficient not only for high transmission but also for low thermal radiation power. It should be pointed out that only the radiation being modulated by the chopper will be synchronously detected at the electronic signal output. Germanium has very low absorption coefficient below room temperature and is readily available commercially. The major portion of the thermal radiation is from the mechanical shroud components, i.e., the chopper wheel and lenses. The contribution from the chopper wheel can be ignored because the modulation occurs in such a way that the signal switch is on only when the gas cell (on the chopper wheel) comes into view.

Also the contribution from the lenses is estimated to be minimal and in any case is spectrally flat and constant so as not to appear at the sensor output. One can approximate the optical train as a cylindrical thermal radiation source where the cylinder is assumed to have a 2 cm radius and a 10 cm length in front of the chopper wheel (Part A) and a 10 cm length at the back of the chopper (Part B) as shown below.

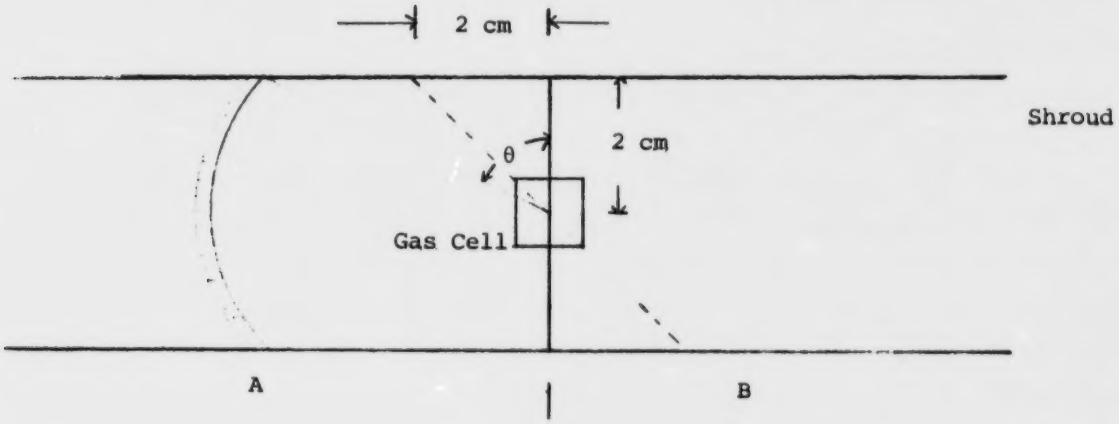

In this calculation we assume a highly reflective surface for Part A and a highly absorptive surface for Part B. The low ε for Part A minimizes the total thermal radiation power from Part A and the high ε for Part B absorbs the modulated thermal radiation through the chopper when the ray hits the surface of Part B. This way we can minimize the modulated thermal radiation power. The time invariant contribution is filtered out by the synchronous detector.

The geometry of the correlation cell confines the acceptance angle to be very narrow, and effectively reduces the thermal radiation power considerably. An estimation of the received power is carried out below using the above mentioned geometry.

Assuming a Lambertian source, the radiation power from dA and through the cell is written as

$$dP_r = N_0 \, dA \, \Omega \cos\theta \tag{4-5}$$

Here N_0 is radiance, Ω is the solid angle subtended by the cell and represented by

$$\Omega \cong \frac{1}{2} \frac{1}{(z^2+4)} \tag{4-6}$$

and dA is the differential area of the source, i.e.,

$$dA = 4\pi \, dz \tag{4-7}$$

Thus the total radiation power into the cell can be integrated as

$$\delta P_r = \int N_0 \, \Omega \cos\theta \, dA \tag{4-8}$$

Substituting equation (4-6) and (4-7) into equation (4-8) one obtains

$$\delta P_r = 4\pi N_0 \int_{z=2}^{10} \frac{dz}{(z^2+4)^{3/2}} = \pi N_0 \left[\frac{z}{(z^2+4)^{1/2}} \right]_2^{10} \tag{4-9}$$

$$\cong 0.27 \cdot \pi \cdot N_0$$

On the other hand the total radiation is estimated to be

$$P_r = \frac{1}{2} N_0 \times \Omega A \tag{4-10}$$

Thus

$$\frac{\delta P_r}{P_r} = \frac{N_0 \times 0.27}{N_0 \times 126} \simeq 2 \times 10^{-3} \tag{4-11}$$

The high ε value for Part B of the shroud effectively reduces any modulated radiation to nil following a reflection. As a result the modulated radiation can be considered as emitted from the cell located 10 cm away from the detector. The collection efficiency for the direct ray from the cell is estimated by considering the solid angle subtended by the detector which is $d\Omega = 3.1 \times 10^{-4}$ Sr.

Thus the collection efficiency can be written as

$$\eta = \frac{d\Omega}{\Delta\Omega} = 6 \times 10^{-4} \qquad (4\text{-}12)$$

where $\Delta\Omega$ is the acceptance solid angle of the gas cell, ~ 0.5 Sr.

In conclusion, we estimate the modulated radiation power from Part A to be $P_m^o A = 1.6 \times 10^{-2} \times 2 \times 10^{-3} \times 3.1 \times 10^{-4} = 1.0 \times 10^{-7}$ watt. With the interference filter, we expect 10^{-3} decrease in power (Refer to Figure 1), thus $P_m^o A = 1.0 \times 10^{-10}$ watt. For a temperature fluctuation of 0.1° /sec, the fractional variation in the radiation power is $\sim 10^{-2}$ thus the equivalent radiation power fluctuation is $P_m^o A = 1.0 \times 10^{-12}$ watt which is well below the detector NEP level.

This is a conservative estimation, because we did not consider the electronic high-pass filter rejection rate which is 20 dB/decade. Because of thermal inertia the temperature cannot fluctuate quickly and any fluctuating signal corresponding to temperature changes will be effectively filtered out by the synchronous detector. Even for the high ε value, the effective radiation power after the filter rejection rate becomes

$$\delta P_B = P_B \cdot \eta_{if} \cdot \eta_{ef} \cdot \eta_r = 1.6 \times 10^{3} \times 10^{-8} \times 10^{-2} = 1.6 \times 10^{-13} W \qquad (4\text{-}13)$$

where η_{if}, η_{ef}, and η_r represent the interference filter rejection rate, the electronic filter rejection rate and the average collection efficiency of the detector, respectively.

In summary, we can easily suppress the effects of the thermal radiation noise well below the detector NEP value.

4.2.5 The Chopper Wheel

The chopper wheel contains both the CH_4 and the C_2H_6 gas cells as well as the reference cells. The chopper wheel will be of high emissivity in order to provide a representative indication of the gas cell temperature. The gas cells will be mounted on the concentric annular regions for an identical double beam configuration as shown in Figure 19. The timing marks are also incorporated on the chopper.

The cells will be constructed by attaching ZnSe windows on both ends of the glass pipe which has annular cross sections. The parallelism of the windows can be established better than 10^{-3} radian, which means that the gas transmission is uniform with an accuracy of 0.1% over the entire cross section of a given cell. The cell will be filled with the optimum pressure using MONITEQ's gas handling facilities and sandwiched between mechanical mounting plates.

The syncrhonous detector relies on having a reference and signal which are correctly phased. Since these two signals are derived from different parts of the chopper wheel, any variation in the position of the reference detector will result in phase error. Similarly, variation in the chopper speed between encoder marks or errors in encoder manufacture will cause phase errors.

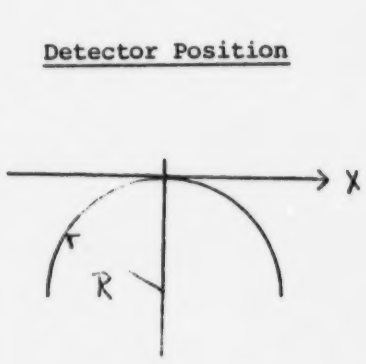

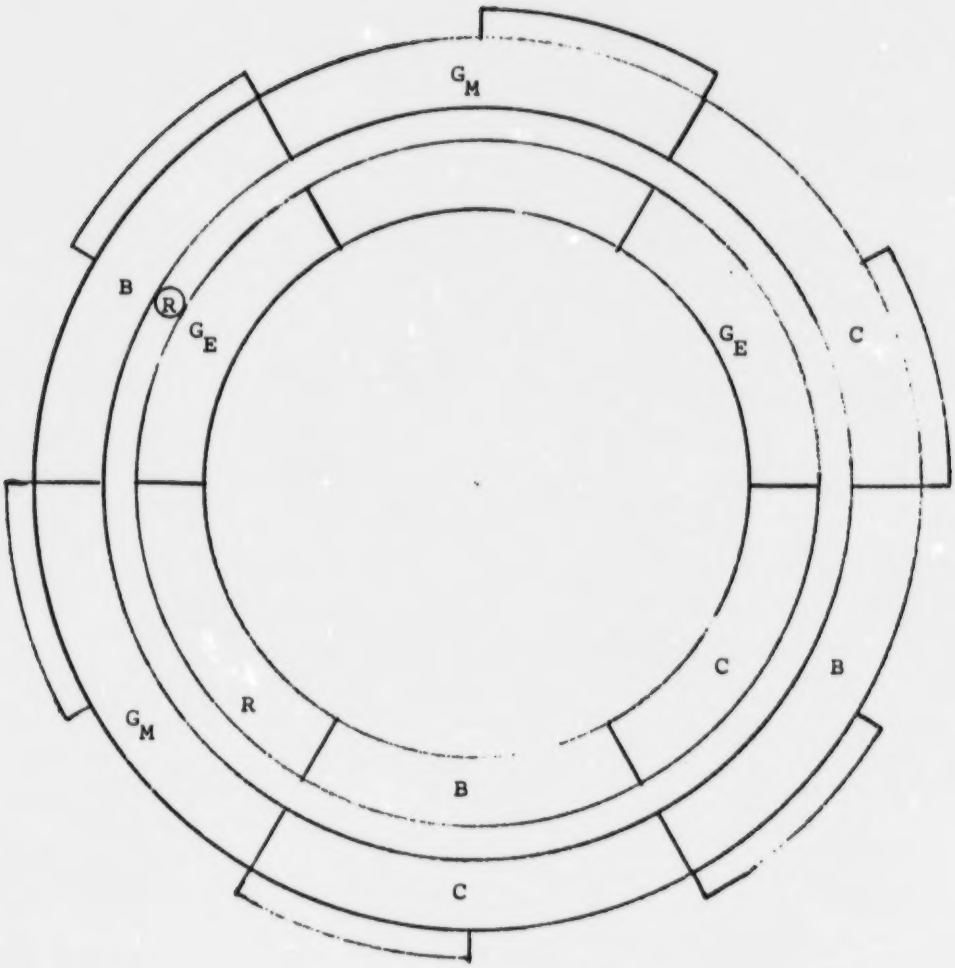

FIGURE 19: Chopper wheel configuration

G_M = methane gas cell

G_E = ethane gas cell

C = clean cell

B = blank

R = reset

A lateral shift, x, of the detector on a circle of radius R results in a phase error of $\frac{x}{R}$. This lateral shift can occur as a result of vibration or a fluctuation in the set point of the edge trigger. For a square pulse of angular duration θ, the jitter is $\frac{x}{R\theta}$. To measure signals to 1 part in 10^5 requires $\frac{x}{R\theta} \leq 10^{-5}$. Our experience indicates that the jitter is approximately 2 μs, for a pulse of duration .01 s. Therefore jitter would normally limit signal capture to 2×10^{-4}.

MONITEQ has conceived of a method whereby improvements are possible, using a master oscillator and precision gating, operating on an in line switch to achieve $< 2 \times 10^{-6}$. This number is estimated on the basis of switch jitter of 20 ns in the same .01 sec. That is, the mechanical jitter is eliminated.

4.2.6 Detector

The detector field of view will be selected to be 100° full angle to increase the etendue of the instrument. The D* will be affected by having this large field of view angle. However, the gain in the final signal capture as the etendue is increased is approximately a quadratic function of the view angle and the D* decreases very slowly as a function of the field of view angle as shown in Figure 20.

The detector sensitivity varies considerably over the active area of the detector. An example of the sensitivity contour of a PbSe detector is shown in Figure 21.

HgCdTe detectors are more spatially uniform in responsivity, however, in order to avoid any systematic correlation of the detector sensitivity contour with any other moving part of the optics, the objective lens is focused on to the detector.

Since the size of the detector is only 1 mm radius and the beam spot is about the same size, care will be taken with optical alignment, stability, and thermal stress on the optical train.

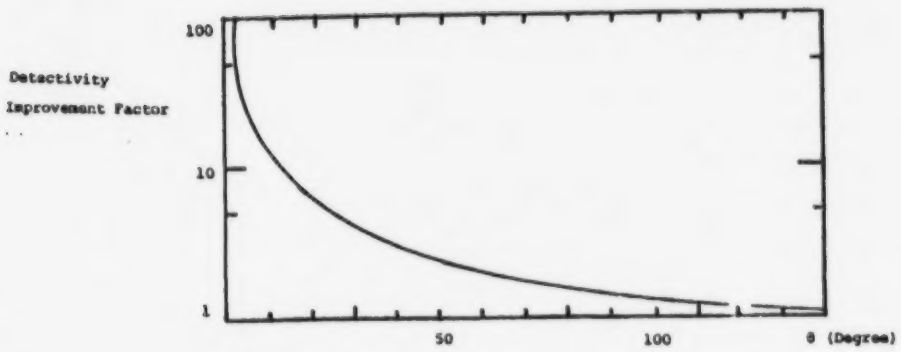

FIGURE 20: Dependence of detectivity improvement on detector field of view

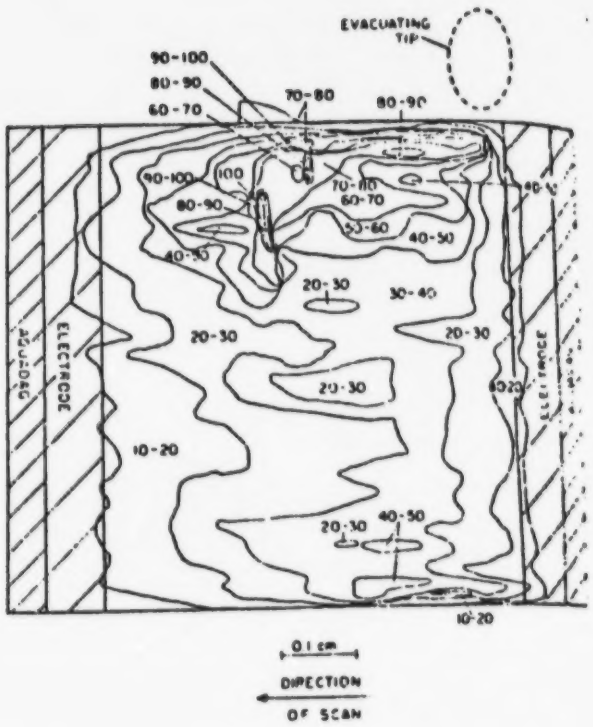

FIGURE 21: Spatial variation of a PbSe detector

4.3 Optical Configuration

Three possible optical configurations were considered which meet the noise figures discussed in the previous section. The schematics of these configurations are shown in Figure 23. Configuration (1) differs from others in terms of the filter location and time sharing of the detector for both CH_4 and C_2H_6 gases. A set of filters are located at the back of the chopper for each gas and the reference gas cells. Although this configuration appears to be cost effective, in practice it is very expensive to obtain well matched filters. In addition the filter cannot be tilted to any degree without disturbing the chopper wheel balance, and the filter for the reference and gas cells must be very carefully matched.

Configuration (2) shares the front end optics, but employs two detectors, one for each gas. The interference filter is placed in front of each detector. A beam splitter is located in the pseudo collimated region. This configuration does not have problems associated with the interference filters which are discussed in the previous paragraph. However, the duty factor is smaller than that of the configuration (1) by a factor of 2, and there may well be problems of polarization at the beamsplitter.

Configuration (3) is a dual channel configuration sharing one chopper wheel. The chopper wheel configuration is shown in Figure 19. The upper channel views the outer portion of the chopper wheel and the bottom channel views the inner portion of the chopper. This configuration is also free of the problems associated with the interference filters, and the interference filter can be tilted. The duty factor is increased by a factor of 4 over that of the configuration (2) and by a factor of 2 over that of the configuration (1), and there are no polarization problems. Finally the spectral filter does not move, and is identical for both gas and reference cells.

In conclusion, configuration (3) appears to be the best choice of all. It has the highest duty factor, is free of any problems associated with the interference filter, is cost effective and straight forward.

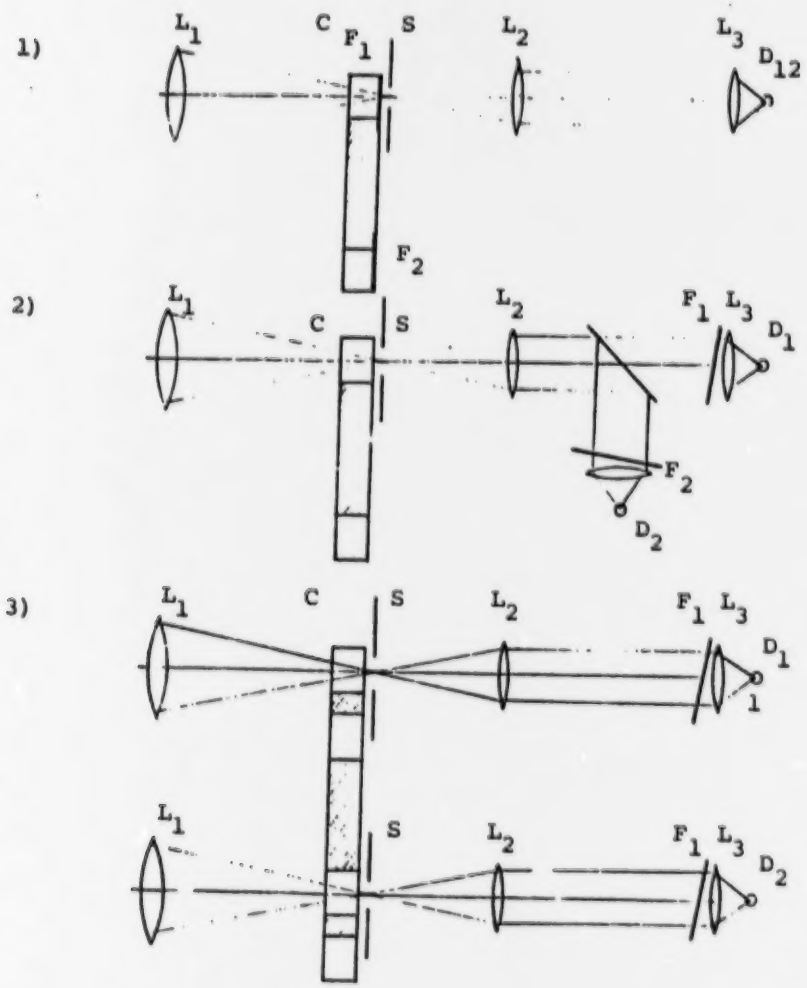

FIGURE 23: Schematics of optical configurations

L_1, L_2, L_3 = lenses

C = chopper

S = field stop

F = interference filter

D = detector

5. SIGNAL PROCESSING

5.1 Introduction

The difference signal, ΔS, in the correlation technique is the product of the radiation term and the correlation coefficient. These two terms are independent of one another. The radiation term depends on the kinetic temperature of the ground and atmosphere and on the ground emissivity. On the other hand the correlation coefficient is governed by the target gas spectrum and the total burden (the concentration times the thickness of the layer). The kinetic temperature of the gas does not influence the correlation coefficient significantly for temperature variations expected in the field.

The indication of the gas leak is included in the correlation coefficient, and is completely independent of the radiation term, except for a scale factor.

Variations in the radiation term when a fixed amount of background gas is present will appear as a difference signal, and be indistinguishable from the leak gas signal. The data must be processed to be free of this radiation term. In addition the signal processing must take place in such a way as to avoid misinterpretation of ground motion across the field of view as a leak gas signal.

5.2 Selection of the Spectral Bands

There are two bands available for each gas; one at 3.4 μ, the other at 7.8 μ for CH_4 and one at 3.4 μ the other at 12.2 μ for C_2H_6. From the signal to noise calculation discussed in Chapter 2, there are no strongly preferred bands. However, the solar radiation effect at 3.4 μ makes it very difficult to apply any simple signal processing routine for CH_4 gas at this spectral location. Also, the absence of the residual C_2H_6 gas, the abundance of the CH_4 residual gas and the higher amount of CH_4 in the leak

gas make the problem on hand more complicated. As discussed in Chapter 1, the term associated with the residual CH_4 gas is about 1,000 times larger than the expected leak gas signal.

Considering this, the 7.8 μ band for CH_4 appears to be the only band worthy of effort. The solar radiation effect at this wavelength is negligible, and the signal to detector noise figure is ∿ 0.3 as good as that of the band at 3.4 μ.

Since the residual C_2H_6 gas in the atmosphere is only a few ppb, the band at 3.4 μ appears as valid as the one at 12.2 μ.

As discussed in Chapter 1, the radiation term may fluctuate considerably less at 7.8 μ and 12.2 μ than at 3.4 μ due to the relatively more constant surface emissivity at these longer wavelengths. In the case of ethane, the emissivity of the ground at 3.4 μ is more variable than that at 12.2 μ. This makes it more difficult to work at the shorter wavelength band. In addition, the unknown cross correlation of CH_4 and C_2H_6 at 3.4 μ could be problematic. Nevertheless, insufficient evidence could be found to reject the 3.4 micron C_2H_6 measurement attempt.

In conclusion, the band at 7.8 μ for CH_4 and the band at 12.2 μ for C_2H_6 are the best choice.

5.3 Signal Processing Concept

The radiation term in the difference signal can be isolated if the ratio of signals for two uniformly mixed gases is performed.

For the best results, the absorption bands of both gases should be located at the same wavelength. In this case the effects associated with the emissivity variation and the air temperature fluctuation can be compensated. In this respect it might be best to work with the 3.4 μ bands for C_2H_6 and CH_4. However, the solar radiation effect on CH_4 at 3.4 μ has made this invalid.

The emissivities of the ground at 7.8 μ and 12.2 μ are similar for various terrain constituents. Thus, the ratio of the signals at these wavelengths can be formed to extract the correlation signal which is free of the radiation term. There is approximately 1.4 ppm of CH_4 and only a few ppb of C_2H_6 in the standard atmosphere. Therefore, the increase in the correlation coefficient for CH_4 gas by the leak gas is estimated to be only a few percent but the increase in the correlation coefficient for C_2H_6 gas will be very large. As a result, the ratio of the ethane signal to the methane signal will yield a very large signal change for the leaked gas.

The ratio of the ethane concentration to the methane concentration in the leak gas is expected to be approximately 3 to 100. Thus the ethane leak gas signal will be generally smaller than the methane leak gas signal.

The proposed design will take two signals simultaneously; one the difference signal for CH_4 gas and the other the ratio of the C_2H_6 gas signal to the CH_4 gas signal. The CH_4 gas signal will fluctuate due to both the leak gas concentration and the radiation term. The second signal will be used to assign which signal is due to the gas leak or the fluctuation in the radiation term.

6. ANALOG SIGNAL PROCESSING

6.1 General Discussion

The instrument uses two synchronized phase sensitive detectors to acquire data for both CH_4 and C_2H_6 gas channels simultaneously. The system is synchronized by having both optical paths share the same chopper disk and having the chopper disk govern the timing. Two signals are collected for each gas, the difference signal, ΔS, and the S_o signal which is related to the ground radiance. These four signals are collected, digitized and transferred to the microprocessor for further manipulation.

The analog signal processing is illustrated in Figure 24.

6.2 Phase Sensitive Detection

For each gas optical path, the filter wheel presents a fixed sequence of sectors as it rotates. The sequence of the sectors is B, G, C, B, C, G, where B is blank, C is clear, G is gas sample.

As each sector is presented, timing signals are picked off the filter wheel. The signals are decoded to switch the output from the preamplifiers associated with each sector into the appropriate sample and hold integration. For each gas the ΔS signal is the analog subtraction of the radiance signals by the order of G, C, B, C, G. This sequence compensates for short term linear variations in the radiation term.

The S_o signal is the difference between the irradiance signal through the reference cell and the radiance signal from the blank sector.

Since the field stop is very near to the chopper wheel, the S_o signal is approximately the difference between signals corresponding to the ground radiance and the blank sector radiance, i.e., $C_1N_e = S_o + C_2N_b$ where N_e and N_b represent blackbody radiances of the ground and blank sector

respectively and C_1 and C_2 are calibration constants to be determined by experiment. Therefore the electronic signal corresponding to the ground radiance C_1N_e can be constructed by measuring S_o signal and the chopper temperature.

The phase sensitive detector for one gas channel is illustrated below.

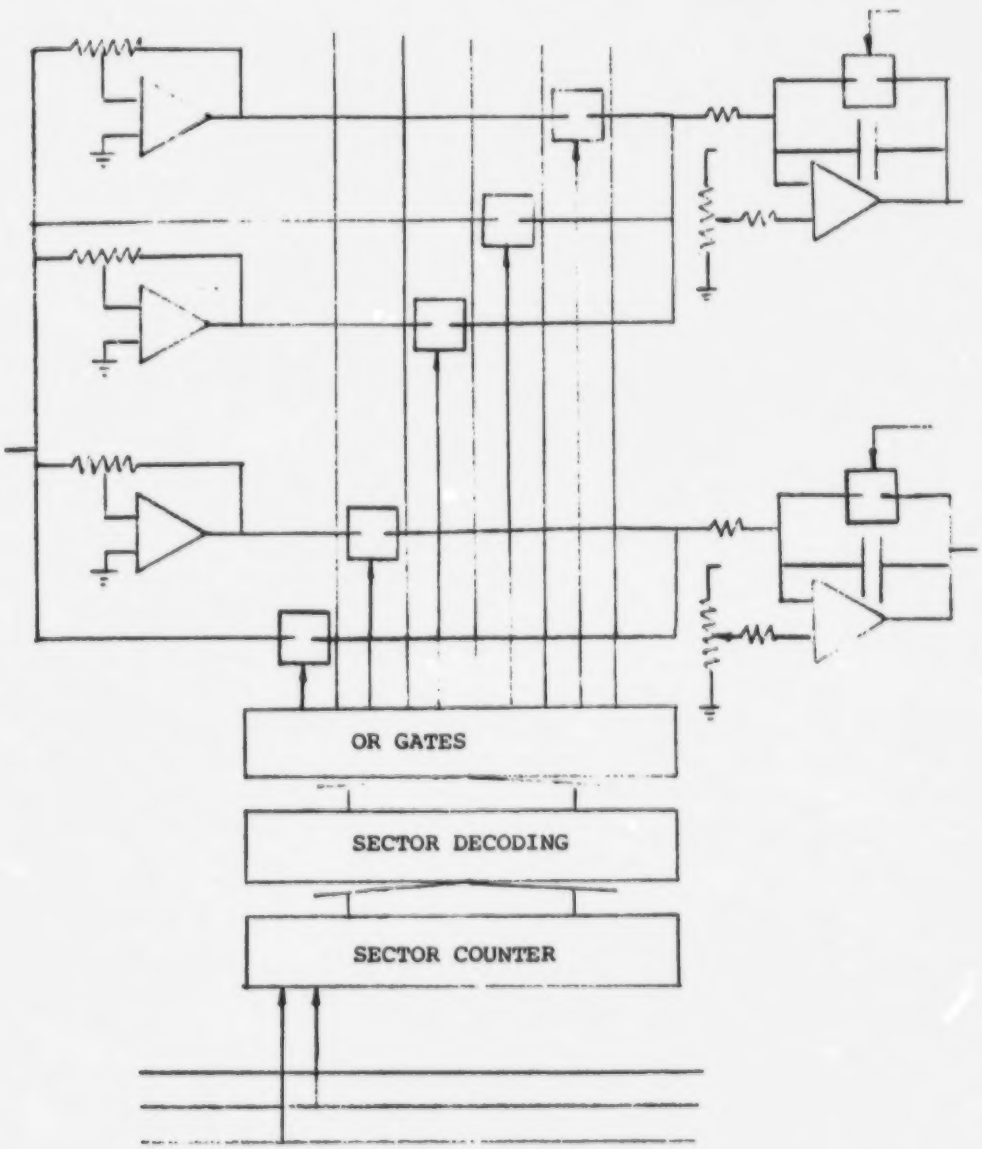

The top integrator collects the ΔS signal from output associated with G sectors and an inverted signal associated with R sectors. The lower integrator collects an S_o signal from C sector output and inverted B sector output.

To minimize the effect of mechanical jitter in the filter wheel and transition effects in chopping, a precision timing network is incorporated. A delay allows the transition between sectors to be completed and the phase sensitive switches to close. After the delay the precision switches are closed for a fixed gate time ensuring that the same integration time is used for each sector. Both delay and gate time are selectable. The precision gating is illustrated below.

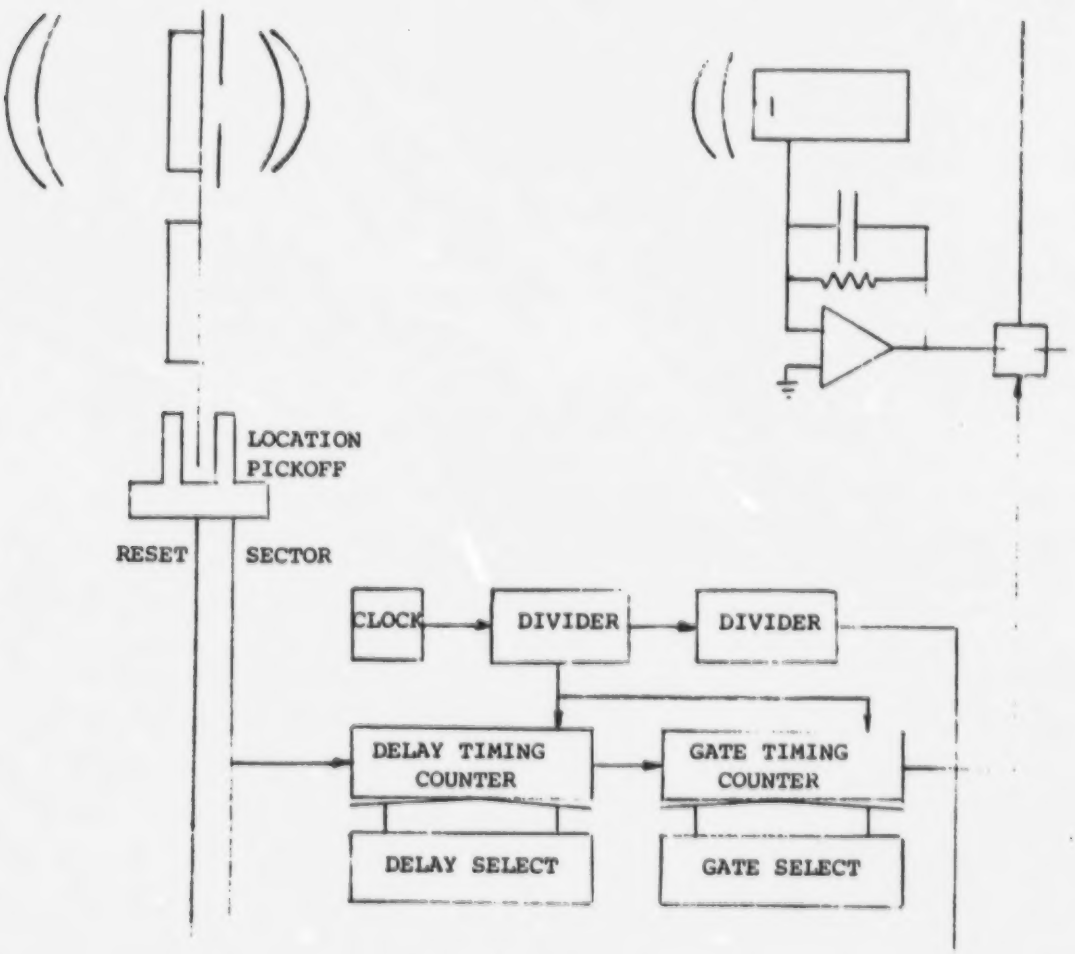

The filter wheel is designed so that the sequence for one optical path is two sectors out of phase with the other sequence. This allows sequential digital conversion and resetting of each integrator once per revolution. The synchronization procedure is governed by the filter wheel timing marks.

6.3 Analog to Digital

The outputs of the four integrators are switched sequentially into an analog to digital convertor by a multiplexor. The multiplexor input is selected by counting the filter wheel timing marks after a four sector delay from reset. A timing diagram is shown below.

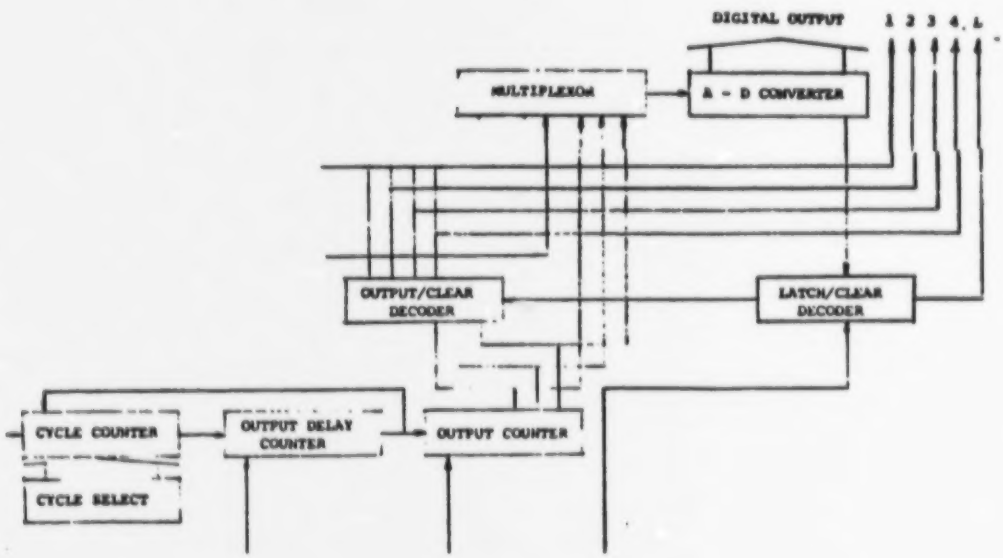

When the conversion is complete (CC) the output is latched and the integrator is cleared for the next cycle. At the same time one of four output flags is set and generates an interrupt in the microprocessor. The analog to digital section is also illustrated above.

The microprocessor is controlled by interrupts generated from the output flags for data acquisition and by interrupts generated from counting filter wheel revolutions for data reduction. When a data acquisition interrupt occurs the microprocessor is vectored to the appropriate data acquisition routine where the output is summed into an accumulator for that channel. After a software adjustable number of cycles the accumulated values are moved so that they can be reduced while the next data set is collected into cleared accumulators. The data reduction routine converts the integer values into floating point numbers, ratios the values and displays the results.

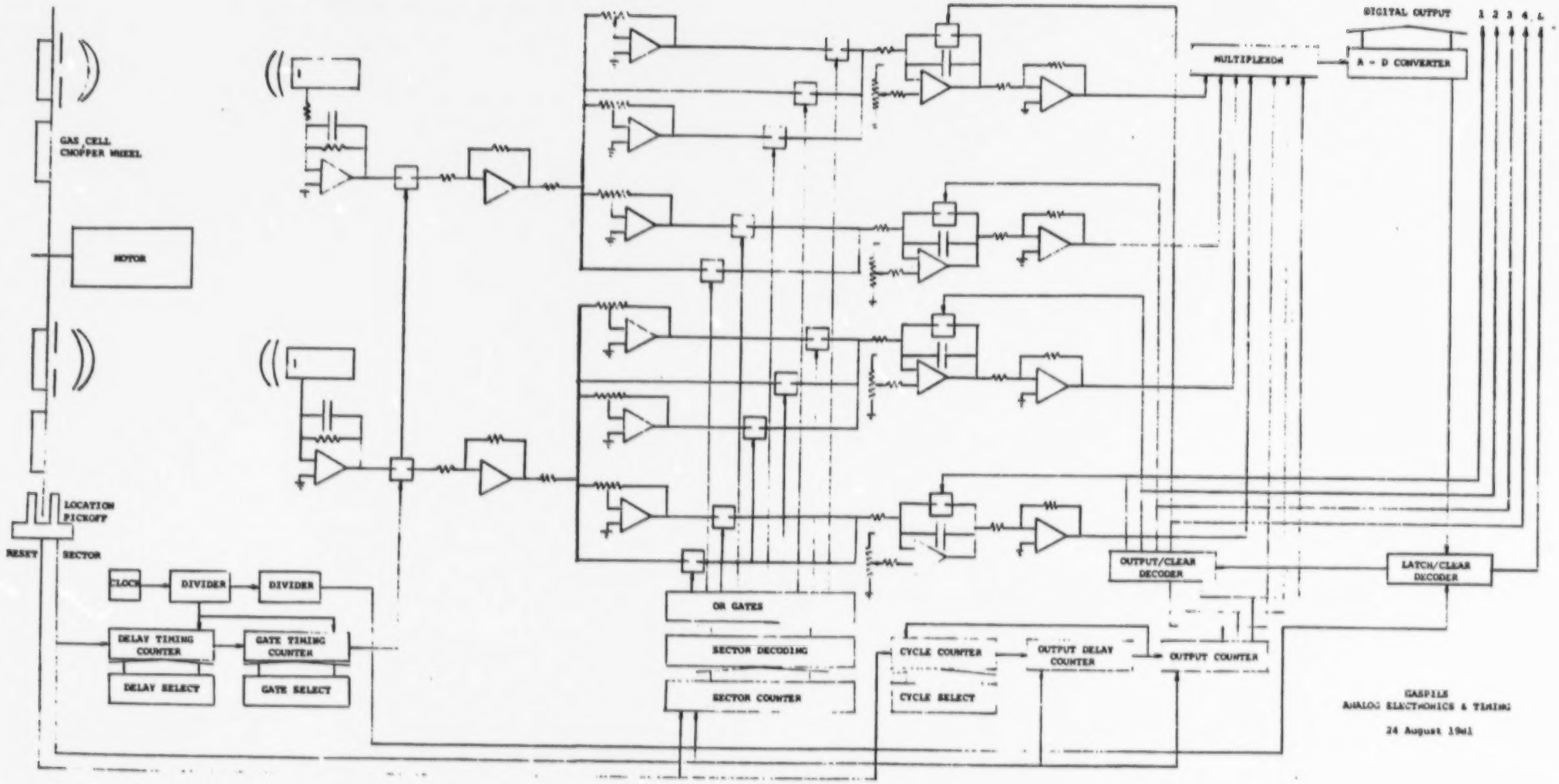

GASFILS
ANALOG ELECTRONICS & TIMING

24 August 1981

7. INSTRUMENT CALIBRATION AND TEST

7.1 Confirmation of the Optimum Cell Parameters

The optimum correlation cell optical depth is determined from the results of the model calculation. The cell length will be pre-determined by allowing the optics and chopper wheel configuration to be as large as possible. The correlation gas in the cell will be diluted to its correct partial pressure by dry nitrogen gas. Several gas cells with different pressures near the optimum value determined from the simulation, will be prepared to perform an experiment. The residual gas and the leak gas will be simulated by the equivalent amount of the gas in a cell in the laboratory. A blackbody source of 300 K will be located at the back of the test gas cell, and the sensitivity of the instrument will be tested in order to confirm the theoretical prediction. This calibration procedure is essential, especially for ethane gas, because there has been no model calculation for this gas due to the lack of experimental spectroscopic data. The initial trial value of the ethane pressure will be inferred from the value for the methane gas. The difference in the average absorption coefficient and the spectral structure will be considered in this estimation.

7.2 The Difference Signal Balancing

By locating a blackbody radiation source immediately in front of the objective lens, the instrument will be calibrated for zero difference signal. The balance will be done by adjusting the gain of the amplifier for the reference gas channel signal, G_2, until changing blackbody radiances gives zero output, and adjusting the gain of the amplifier for the blank sector signal, G_3 to k.

In the absence of the test gas, the difference signal is expressed as

$$\Delta S = S_g - G_2 S_r - G_3 S_b \qquad (7\text{-}1)$$

where the S's stand for the signal from the detector, and the subscripts g, r, and b represent correlation gas channel, reference gas channel and blank sector, respectively.

The correlation gas channel signal is composed of two parts; one corresponding to the transmitted radiation flux, the other the radiation emitted from the correlation gas.

Therefore, one can write

$$S_g = T_c S_r + S_e \tag{7-2}$$

where S_e represents the signal corresponding to the gas emission.

Substituting equation (7-2) into equation (7-1) one obtains

$$\Delta S = T_c S_r + S_e - G_2 S_r - G_3 S_b \tag{7-3}$$

The balance is carried out by adjusting the electronic gain factors G_2 and G_3 to ensure ΔS zero for any S_r and S_b values (changing source radiation). S_e is proportional to S_b under the assumption of thermal equilibrium between the chopper wheel and the correlation gas, thus, $S_e = (1 - T_c) S_b$.

S_r and S_b are independent of one another since the source temperature and the chopper wheel temperature are independent. Therefore, the balance for thermal changes can be established independently. Thus, $T_c S_r = G_2 S_r$ balance is adjusted to give zero output with external blackbody source temperature changes, and $G_3 S_b = S_e = (1 - T_c) S_b$ is established through balancing to a zero output for gas cell temperature changes.

Strictly speaking the transmittance through the gas cell is a function of the thermal temperature of the chopper wheel, however the effect of the temperature on transmittance is not significant and may be ignored.

The average gas cell transmission, T_c, is a strong function of the cell pressure (linear function for $T_c < 0.05$). As a result the balance to the instrument is made for a specific given cell pressure.

In order to obtain the two independent balances one can apply the following procedure:

i) Set G_2 near 1.

ii) Vary the external blackbody source temperature and adjust G_3 until no change in ΔS is observed.

iii) Fix G_3 and the external blackbody source temperature and vary G_2 until no change in ΔS is observed.

iv) Repeat steps (ii) and (iii) several times until no further adjustment is required from the previous values of G_2 and G_3.

After a careful balancing for the optimum cell pressure, G_2 and G_3 values will be tabulated in the instrument specifications as a reference.

7.3 Instrument Sensitivity Calibration

The instrument sensitivity calibration will be done for the optimum gas pressure and correct balancing. The leak gas on top of the residual gas will be simulated in the laboratory by using a test gas cell which has an equivalent (cl) value of the expected leak gas burden. Initially the sensitivities for methane gas and ethane/methane will be calibrated independently.

For a given test cell (cl) value, the source temperature will be varied and the validity of the signal processing concept will be tested. The source as well as the test gas temperature will be varied in this test.

7.4 Instrument Stability

Mechanical vibration and thermal stress are two major environmental factors to be considered in order to test the stability of the instrument. The mechanical vibration can shake the optical train and cause a deterioration of the optical transfer efficiency. To overcome this problem, the sensor design will include an optical train on which all the optical components, including the detectors, will be mounted kinematically. The last lens and detector will be mounted together so that the relative position of these two components remains the same through any vibration. A conceptual design is shown below.

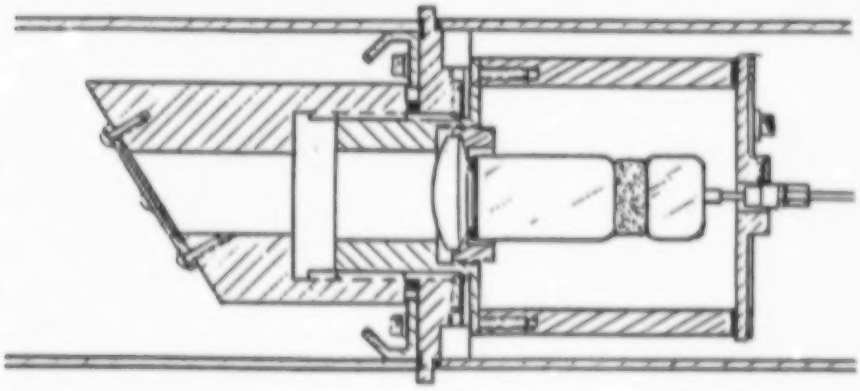

The chopper speed may be influenced by vibration. A speed controlled motor using an electronic high precision gating system will be employed to overcome this problem. As the sensor views downward the chopper disk will rotate about a vertical axis so that platform accelerations are expected to be small.

Thermal temperature variation and consequent thermal stress may also affect the optics. Symmetry and good design practice will be maintained as much as possible in the design of the optics to avoid this problem. The chopper disk housing will be thermally stabilized and controlled.

Electrical noise input will be minimized by mounting a low noise pre-amplifier as close as possible to the detector. The detector including the pre-amplifier will be shielded by a good conducting metal (or μ metal).

8. MECHANICAL DESIGN

The sensor will be housed in an aluminum box structure with a partition running down the middle. The partition will serve as an optical baseplate and will also electronically isolate the analog from the digital signal processing. The size of the sensor will be approximately 50 cm x 30 cm x 30 cm. Two optic trains will be mounted on the partition in parallel. Each optic train consists of essentially two modular assemblies which are divided by the chopper wheel. The objective lens will be contained in the front assembly and the rest of the optics including the detector and the pre-amplifier will be contained in the other assembly.

The chopper wheel will be mounted on the baseplate in order to reduce the mechanical vibration propagated to the optic trains. The total electric power consumption is estimated to be no more than 30 watts.

The chopper wheel will be contained in a thermally insulated cage and the temperature of the cage will be controlled to maintain 296 K.

On the other side of the partition, the remainder of the electronics will be contained.

There will be two analog signal outputs; one the difference signal for methane and another the ratio between difference signals for ethane and methane. The two signals will be recorded on the same chart recorder and compared in order to check correlations between themselves. The correlation between the two signals is an important feature to be used in a false alarm check. The condition when the methane signal becomes high and both signals show high correlation will indicate a gas leak. The level of the methane signal as well as the correlation value will be decided based on the signal to noise calculation.

9. PLAN FOR THE FIELD TEST

The field test shall be carried out using a simulated pipeline leak. The objectives of the field test are as follows:

- Confirmation of the signal processing concept: this also includes separate field mapping for the ground temperature and the ground emissivity.

- Test of the gas dispersion model: this includes an establishment of a conversion factor between the mixing ratio and the leak rate, and the optimum down-wind distances to be viewed by the sensor for given wind speeds and leak rates.

- Test on atmospheric condition: the optimum time of day will be established in terms of the atmospheric stability and the atmospheric temperature lapse rate.

10. WORK STATEMENT

Phase II - Detail Design & Fabrication

During this phase the detailed optical, mechanical and electronic design shall be carried out. To begin, all long lead items identified in Phase I shall be specified and procured. Upon completion of the detailed design phase optical, mechanical and electronic subassemblies shall be fabricated and assembled. All subsystems shall be tested and debugged prior to system integration and testing.

A detailed laboratory acceptance test plan and test procedures shall be prepared and submitted to the contract scientific authority at least 30 days prior to commencement of testing.

The laboratory testing shall be defined to completely evaluate the instrument performance for the expected range of atmospheric and ground conditions (gas and surface temperatures). Tests will be performed to determine limiting noise mechanisms and establish signal, range and limits of detection for both methane and ethane.

Upon completion of all testing and documentation of test data a Phase II review meeting shall be held at MONITEQ when a demonstration of the instrument performance shall be carried out.

Phase II will be completed with a report containing a full documentation package of detailed drawings and test data. Included in this report will be a detailed schedule for Phase III field tests and a preliminary field test plan.

Phase II - Detailed Tasking

Task	Project Manager	System Engineer	Electronic Engineer	Digital Engineer	Technician	Drawing Office
Project Management	12	-	-	-	-	-
Mechanical Design	-	10	-	-	-	10
- detailing	-	5	-	-	-	30
Analog Electronics						
- signal processing	-	3	10	-	10	-
- timing decoding	-	2	5	-	10	-
- motor controls	-	2	5	-	15	-
- solenoid drivers	-	-	1	-	2	-
- pick offs	-	-	2	-	5	-
Digital Electonics						
- system	-	2	1	3	20	-
- programming	-	1	-	50	-	-
Electronic Documentation	-	1	2	-	-	10
Wiring Cable Assembly	-	-	-	-	20	-
Instrument Assembly	-	-	-	-	10	-
Debug & Test	-	2	3	2	10	-
Calibration & Evaluation	-	15	5	5	15	-
Reporting & Manual Preparation	2	10	2	2	-	10
Design Review	1	1	1	1	2	2
	15	53	37	63	119	62

Direct Personnel

Project Manager	@ $339.00/day x 15 =	$ 5,085
System Engineer	@ $240.00/day x 53 =	12,720
Electronic Engineer	@ $299.45/day x 37 =	11,080
Digital Engineer	@ $277.00/day x 63 =	17,451
Technician	@ $203.00/day x 119 =	24,157
Drawing Office	@ $220.00/day x 62 =	13,640
		$70,493

Sub-Contract

Drafting	@ $220.00/day x 62 =		$13,640
Fee at 7.5% of Direct Labour			5,287
			$89,420

Materials (estimated with Duty & Federal Sales Tax included)

Electronics	$ 4,000	
Digital	3,000	
Optical	20,000	
Machining	6,000	
Other	2,000	
		$35,000

Computing

CCRS Landline (3 months @ $250/mos)	$ 750	
AIP Development System	2,000	
		2,750

Travel & Living

2 man trips to Ottawa @ $250/trip	$ 500	
		500
		38,250
		$127,670

REFERENCES

1) Barringer, A.R. and Davies, J.H., Further Developments in Correlation Spectroscopy for Remote Sensing Air Pollution, 2nd Joint Conference on Sensing of Environmental Pollutants, Washington, D.C., December, 1973.

2) Davies, J.H., Correlation Spectroscopy Measurements of Air Pollution, 2nd European Electro-Optical Conference, Geneva, Switzerland, December, 1973.

3) Bortner, M.H., Dick, R., Goldstein, H.W., Grenda, R.N. and Levy, G.M., Development of a Breadboard Model Correlation Interferometer for the Carbon Monoxide Pollution Experiment, General Electric Co. Report NASA CR-112212, March, 1973.

4) Goldstein, H.W., Bortner, M.H., Grenda, R.N., Karger, A.M. and Level, P.O., Correlation Interferometric Measurement of Trace Species in the Atmosphere, AIAA Paper #73-515, International Conference on the Environmental Impact of Aerospace Operations in the High Atmosphere, Denver, June, 1973.

5) Ludwig, C.B., Griggs, M., Malkmus, W. and Bartle, E.R., Applied Optics, 13, 1494, 1974.

6) Ward, T.V. and Zwick, H.H., Gas Cell Correlation Spectrometer: GASPEC, Applied Optics, Vol. 14, No. 12, 2896, December, 1975.

7) A.I.P. Handbook, 3rd Edition, McGraw-Hill.

8) Derr, V.E., Remote Sensing of the Troposphere, NOAA Report Ed.

Rouse, W.R., Noad, D. and McCutcheon, J., Radiation Temperature and Atmospheric Emissivities in a Polluted Urban Atmosphere at Hamilton, Ontario, Journal of Applied Meteo., Vol. 12, 798, 1973.

9) Kalshoven, J.E., Korb, C.L., Schwemmer, G.K. and Dombrowski, M., Laser Remote Sensing of Atmospheric Temperature by Observing Resonant Absorption of Oxygen, Applied Optics, Vol. 20, No. 11, June, 1981.

10) The Infrared Handbook, Wolfe, Zessis, ONR, 1978.

11) Leeman, V., Earing, D., Vincent, R.K. and Ladd, S., The NASA Earth Resources Spectral Information System: A Data Compilation, 1971.

12) Private Communications with Ms. Stearns at NOAA.

13) AFCRL-TR-73-0096, 26 January 1973, Environmental Research Papers, No. 434.

14) Pine, A.S., High Resolution Methane ν_3-band Spectra Using a Stabilized Tunable Difference-Frequency Laser Systems, Journal of Optical Society of America, Vol. 66, No. 2, February, 1976.

15) Chedin, A., Huson, N., and McDowell, R.S., ν_4-band of Methane. Line Parameters and Evaluation of Jovian Atmospheric Transmission at 7.7 μm, Journal of Mol. Spec., 71, 343-368, 1978.

16) McDowell, R.S., The ν_3 Infrared Bands of $C^{12}H_4$ and $C^{13}H_4$, Journal of Mol. Spec., 21, 280-290, 1966.

17) Pinson, P., Dupre-Maquaire, J., The High Resolution Spectrum of CH_4. The Q Branch of the ν_4-band, Journal of Optical Spec., 78, 170-174, 1979.

18) Restelli, G. and Cappellani, F., High Resolution Spectroscopy of the ν_4-band of Metahne, Journal of Mol. Spec., 78, 161-169, 1979.

19) Potter, R.F., Pernett, J.M. and Naugle, A.B., The Measurement and Interpretation of Photodetector Parameters, Proceedings of the IRE, p. 1503, September, 1959.

Number/
Numéro
2

DESIGN & FABRICATION OF AN AIRBORNE REMOTE SENSING SYSTEM FOR GAS PIPE-LINE LEAK DETECTION

DSS File No. 15SQ.23440-0-9103

PHASE I - CONCEPTUAL DESIGN REPORT

REQ.NO.O-9103

Monitoring Environmental Quality
Moniteq Ltd., 630 Rivermede Road, Concord, Ontario, Canada L4K 1B6 (416) 669-5334 Cable: Monteq Toronto

CONTRACT REPORT NO.1SQ81-00003

DESIGN & FABRICATION OF AN AIRBORNE REMOTE SENSING SYSTEM FOR GAS PIPE-LINE LEAK DETECTION

DSS File No. 15SQ.23440-0-9103

PHASE I - CONCEPTUAL DESIGN REPORT

Appendix I & II

MTR#81-27
September, 1981

41 pp

MICROMEDIA
JUL 2 9 1983

APPENDIX I

ATTENDANCE

MONITEQ GASPILS REVIEW MEETING, Sept. 2, 1981

1.	Dr. Sang Lee	Project Leader	MONITEQ
2.	Mr. John Harron	Research Scientist	MONITEQ
3.	Harold Zwick	V.P. Technology	MONITEQ
4.	Victor Ward	V.P. Operations	MONITEQ
5.	Dr. Susan Till	Scientific Authority	CCRS
6.	Dr. Bob O'Neil	Sensors Section Head	CCRS
7.	Mr. John Mitchell	Strategic Studies	Transport Canada
8.	Mrs. Edith Jubenville	Engineer - Pipeline Facilities	TCP

GASPILS PHASE I REVIEW

CONCEPTUAL DESIGN PHASE

LOCATION: MONITEQ Ltd.

DATE: September 2, 1981, 10:00 a.m.

AGENDA OF REVIEW MEETING

A) A.M.

10:15	Historical Review
10:30	Phase I Project Review
12:00	Lunch

B) P.M.

1:30	Financial Summary of Phase 1
1:45	Future Plans
2:15	General Discussion

Historical Overview

1972 - 74	Texaco Exploration/BRL CH_4/C_2H_6
1978	T.C.P.L. evaluation of I.R. technology
1978	MONITEQ field tests with modified CCRS GASPEC
1979	Proposal submitted to T.C.P.L.
1980	Revised proposal submitted as U.P. to D.S.S.
1981 April	Contract awarded. Financially supported by D.S.S., T.C. and CANMET with technical and field testing support from C.C.R.S.
1981 Sept.	Phase I Conceptual Design Review

Sensor Selection

Instrument	Sensitivity	Specificity	Complexity Of Instrum.	Observ. Time	Information Content	Remarks
Radiometer (filter wheel or many single filters)	Medium	Low	Low	Short	Medium	Limit $\Delta\omega \sim 3\ cm^{-1}$; many channels required
Radiometer (polychromator)	Low Medium	High Low	Medium	Short Short	Medium	Assuming $\Delta\omega < 1\ cm^{-1}$ Assuming $\Delta\omega > 1\ cm^{-1}$; Multiple detectors required
Scanning — Spectrometer	Low Medium	High Low	Medium	Long Medium	High	Assuming $\Delta\omega < cm^{-1}$ Assuming $\Delta\omega > cm^{-1}$
Optical Correlation Instrument	High	High	Medium	Short	Medium	Matched filter with multiple entrance slits and nondispersive
Interierometer — Spectrometer	High	High	High	Medium	High	Sampling time at least 10 sec; image motion compensation required; large information content for wide spectral interval

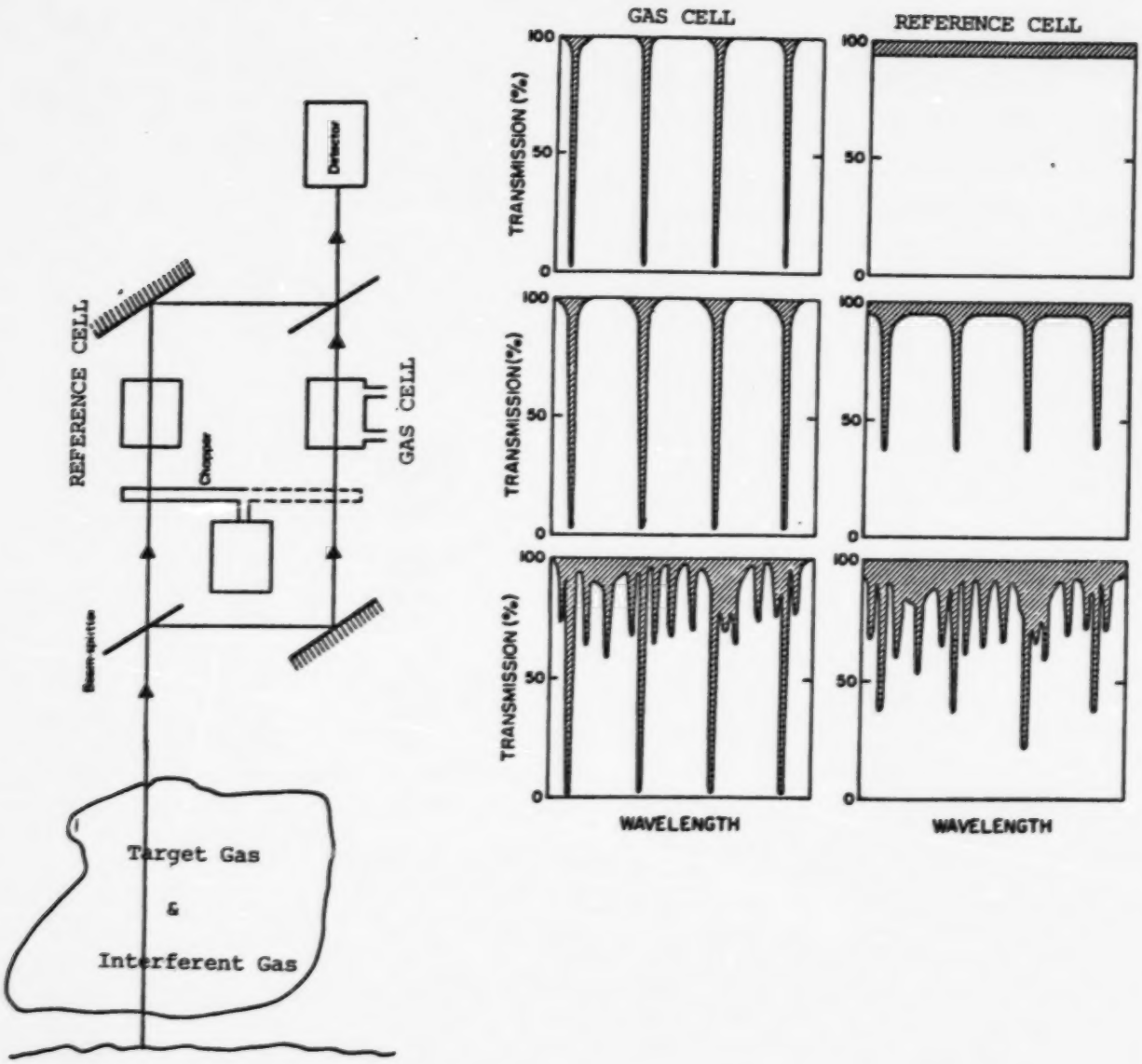

PRINCIPLE OF OPERATION

TARGET GASES

CH_4 AND C_2H_6

SPECTRAL BANDS

CH_4	3.4
	7.8
C_2H_6	3.4
	12.2

NATURAL GAS – VARIOUS FIELDS

	METHANE %	ETHANE %	PROPANE %	BUTANE %	OTHER %
MICHIGAN	75.80	17.50	0	0	6.70
PENNSYLVANIA (Leidy)	96.80	2.5	.20	0	.50
TEXAS (Hugoton(A))	79.00	6.31	2.20	.07	12.42

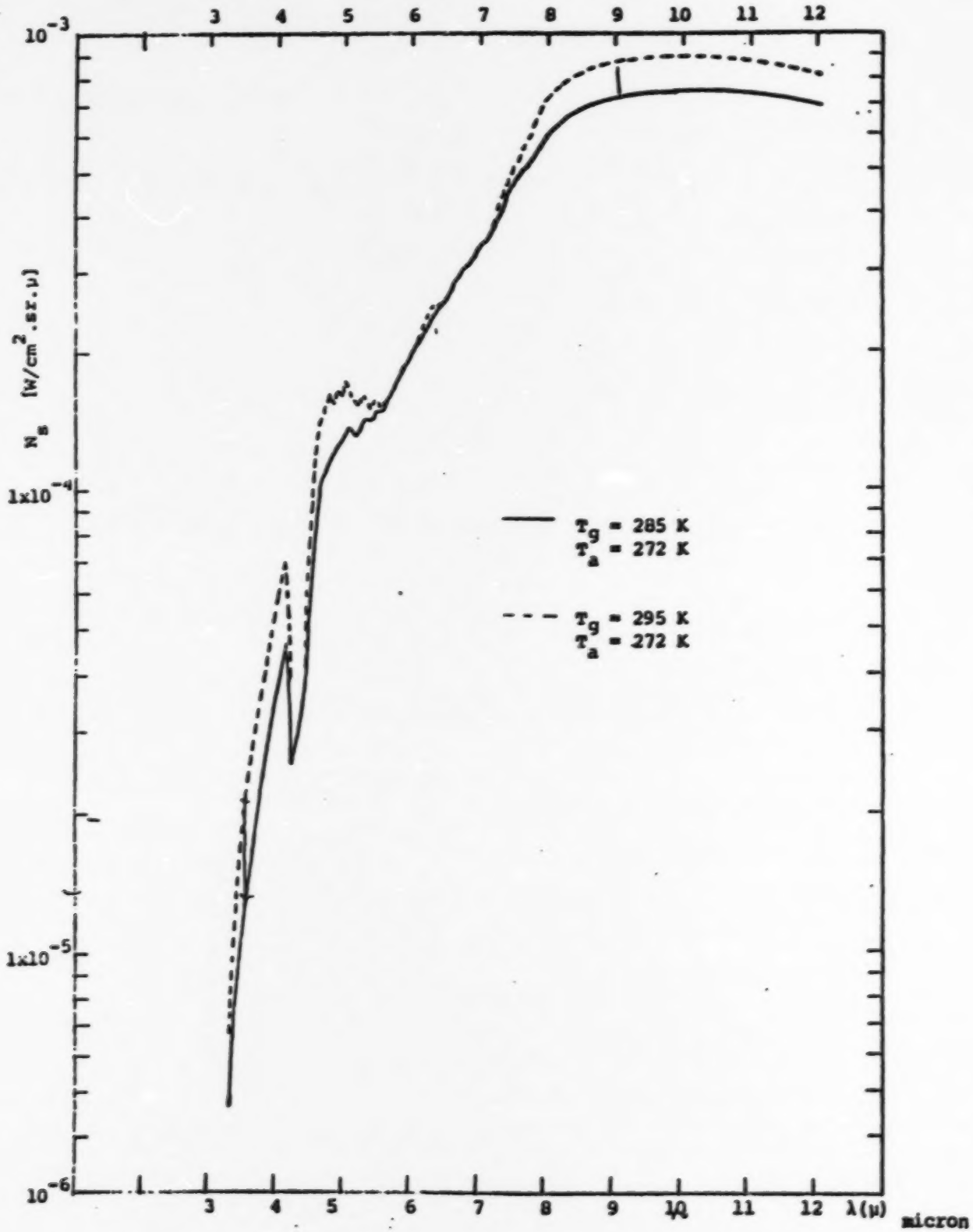

FIGURE 6: Upwelling Radiance at 1.1 km Altitude vs. Wavelength for Two Different Ground Temperatures

$$\text{OUTPUT} = \int_{\Delta\nu} P_S \cdot T_A \cdot (T_C - \chi \cdot T_R)\, d\nu$$

DIFFERENCE SIGNAL

$$\Delta S = \eta_C A \Omega (\varepsilon \bar{B}_E - \bar{B}_A) \left[\int_{\Delta\nu} T_A T_C \, d\nu - \frac{1}{\Delta\nu} \int_{\Delta\nu} T_A \, d\nu \int_{\Delta\nu} T_C \, d\nu \right] + J_C$$

$$= \eta_C A \Omega (\varepsilon \bar{B}_E - \bar{B}_A) (\overline{T_A T_C} - \bar{T}_A \bar{T}_C) \Delta\nu + J_C$$

DIFFERENCE SIGNAL IN THE PRESENCE OF THE SOLAR RADIATION

$$\Delta S = \eta_C A \Omega \left[(\bar{N}_X - \bar{B}_S) R (\overline{T_S T_A T_C} - \overline{T_S} \bar{T}_A \bar{T}_C) \right.$$

$$\left. + (\bar{B}_S R + \varepsilon \bar{B}_E - \bar{B}_A) (\overline{T_A T_C} - \bar{T}_A \bar{T}_C) \right] \Delta\nu$$

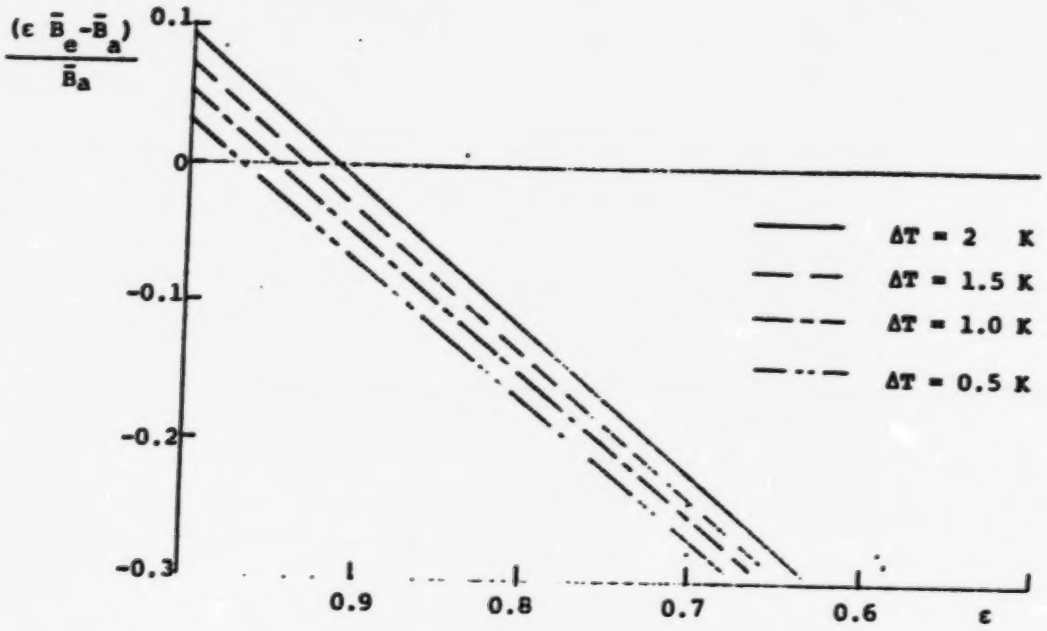

FIGURE 2: $(\varepsilon \bar{B} - \bar{B}_a)/\bar{B}_a$ as a function of the ground emissivity for various ΔT at $\lambda = 3.4\ \mu$

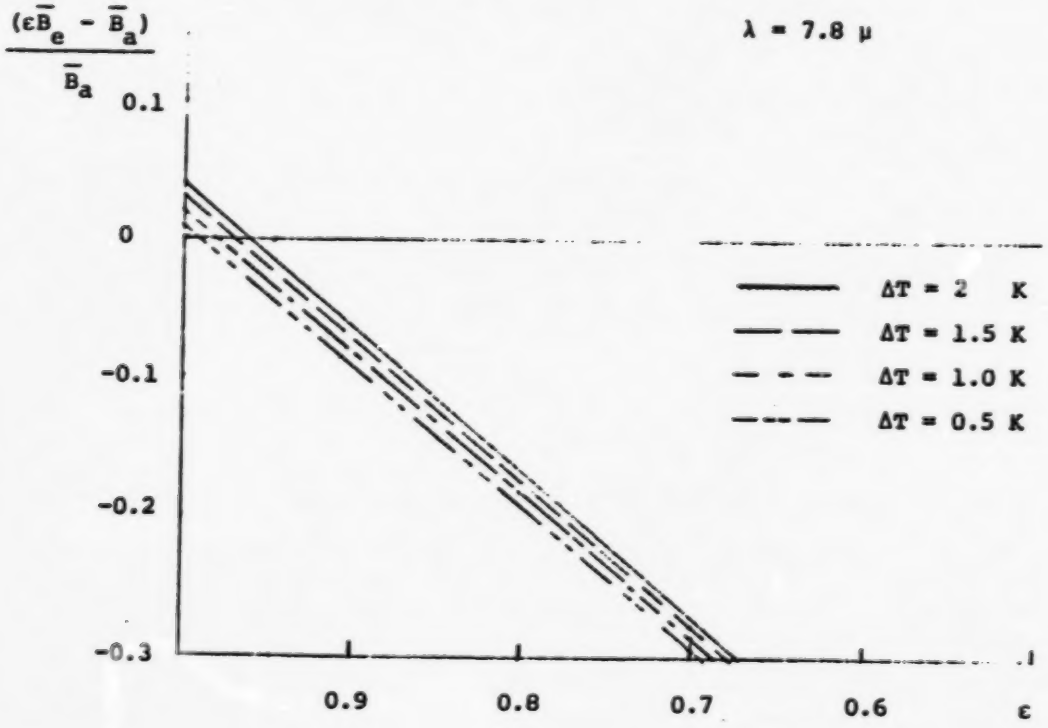

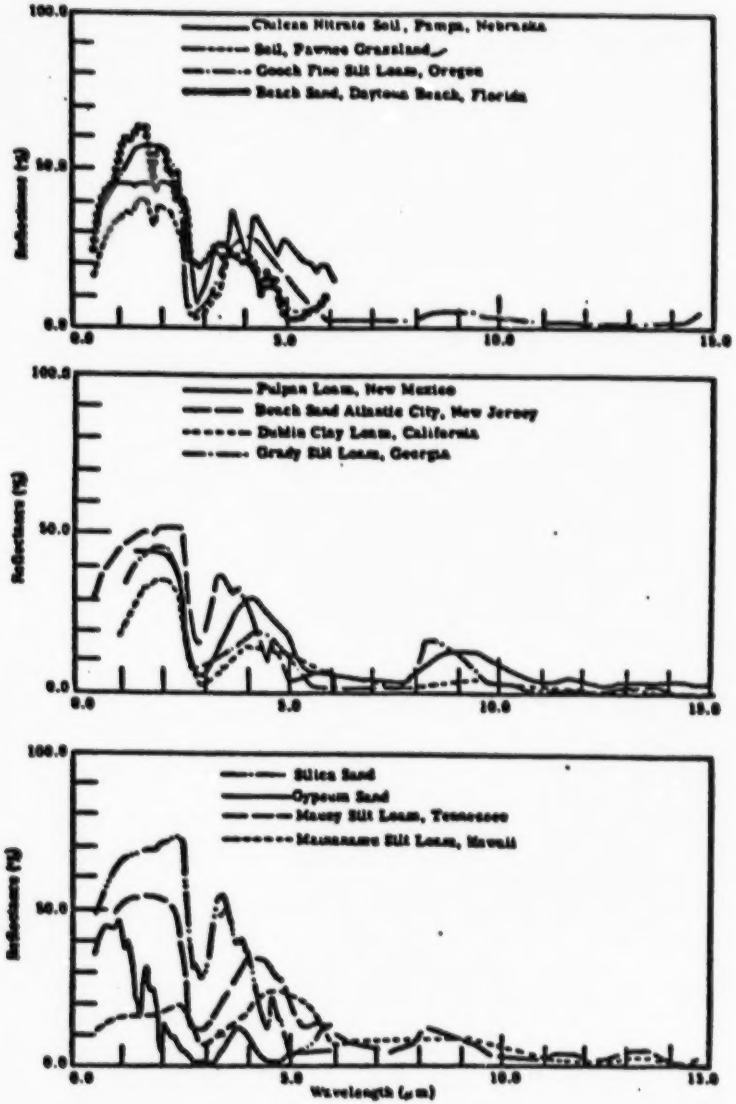

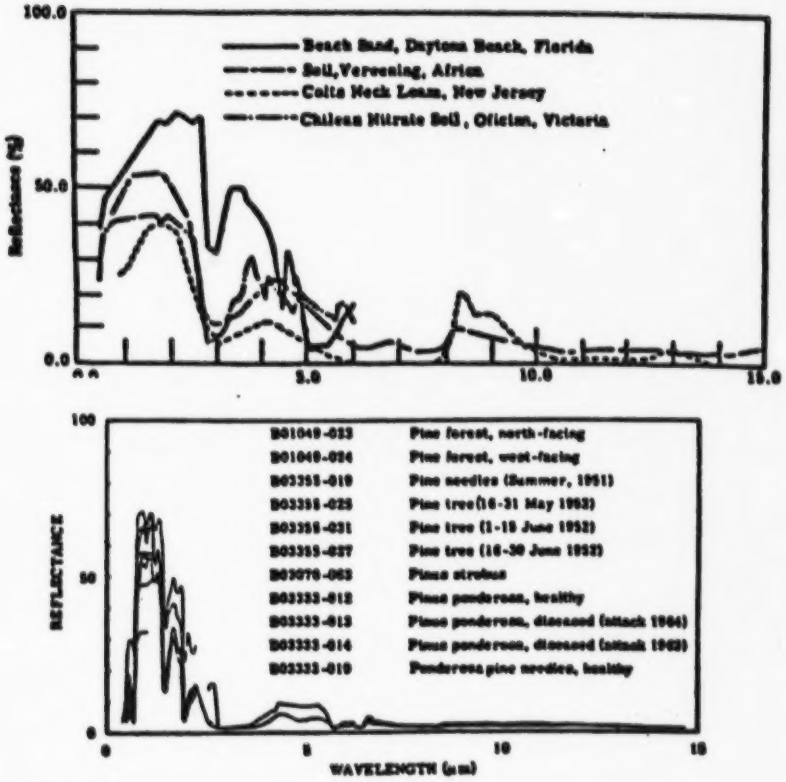
Beach Sand, Daytona Beach, Florida
Soil, Vereening, Africa
Colts Neck Loam, New Jersey
Chilean Nitrate Soil, Ofician, Victoria
B01049-023 Pine forest, north-facing
B01049-024 Pine forest, west-facing
B02355-019 Pine needles (Summer, 1951)
B02355-025 Pine tree (16-31 May 1952)
B02355-031 Pine tree (1-15 June 1952)
B02355-037 Pine tree (16-30 June 1952)
B03070-063 Pinus strobus
B03333-012 Pinus ponderosa, healthy
B03333-013 Pinus ponderosa, diseased (attack 1964)
B03333-014 Pinus ponderosa, diseased (attack 1962)
B03333-010 Ponderosa pine needles, healthy
REFLECTANCE
WAVELENGTH (μm)

FIGURE 4: Ground reflection coefficient as a function of wavelength for various ground conditions[10,11]

$\lambda(\mu)$	$\bar{\varepsilon}$	$\Delta\bar{\varepsilon}$	$\Delta(\varepsilon\bar{B}_e-\bar{B}_a)/(\varepsilon\bar{B}_e-\bar{B}_a)$
3.4	0.85	±0.1	77%
7.8	0.95	±0.04	60%
12.2	0.95	±0.02	59%

TABLE 1: Expected emissivity variations

CORRELATION COEFFICIENT

$$\Delta\nu \cdot \rho = \int_{\Delta\nu} T_A T_C d\nu - \frac{1}{\Delta\nu} \int_{\Delta\nu} T_A d\nu \int_{\Delta\nu} T_C d\nu$$

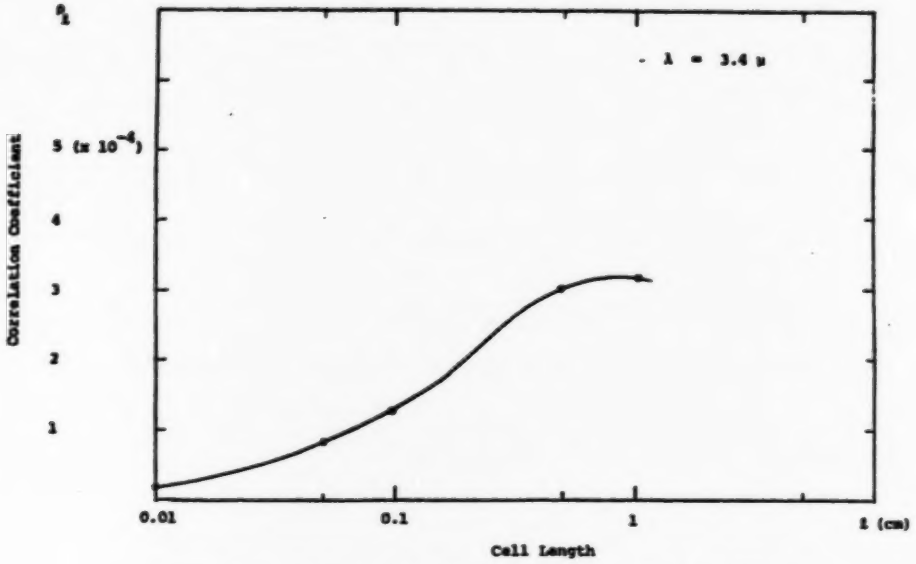

FIGURE 11: The correlation coefficient for 10 ppm.M CH_4 leak gas as a function of the cell length.

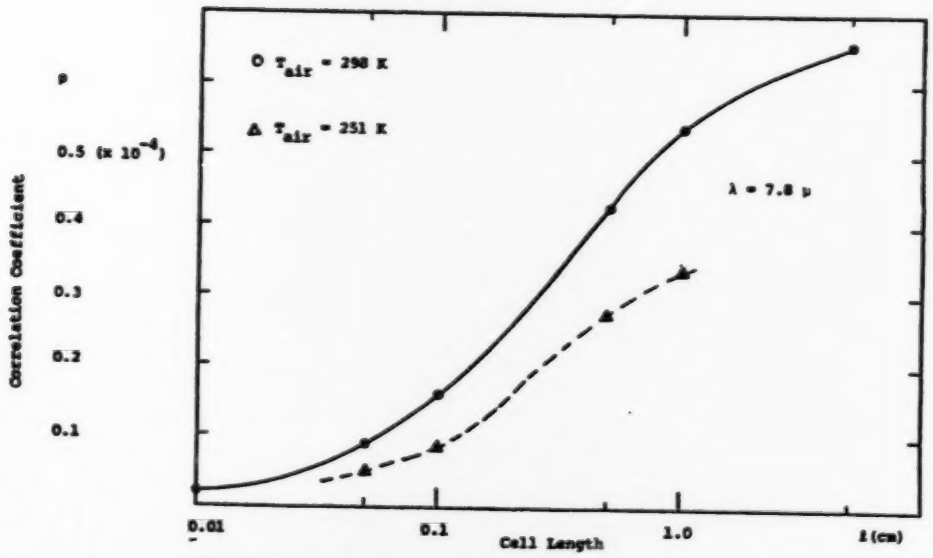

FIGURE 16: The correlation coefficients for 10 ppm.M CH_4 leak gas as a function of the cell length

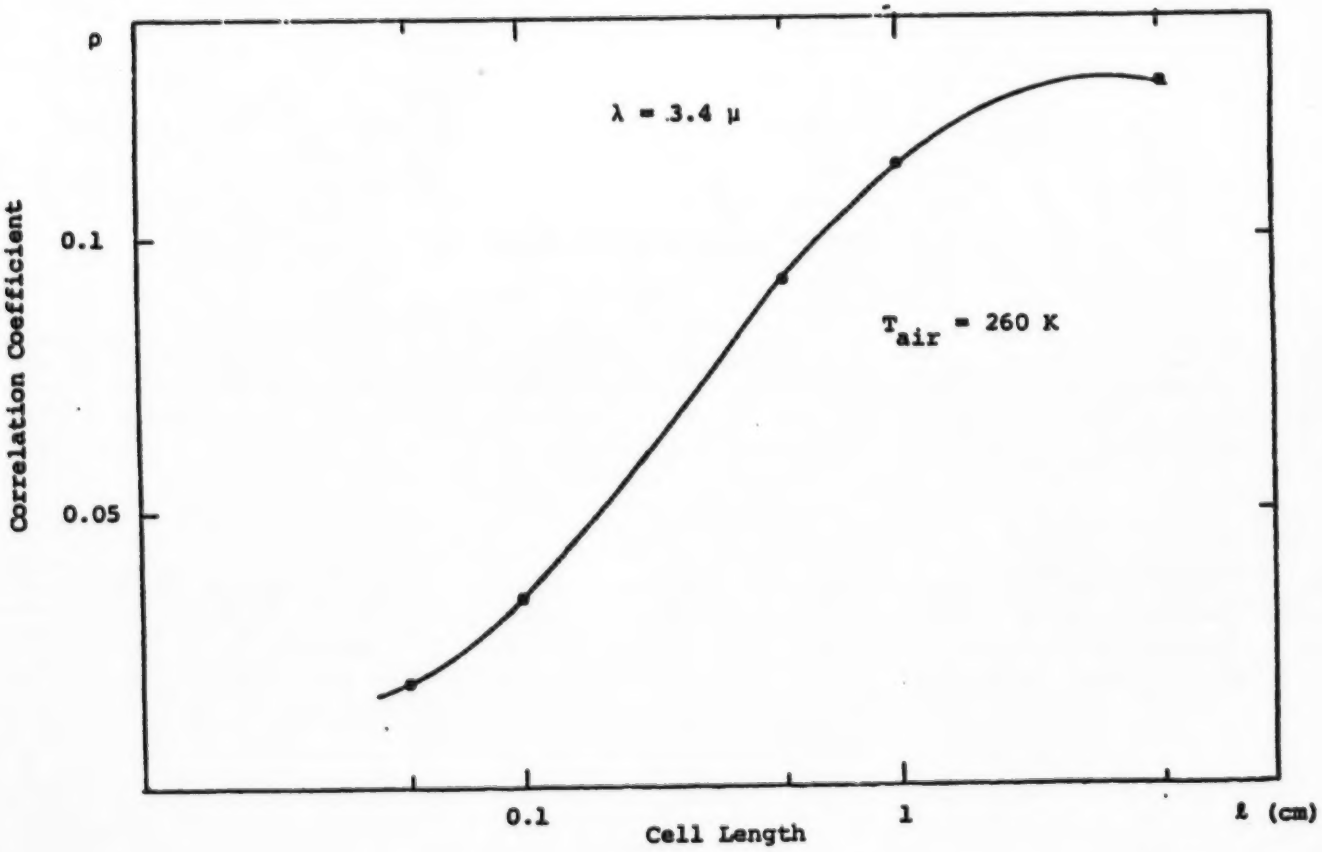

FIGURE 12: The correlation coefficient of the total residual CH_4 for 2X scale height (24.5 torr.M)

λ	3.4 μ	7.8 μ
ρ_ℓ (10 PPM.M)	3.3×10^{-4}	0.55×10^{-4}
$\frac{\partial \rho}{\partial \theta}$	1.9×10^{-5}/K	9.3×10^{-6}/K
$\frac{\partial I}{\partial \theta}$	9.5×10^{-4}/K	3.3×10^{-4}/K
$\frac{\rho(\theta_G=251\ K)}{\rho(\theta_G=300\ K)}$	(0.62)	0.62

RESULTS OF THE MODEL CALCULATION

NOISE CONTRIBUTIONS AT INPUT

Optical Power W	Detector Output V	Amplifier Gain G_1	PbS Detector (3.4μm) (v/√Hz)	Amplifier A_1 v/√Hz	Amplifier A_2 v/√Hz	Amplifier A_3 v/√Hz	e_{total} v/√Hz	Noise Voltage v	Fractional Noise Components	Fractional Thermal Drift $G_1 E$ = 10V (1°C change)
10^{-7}	5×10^{-2}	200	3.3×10^{-7}	1.5×10^{-8}	10^{-10}	1.5×10^{-9}	3.3×10^{-7}	4.3×10^{-7}	8.6×10^{-6}	2.5×10^{-5}
10^{-8}	5×10^{-3}	2000	3.3×10^{-7}	1.5×10^{-8}	——	——	3.3×10^{-7}	4.3×10^{-7}	8.6×10^{-5}	2.5×10^{-5}

Optical Power W	Detector Output V	Amplifier Gain G_1	(Worst Case) NqCdTe v/√Hz	Amplifier A_1 v/√Hz	Amplifier A_2 v/√Hz	Amplifier A_3 v/√Hz	e_{total} v/√Hz	Noise Voltage v	Fractional Noise Components	Fractional Thermal Drift $G_1 E$ = 10V (1°C change)
10^{-6}	10^{-3}	10^{4}	1.25×10^{-8}	1.5×10^{-8}	——	——	1.25×10^{-8}	2.6×10^{-9}	2.6×10^{-6}	2.5×10^{-5}
10^{-7}	10^{-4}	10^{5}	1.25×10^{-8}	1.5×10^{-8}	——	——	1.25×10^{-8}	2.6×10^{-9}	2.6×10^{-5}	2.5×10^{-5}

SYSTEM PARAMETERS

PARAMETERS \ BAND	No. 1	No. 2	No. 3	UNIT
Gas	CH_4 C_2H_6	CH_4	C_2H_6	
λ	3.4	7.8	12.2	μm
$\Delta\lambda$	.25	.40	.40	μm
α (Absorption Coefficient)	.60 for CH_4 .73 for C_2H_6	.10	.80	$cm^{-1}\ atm^{-1}$
B_e	0.2	8.9	9.1	$10^{-4} w/(cm^2 \cdot \mu m \cdot Sr)$
$\bar{\varepsilon}$	0.85	0.95	0.95	-
$\frac{\varepsilon \bar{B}_e - \bar{B}_a}{B_a}$ $(=N_s/\bar{B}_a)$	0.15	0.04	0.03	-
Etendu †	7.4	7.4	7.4	$10^{-2} cm^2 Sr$
T_e (Lens Transmission)	.98	.98	.98	-
T_f (Filter Transmission)	0.30	0.30	0.30	-
T_t $(=T_e^3\ T_f)$	0.27	0.27	0.27	-
P $(=N_s A\Omega T_t \Delta\lambda)$	0.15	2.8	1.5	$10^{-7} w$
Detector	PbS	HgCdTe	HgCdTe	-

P ($=N_s A\Omega T_t \Delta\lambda$)	0.15	2.8	1.5	10^{-7} w
Detector	PbS	HgCdTe	HgCdTe	-
D* ($^{low}_{high}$)	150 200	6.5 30	8.5 30	10^9 cm$\sqrt{Hz}$/w
Δf	1.7	1.7	1.7	Hz
Duty Factor	0.70	.70	.70	-
NEP†† ($^{low}_{high}$)	0.32 0.25	7.7 1.7	6.0 1.7	10^{-11} w
NEP/P ($^{low}_{high}$)	2.1 1.7	2.8 0.6	4.0 1.1	10^{-4} 10^{-4}
ρ†††/(10 ppm.M CH_4)	3.3	0.55	-	10^{-4}
k*	0.55	0.55		
ρ/(10 ppm.M C_2H_6)	4.0		4.4	10^{-4}
Detection Limit for CH_4 ($^{low}_{high}$)	6.5 5.2	50 11	- -	ppm.M
Detection Limit for C_2H_6 ($^{low}_{high}$) ††††	5.3 4.3	-	9.1 2.5	- -
Δ S/S for Detection Limit	4.3	1.1	1.3	10^{-5}
$\Delta\theta$** (Temperature Stability Limit)	.23	.83		K

TABLE 2

SUMMARY OF NOISE

	CH_4		C_2H_6	
	3.4	7.8	3.4	12.2
Ground Effect	55	10	-	-
Solar Effect	1000	1	1	0
Detector	1	1	1	1
Signal Processing				
Electronic Preamp	0.1	0.5	0.1	0.5
Gate Jitter	0.1	0.1	0.1	0.1
Thermal Drift	2	2	2	2
Chopper Temp. Drift	.5	.2	.5	.5

INPUT WIND SPEED(M/S): 3.
INPUT LEAK RATE(M**3/S): 0.01
INPUT SENSOR FOOTPRINT(M): 40.

VERTICALLY INTEGRATED CONCENTRATION FOR VARIOUS DOWNWIND DISTANCE

FOR PASQUILL STABILITY CLASS, A, THE VERTICAL CONCENTRATIONS ARE EXPRESSED IN PPM-M FOR DISTANCES OF 10-1000 METRES FROM THE SOURCE

	10	20	30	40	50	60	70	80	90	100
0	100.0000	99.9995	99.7593	97.7230	93.1654	87.1411	80.7507	74.6098	68.9721	63.9086
100	59.4015	55.4004	51.8462	48.6811	45.8528	43.3158	41.0310	38.9651	37.0899	35.3813
200	33.8195	32.3866	31.0679	29.8507	28.7241	27.6786	26.7059	25.7987	24.9509	24.1569
300	23.4119	22.7113	22.0515	21.4291	20.8410	20.2845	19.7571	19.2566	18.7812	18.3286
400	17.8977	17.4868	17.0945	16.7197	16.3612	16.0179	15.6890	15.3735	15.0706	14.7797
500	14.5000	14.2368	13.9717	13.7220	13.4812	13.2489	13.0247	12.8081	12.5987	12.3963
600	12.2003	12.0107	11.8270	11.6489	11.4763	11.3089	11.1464	10.9886	10.8354	10.6865
700	10.5418	10.4010	10.2641	10.1308	10.0011	9.8748	9.7517	9.6317	9.5148	9.4007
800	9.2895	9.1809	9.0749	8.9715	8.8705	8.7717	8.6753	8.5810	8.4889	8.3987
900	8.3106	8.2243	8.1399	8.0573	7.9764	7.8972	7.8194	7.7435	7.6690	7.5960

FOR PASQUILL STABILITY CLASS, B, THE VERTICAL CONCENTRATIONS ARE EXPRESSED IN PPM-M FOR DISTANCES OF 10-1000 METRES FROM THE SOURCE

	10	20	30	40	50	60	70	80	90	100
0	100.0000	100.0000	99.9970	99.8259	98.7798	96.3344	92.6860	88.3291	83.7022	79.0969
100	74.6794	70.5314	66.6840	63.1393	59.8945	56.8996	54.1620	51.6489	49.3384	47.2103
200	45.2463	43.4301	41.7470	40.1839	38.7292	37.3727	36.1053	34.9189	33.8063	32.7610
300	31.7774	30.8504	29.9753	29.1480	28.3648	27.6224	26.9177	26.2480	25.6108	25.0037
400	24.4249	23.8723	23.3443	22.8393	22.3559	21.8925	21.4482	21.0218	20.6121	20.2183
500	19.8395	19.4748	19.1234	18.7847	18.4580	18.1426	17.8380	17.5436	17.2590	16.9837
600	16.7172	16.4591	16.2090	15.9665	15.7314	15.5033	15.2818	15.0668	14.8579	14.6548
700	14.4574	14.2653	14.0784	13.8965	13.7194	13.5469	13.3788	13.2149	13.0552	12.8993
800	12.7473	12.5989	12.4541	12.3126	12.1745	12.0395	11.9076	11.7786	11.6526	11.5293
900	11.4086	11.2906	11.1751	11.0620	10.9512	10.8428	10.7365	10.6325	10.5305	10.4305

FOR PASQUILL STABILITY CLASS, C, THE VERTICAL CONCENTRATIONS ARE EXPRESSED IN PPM-M FOR DISTANCES OF 10-1000 METRES FROM THE SOURCE

	10	20	30	40	50	60	70	80	90	100
0	100.0000	100.0000	100.0000	99.9995	99.9733	99.7629	99.0852	97.7499	95.7570	93.2338
100	90.3479	87.2545	84.0769	80.9045	77.7981	74.7964	71.9221	69.1869	66.5949	64.1453
200	61.8342	59.6557	57.6030	55.6689	53.8456	52.1262	50.5034	48.9705	47.5214	46.1501
300	44.8512	43.6196	42.4508	41.3403	40.2843	39.2791	38.3213	37.4078	36.5359	35.7028
400	34.9061	34.1437	33.4134	32.7133	32.0416	31.3968	30.7772	30.1815	29.6084	29.0566
500	28.5250	28.0125	27.5182	27.0411	26.5803	26.1351	25.7046	25.2882	24.8853	24.4951
600	24.1171	23.7508	23.3955	23.0509	22.7165	22.3917	22.0763	21.7699	21.4719	21.1822
700	20.9004	20.6261	20.3591	20.0990	19.8457	19.5989	19.3582	19.1236	18.8947	18.6714
800	18.4534	18.2407	18.0329	17.8299	17.6316	17.4378	17.2483	17.0631	16.8819	16.7047
900	16.5312	16.3615	16.1953	16.0326	15.8732	15.7171	15.5642	15.4143	15.2674	15.1233

Signal Processing

Output (1) ΔS_{CH_4}

(2) $\Delta S_{C_2H_6} / \Delta S_{CH_4}$

For the leak gas signal
(1) and (2) both are high

For false signal
(1) is high (2) is low

Optics Design Objectives

I) Good rejection of the spectrum of the blackbody radiation outside the spectral band of the target gas.

II) Minimize the modulated thermal radiation noise.

III) Maximize the signal power.

IV) Minimize any systematic correlations between the ground structure and optical components.

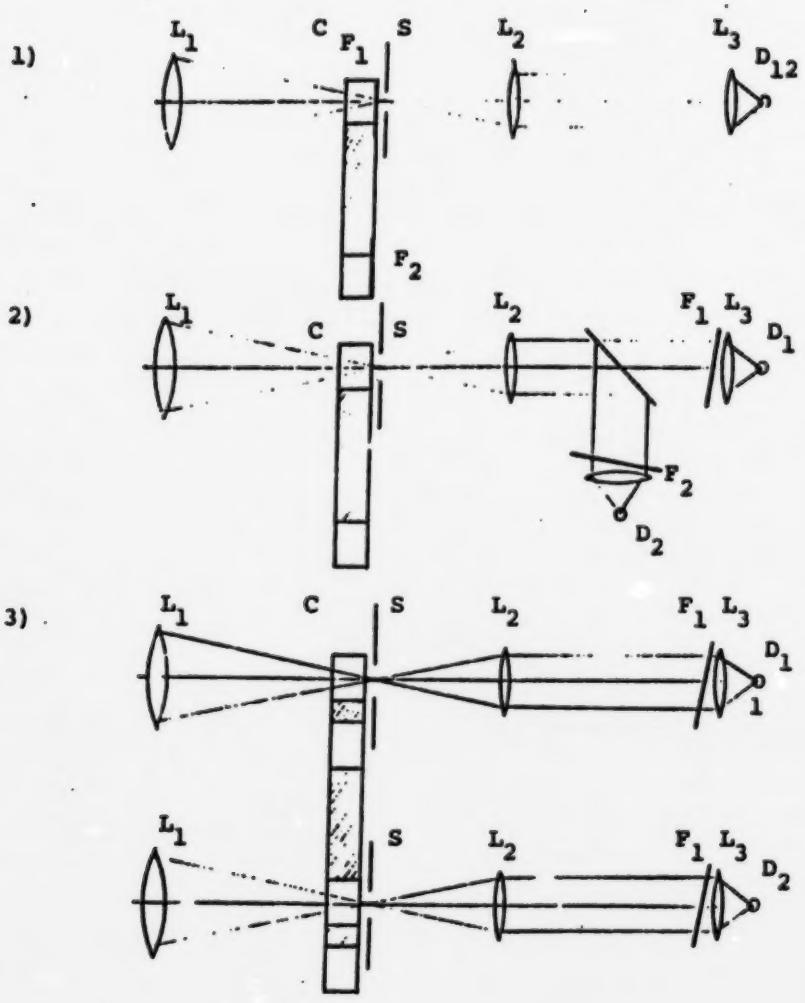

FIGURE 23: Schematics of optical configurations

L_1, L_2, L_3 = lenses

C = chopper

S = field stop

F = interference filter

D = detector

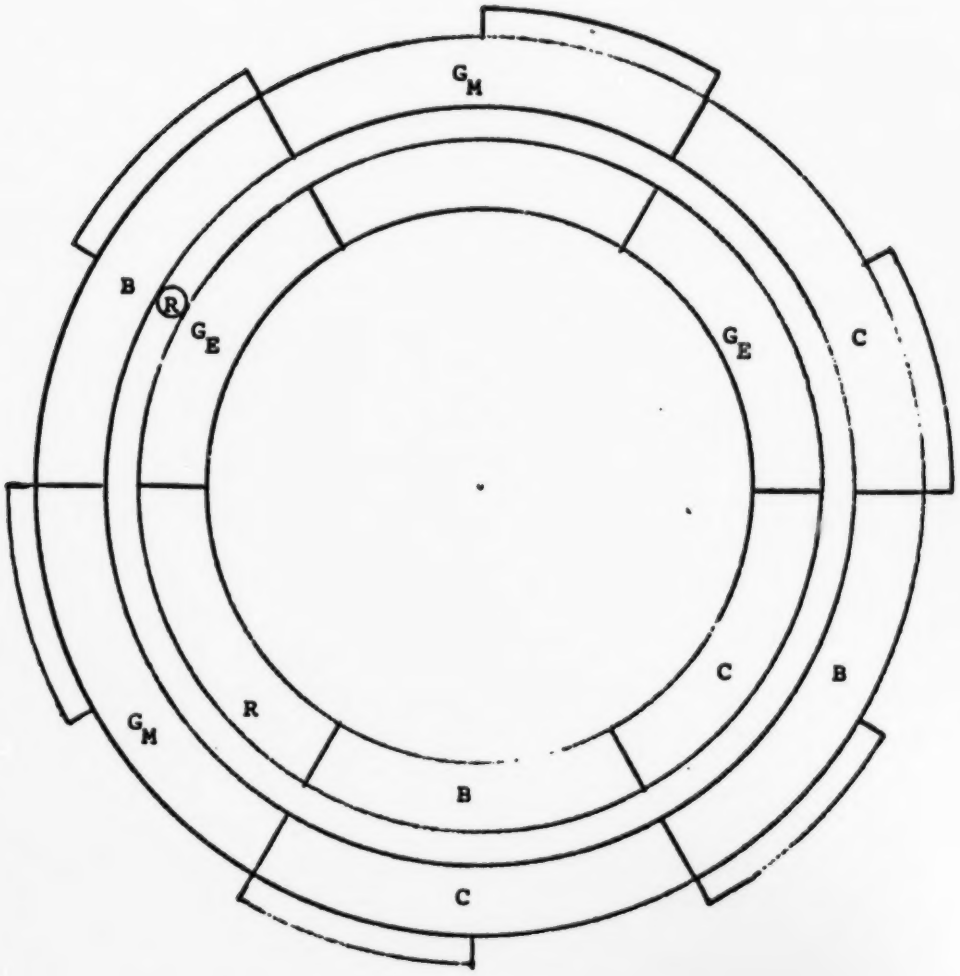

FIGURE 19: Chopper wheel configuration

G_M = methane gas cell

G_E = ethane gas cell

C = clean cell

B = blank

R = reset

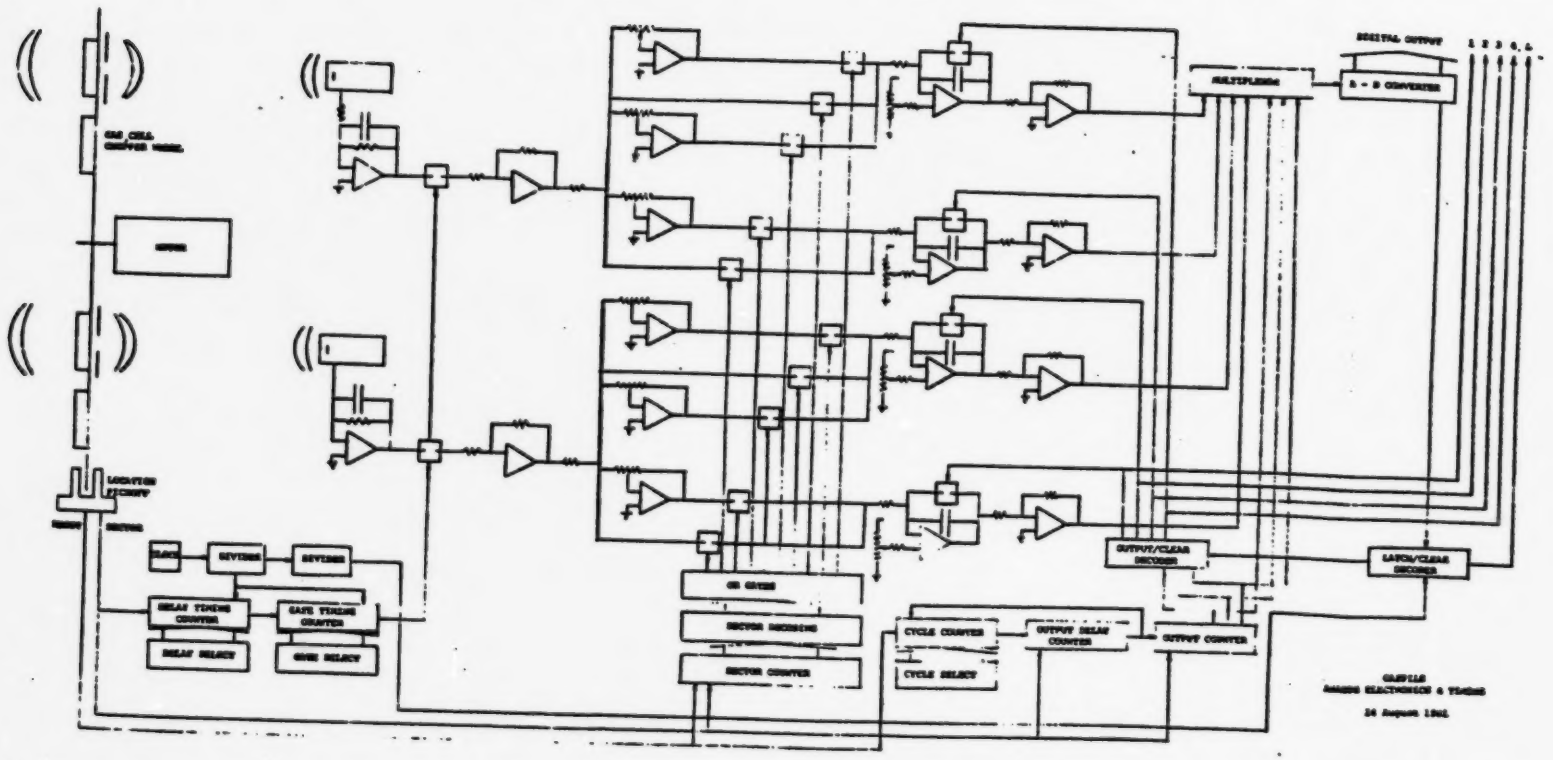
DIGITAL OUTPUT
MULTIPLEXER
A - D CONVERTER
OUTPUT/CLEAR DECODER
LATCH/CLEAR DECODER
OR GATES
SECTOR INCREMENT
SECTOR COUNTER
CYCLE COUNTER
CYCLE SELECT
OUTPUT DELAY COUNTER
OUTPUT COUNTER

Signal Balancing

$$S = T_C S_R - G_2 S_R + (1 - T_C) S_B - G_3 S_B$$

i) Set $G_2 = 1$

ii) Vary S_R, adjust G_3

iii) Vary S_B, adjust G_2

iv) Repeat (ii) and (iii)

Calibration

Using test gas cell — model calculation.

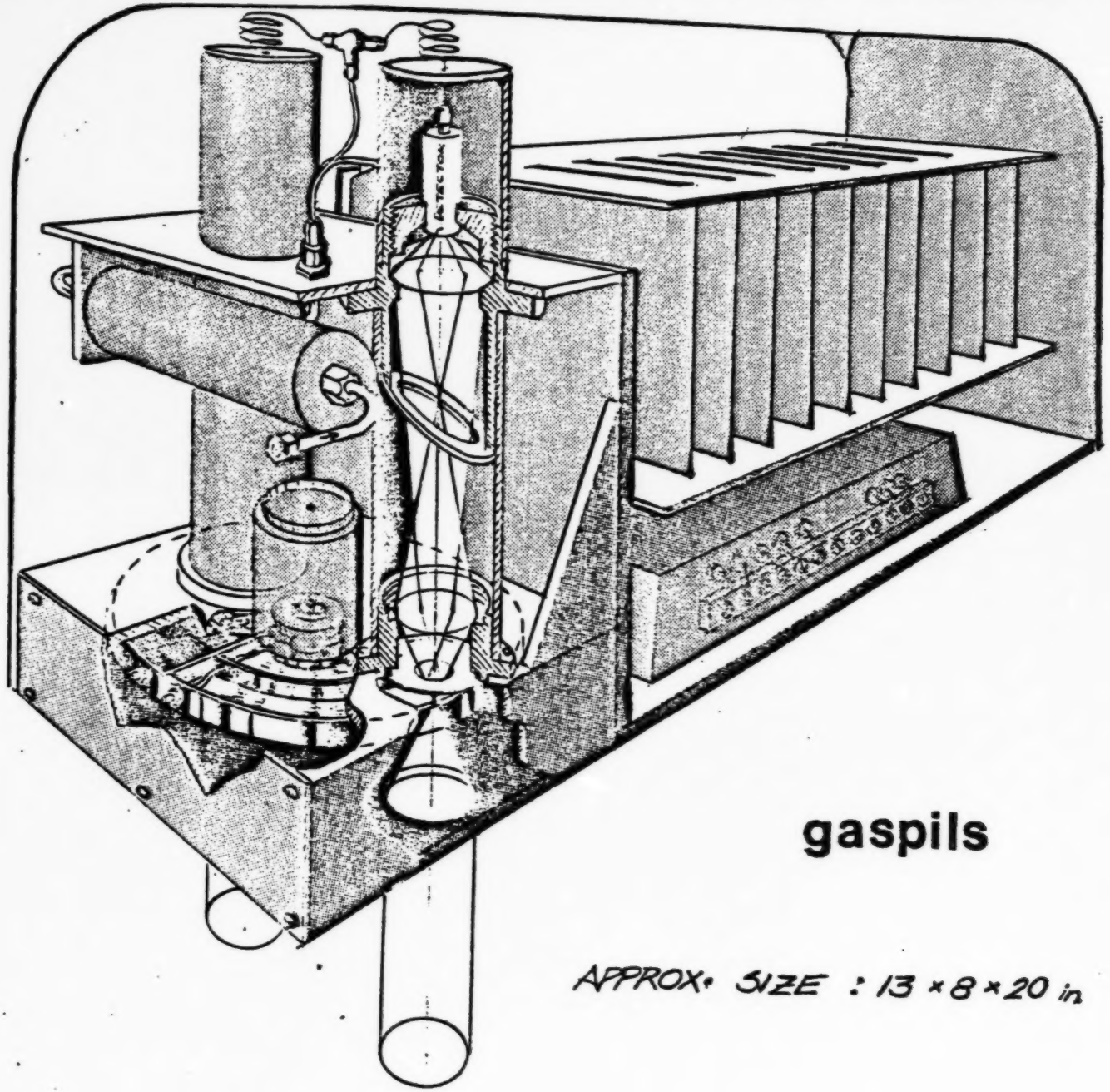

gaspils

APPROX. SIZE : 13 × 8 × 20 in

FUTURE PLANS

1. PHASE II GASPILS DEVELOPMENT
(SEPTEMBER - MARCH 1982) ($127,670)

- SPECIFICATIONS AND COMPONENT PROCUREMENT
- DETAILED OPTICAL /ELECTRONIC DESIGN
- FABRICATION AND ASSEMBLY
- DEBUGGING AND INITIAL SUB-ASSEMBLY TESTING
- LABORATORY TESTING
- ACCEPTANCE TESTING
- REPORTING

FUTURE PLANS

2. PHASE III GASPILS FIELD TRIALS AND OPERATIONAL EVALUATION (APRIL - NOVEMBER 1982) ($85,000.)

- INSTALLATION INTO CCRS AIRCRAFT WITH AUXILLARY SENSORS:
  - A) ALTITUDE (BARO AND RADAR ALTIMETER)
  - B) AIR TEMPERATURE
  - C) DUAL CHANNEL THERMAL IR, 3-5, 8-10, 10-12 MICRONS
  - D) PHOTOGRAPHY (9 x 9 COLOUR)

- INITIAL TRIALS OVER TERRAIN IN THE OTTAWA AREA (NO LEAKS NEEDED)

- TEST LEAKS:
  - A) SEVERAL KNOWN LEAK RATES AND GAS COMPOSITION
  - B) MEASUREMENT OF SURFACE (4' ABOVE SURFACE) CH_4, C_2H_6 CONCENTRATIONS AND SPATIAL VARIATIONS
  - C) MEASURED AIR TEMPERATURE
  - D) WINDSPEED AND DIRECTION

- FLIGHT TRIALS AT LOW ALTITUDE (500', 1000' AND 2000')

- DATA ANALYSIS AND INTERPRETATION

- REVIEW OF GASPILS PERFORMANCE WITH CANMET/TC/TCP TO ESTABLISH OPERATIONAL CONFIGURATIONS AND USEAGE

- RECOMMENDED DETAILED OPERATIONAL SENSOR CONFIGURATION AND APPLICATIONS METHODOLOGY

PHASE IV - DEVELOP PRODUCTION UNIT

Financial Review

	Contract	Actual	Projected	Variance
Phase I	66,754	~71,000	~71,000	~4,500
Phase II	127,670	---	127,670	---
TOTAL	194,424	71,000	198,670	4,500

APPENDIX II

1. SOLAR EFFECT AT 7.8 μ

As shown in Figure 7, the solar radiation collected by the sensor consists of the direct reflected solar radiation, E_R, and the atmospheric scattering radiation, E_θ. For 5% reflectance we estimate $E_R = 6 \times 10^{-7}$w and $E_\theta = 1 \times 10^{-7}$w. The ground radiance, E_g, is estimated to be approximately 8×10^{-4}w. For this solar radiation power, the total atmospheric residual CH_4 gas gives a difference signal as small as 50 ppm.M methane leak gas signal which is the sensor detection limit.

This solar effect may fluctuate if the sky condition varies from place to place as the aircraft flies, due mainly to the prescence of the clouds. Extinction and scattering coefficients of three cloud classes are shown in the following figure. The data shows a very high extinction coefficient as well as a very high scattering coefficient at $\lambda = 7.8$ μ. For any clouds over 1 Km thick, the solar radiation at 7.8 μ will be completely blocked. This means that on a cloudy day there will be no solar effect. Also, if the sky condition is uniform the solar effect while not negligible will be constant in time.

When a cloud comes between the sensor and the sun, the sensor will see a false signal on the methane channel. This is shown above to be only 50 ppm.M and it is considered unnecessary to attempt to determine this false signal.

Since the reflected solar radiation power at 7.8 μ is so small it may be very difficult to incorporate any signal processing routine to discriminate the solar effect.

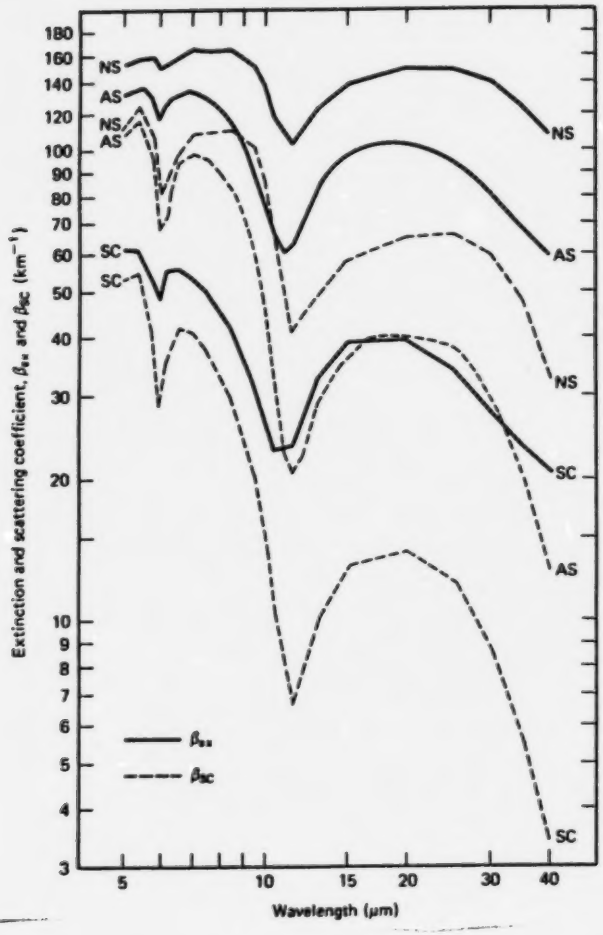

Extinction and scattering coefficients versus wavelength for three different cloud classes

2. ENVIRONMENTAL REQUIREMENTS

The sensor can be operated almost any time, except in the case of snow or rain. There is however a sensitivity which depends on environmental conditions.

Since the sensor signal depends on the ground thermal radiation it will even function during the night hours and any solar effect is absent in this case. The sensitivity of the sensor will vary during the day due to the change in the atmospheric temperature lapse rate (refer to the following figure) and atmospheric instability. The best time of operation during the day will be decided by the field trials. It is not straightforward to predict the best time of day because the sensitivity is determined by $(\varepsilon B_e - B_a)$ and it is necessarily best when $(B_e - B_a)$ is a maximum since the emissivity term cannot be neglected. Figure 3 in the report suggests that at an expected ε of 0.95, good sensitivity will occur in the ΔT range of say 0.5 to 3°K. According to the following figure this should be normally expected.

The wind speed is also an important factor in the field operation in terms of the dispersion of the leak gas. Low wind speed and low atmospheric instability is desirable.

The sensor sensitivity is directly related with the seasonal ground temperature. Therefore, the sensitivity of the sensor in wintertime will decrease to approximately 20% of the summertime value for the methane signal, and approximately 30% for the ratio signal.

The operating environment of the sensor will be isolated since the sensor head will be thermally insulated, and the chopper wheel will be temperature controlled to approximately 0.1 K. It may be necessary, in the research instrument, that the temperature be reset for different seasons of the year since it is expected that the thermal control will be based on heating only.

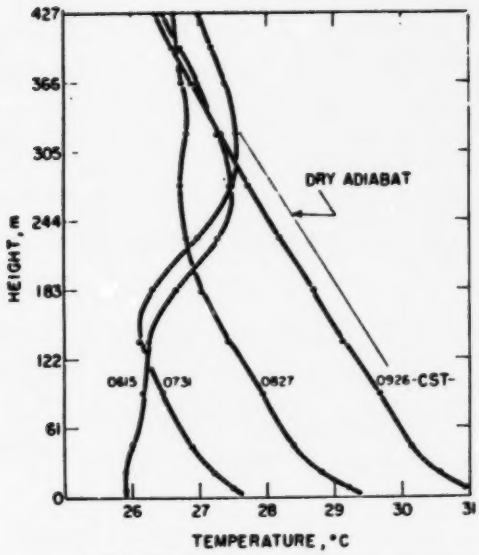

Temperature profiles for various times of the day

3. OUTPUT OF THE SENSOR

The gas signal output consists of two analog electronic signals corresponding to the methane signal, ethane signal and the ratio (ethane/methane) signal, respectively. An alarm will also be provided to indicate a gas leak. The threshold of the alarm will be decided based on the results of the field test. The prototype sensor will also be made to output the radiometric signal at each band.

The instrument sensitivity becomes zero when $(\varepsilon\bar{B}_e - \bar{B}_o)$ becomes zero. We have decided to monitor the instrument sensitivity and incorporate it as an extra output.

The non-zero methane signal for the residual CH_4 gas can be used to monitor the sensor sensitivity if we assume the residual gas signal is constant, since it is also governed by the same instrument sensitivity.

The absolute value of the methane signal will be monitored and a threshold will be set below which the instrument sensitivity is not reliable.

4. EFFECT OF THE TOTAL RESIDUAL GAS IN THE SKY

At 7.8 μ, the Planck function is very insensitive to temperature changes, thus $\bar{B}_e \simeq \bar{B}_a$ for $\Delta T = 1$ K in equation (1-14). Neglecting $B_s R$ one can approximate equation (1-14) as

$$\Delta S = A\Omega\eta_c\Delta\nu \quad (1 - \varepsilon)[(\overline{T_s T_a T_c} - \bar{T}_s \bar{T}_a \bar{T}_c)(\bar{N}_x - \bar{B}_s) - (\overline{T_a T_c} - \bar{T}_a \bar{T}_c)\, \bar{B}_a]$$

An estimation shows the first term in square parenthesis will have approximately the same magnitude as the second term. Therefore, as the ground emissivity varies the signal may fluctuate with an amplitude which is as large as that without the sky residual gas effect. However, twice the current signal processing concept is still valid, as the ratio signal effectively isolates the ground emissivity term.

In the worst case, if the ethane signal is too small to detect, one can use another atmospheric interferent gas such as N_2O, to replace the ethane. We will then rely on the ratio signal between methane and N_2O, to compensate for the varying emissivity term, i.e., the output will be the methane signal and methane signal/N_2O signal.